2011

Dynamic modeling, simulation and control design of a parafoil-payload system for ship launched aerial delivery system (SLADS)

Anand S. Puranik
Michigan Technological University

DYNAMIC MODELING, SIMULATION AND CONTROL DESIGN OF A PARAFOIL-PAYLOAD SYSTEM FOR SHIP LAUNCHED AERIAL DELIVERY SYSTEM (SLADS)

By

Anand S Puranik

A DISSERTATION

Submitted in partial fulfillment of the requirements for the degree of

DOCTOR OF PHILOSOPHY

(Mechanical Engineering – Engineering Mechanics)

MICHIGAN TECHNOLOGICAL UNIVERSITY

2011

This dissertation, "Dynamic Modeling, Simulation And Control Design Of A Parafoil-Payload System For Ship Launched Aerial Delivery System (SLADS)," is hereby approved in partial fulfillment for the requirements for the Degree of DOCTOR OF PHILOSOPHY IN Mechanical Engineering – Engineering Mechanics.

Department of Mechanical Engineering – Engineering Mechanics

Advisor: _____
Dr. Gordon Parker

Committee Member: _____
Dr. Chris Paserrello

Committee Member: _____
Dr. Jason Blough

Committee Member: _____
Dr. Allan Struthers

Department Chair: _____
Professor William W. Predebon

Date: _____

Contents

List of Figures

List of Tables

Acknowledgments

I take this opportunity to express my deepest regards to my advisor and mentor Dr. Gordon Parker, who has been a strong support for me during my graduate student life at Michigan Technological University. He not only provided opportunities to get exposed to myriad of research and teaching activities, but also subtly inculcated in me an habit of independent work ethic and attention to details. I would always be grateful to him for my qualitative professional development.

I also thank my project sponsors, Mr. Dexter Bird of Craft Engineering Associates and Mr. Frank Leban of Office of Naval Research. It was a wonderful experience working with you both on different aspects of this project and would like to maintain this professional relationship in future too.

I would like to appreciate my dissertation committee members Dr. Chris Paserrello, Dr. Jason Blough and Dr. Allan Struthers who gave their valuable time for critically analyzing my work and giving me timely feedback.

It was my parents' dream that their progenies be involved in excellent learning opportunities, both academically and qualitatively. They have strived all through their life to fulfill this dream. Today, while standing at the doors of, which can arguably be called as the epitome of academic success, I feel indebted to my parents for providing me best of the life so that I could reach this point. Thanks for being there with me always. My wife has been

a strong support since last two years in all the troughs and crests of daily life. It wouldn't have been possible without her love and patience.

My friends at Michigan Tech University were my family away from home. They always created a homely environment for a stable mind and focused study. I consider myself very lucky to have lived with exceptionally good housemates at 1913B, Woodmar Drive.

I would miss the fun times spent with my labmates, Maruthi Devarakonda, James Diaz, Jason Chea, Arunandan Sharma and Ed Trinklein in lab 306.

Finally, last but not the least, it is all possible because of some supreme intervention. Thank you God.

Nomenclature

α	Angle of attack
β	Side slip angle
Δ	Perturbation of a variable
δ_a	Asymmetric control input or brake deflection
δ_s	Symmetric control input or brake deflection
$\dot{L}$	Tow cable payout rate
η	Wind vector elevation angle
$\hat{I},\hat{J},\hat{K}$	Unit vectors along the axes of the inertial frame of reference
$\hat{i}_b,\hat{j}_b,\hat{k}_b$	Unit vectors along the axes of the reference frame attached to parafoil-payload system
$\hat{i}_T,\hat{j}_T,\hat{k}_T$	Unit vectors along the axes of the tow cable frame of reference
λ	Eigenvalues
$\mathcal{C}$	Controllability matrix

$\mathcal{O}$	Observability matrix
μ	Wind vector azimuth angle
ϕ_2	Roll angle of the parafoil-payload system
ψ_1	Off-plane tow angle of the tow cable in XY inertial frame
ψ_2	Yaw angle of the parafoil-payload system
ρ	Density of the air
θ_1	In-plane tow angle of the tow cable in XZ inertial frame
θ_2	Pitch angle of the parafoil-payload system
$\underline{u}$	Input vector
$\underline{u}_0$	Steady state input vector
$\underline{x}$	State vector
$\underline{x}_0$	Steady state vector
$\vec{r}_1$	The absolute position of the ship
$\vec{r}_2$	The absolute position of the CG of the parafoil-payload system
$\vec{r}_{3/1}$	The relative vector between the two ends of the tow cable
$\vec{r}_{3/2}$	The relative vector between the CG of the parafoil-payload system and the point of tow cable attachment
$\vec{r}_{4/2}$	The relative vector between the CG of the parafoil-payload system and the aerodynamic center

$\vec{v}_1$, v_s	The velocity of the ship
$\vec{v}_2$	The velocity of the CG of the parafoil-payload system
$\vec{v}_w$	Wind velocity vector
$\vec{v}_{4/w}$	The velocity of the aerodynamic center of the parafoil canopy with respect to wind
$\{B\}$	Reference frame attached to the parafoil-payload system
$\{I\}$	Inertial frame of reference
$\{T\}$	Tow cable frame of reference
$\{W\}$	Wind frame of reference
b	Span of the parafoil canopy
c	Chord of the parafoil canopy
C_D	Drag coefficient
C_L	Lift coefficient
C_l	Rolling moment coefficient
C_m	Pitching moment coefficient
C_n	Yawing moment coefficient
C_Y	Side force coefficient
F_D	Drag Force

F_L	Lift Force
F_Y	Side Force
I_{xx}	Total moment of inertia of the parafoil-payload system about body reference X axis
I_{yy}	Total moment of inertia of the parafoil-payload system about body reference Y axis
I_{zz}	Total moment of inertia of the parafoil-payload system about body reference Z axis
L	Tow cable length
m	Total mass of the parafoil-payload system
M_{4x}	Rolling moment
M_{4y}	Pitching moment
M_{4z}	Yawing moment
m_{air}	Mass of the air trapped in the inflated canopy
m_{app}	Apparent mass
m_{cpy}	Mass of the parafoil canopy
m_{pl}	Mass of the payload
p	Rotational velocity component of the CG of the parafoil-payload system in the body reference X axis

$p_{2/1,z}$	Relative altitude between the parafoil-payload system and the ship in $\{I\}$ frame
pl_x	Payload dimension in inertial X direction
pl_y	Payload dimension in inertial Y direction
pl_z	Payload dimension in inertial Z direction
q	Rotational velocity component of the CG of the parafoil-payload system in the body reference Y axis
r	Rotational velocity component of the CG of the parafoil-payload system in the body reference Z axis
S	Area of the parafoil canopy
T	Kinetic energy of the system
t	parafoil canopy thickness
u	Translational velocity component of the CG of the parafoil-payload system in the body reference X axis
V	Potential energy of the parafoil-payload system
v	Translational velocity component of the CG of the parafoil-payload system in the body reference Y axis
V_∞	Relative wind velocity
w	Translational velocity component of the CG of the parafoil-payload system in the body reference Z axis

$\mathbf{F}_4$	The aerodynamic forces acting at the aerodynamic center 4 of the parafoil canopy represented in $\{B\}$ frame
$\mathbf{I}$	Inertia Matrix of the parafoil-payload system
$\mathbf{M}_4$	The aerodynamic moments acting at the aerodynamic center 4 of the parafoil canopy represented in $\{B\}$ frame
${}^B\vec{\omega}_B$	Angular velocity of the parafoil-payload system represented in $\{B\}$ frame
${}^B_I\mathbf{R}$	Rotation matrix to transform vectors from $\{I\}$ frame to $\{B\}$ frame
${}^B_W\mathbf{R}$	Rotation matrix to transform vectors from $\{W\}$ frame to $\{B\}$ frame
${}^T\vec{\omega}_T$	Angular velocity of the tow cable represented in $\{T\}$ frame
${}^T_I\mathbf{R}$	Rotation matrix to transform vectors from $\{I\}$ frame to $\{T\}$ frame
JPADS	Joint Precision Airdrop System
MMIST	Mist Mobility Integrated Systems Technology Inc
PADS	Precision Airdrop System
PEGASYS	Precision Extended Glide Air Drop System
SLADS	Ship Launched Aerial Delivery System

Abstract

Dynamic Modeling, Simulation And Control Design Of A Parafoil-Payload System For Ship Launched Aerial Delivery System (SLADS)

Anand S Puranik

Michigan Technological University, 2011

Advisor: Dr. Gordon Parker

The objective of this research was to develop a high-fidelity dynamic model of a parafoil-payload system with respect to its application for the Ship Launched Aerial Delivery System (SLADS). SLADS is a concept in which cargo can be transfered from ship to shore using a parafoil-payload system. It is accomplished in two phases: An initial towing phase when the glider follows the towing vessel in a passive lift mode and an autonomous gliding phase when the system is guided to the desired point. While many previous researchers have analyzed the parafoil-payload system when it is released from another airborne vehicle, limited work has been done in the area of towing up the system from ground or sea. One of the main contributions of this research was the development of a nonlinear dynamic model of a towed parafoil-payload system. After performing an extensive literature review of the existing methods of modeling a parafoil-payload system, a five degree-of-freedom model was

developed. The inertial and geometric properties of the system were investigated to predict accurate results in the simulation environment. Since extensive research has been done in determining the aerodynamic characteristics of a paraglider, an existing aerodynamic model was chosen to incorporate the effects of air flow around the flexible paraglider wing. During the towing phase, it is essential that the parafoil-payload system follow the line of the towing vessel path to prevent an unstable flight condition called 'lockout'. A detailed study of the causes of lockout, its mathematical representation and the flight conditions and the parameters related to lockout, constitute another contribution of this work. A linearized model of the parafoil-payload system was developed and used to analyze the stability of the system about equilibrium conditions. The relationship between the control surface inputs and the stability was investigated. In addition to stability of flight, one more important objective of SLADS is to tow up the parafoil-payload system as fast as possible. The tension in the tow cable is directly proportional to the rate of ascent of the parafoil-payload system. Lockout instability is more favorable when tow tensions are large. Thus there is a trade-off between susceptibility to lockout and rapid deployment. Control strategies were also developed for optimal tow up and to maintain stability in the event of disturbances.

1. Introduction

A parachute has been an object of general interest as well as a topic of scientific research, ever since André Jacques Garnerin took a successful jump with a parachute from a balloon in 1797. During the 19th century the focus of the parachute development was to make it more compact and stable, until it was successfully used in military operations during World War I. It was in 1960 that Ms. Domina Jalbert improved the parachute design considerably and invented a new device called the ram air parachute or parafoil.

Parafoils are extensively used today by sport enthusiasts as well as military forces. Their light weight structure, high maneuverability and ability to travel large distances make them especially useful in supplying troops as well as providing urgent humanitarian supplies in areas of natural calamities. Typically, the 'payload' is attached to a parafoil and dropped from an airplane. The US Air Force's Precision Airdrop System (PADS) and US Army's Precision Extended Glide Air Drop System (PEGASYS), combined into a Joint Precision Airdrop System (JPADS) program. JPADS is the program which has promoted extensive research and development in deploying parafoil-payload systems from an airplane and autonomously guide it to the touchdown point with precision. Today, such systems are commercially available. For example, Mist Mobility Integrated Systems Technology Inc (MMIST) has developed the 'SnowGoose' Unmanned Aerial Vehicle and 'Sherpa' Precision Aerial Delivery System, capable of cargo delivery up to 10,000 lbs. Airborne Systems'

'FireFly', a Guided Precision Aerial Delivery System, is capable of dropping payloads from altitudes up to 7500 meters and precisely guiding to a point within 150 meters of the designated impact point. This work focuses on the analysis and control research that will facilitate similar operations using a towed deployment approach.

This chapter is organized as follows. Section 1.1 presents various projects and scientific missions which have been conducted in the past in the related field of aerodynamic decelerators. Section 1.3 describes the US Navy Ship Launched Cargo Delivery (SLADS) project. A summary of research contributions made during this doctoral work is outlined in Section 1.4, followed by an outline of this dissertation in Section 1.5.

1.1 Background

Parachutes and parafoils have been studied for their application of precision airdrop systems. Early research focused on understanding the aerodynamics and stability characteristics of this peculiar flexible wing, and soon parafoils were seen as a prime component of airdrop systems. The two main U.S. programs which promoted research on parafoils during last two decades were:

1. NASA X-38 crew return vehicle
2. The Joint Precision Airdrop System (JPADS) which was a joint program of US Army and US Air Force

NASA's crew return vehicle prototype consisted of a 18,000 lbs pallet, simulating the actual X-38, attached to a 7500 sq. ft parafoil, which was the largest parafoil parachute in history (8). It was tested at the US Army's Yuma Proving Grounds in Arizona. It was

dropped from a C-130 aircraft at an altitude of 21,500 feet. Starting with the descent speed of 60 miles an hour, it landed with a descent speed of less than 8 miles an hour. In the process of this successful testing, a variety of dynamic models of parafoil-payload systems were developed, many experimental tests conducted to understand the aerodynamics of the parafoils and tremendous resources were invested to formalize the research in the field of aerodynamic decelerators.

From the early 90's, the US Air Force has worked on the Precision Air Drop System (PADS) while the US Army developed the Precision Extended Glide Air Drop System (PEGASYS). A combined Army and Air Force initiative resulted in the Joint Precision Air Drop System (JPADS) Advanced Concept Technology Demonstration (ACTD) in August 2003. The purpose of this program was to develop a system capable of delivering payloads ranging from 200-10,000 lbs to a point within 300 feet of the ground target from altitudes of 25,000 feet.

Some of the other precision airdrop systems include Small Autonomous Parafoil Landing Experiment by Institute of Flight Mechanics of the German Aerospace Center (9), High Altitude Balloon Experiments in Technology HABET by Iowa State University (10), Advanced Precision Aerial Delivery System by FXC Corporation (11), the Precision Guided Parachute System by Atair Aerospace and others (12).

In all these applications the parafoil-payload system has been modeled and experimented for the 'airdrop' application. Interestingly, there hasn't been any significant published research in the area of towed parafoil payload system, which forms the main topic of this dissertation.

1.2 Aerodynamic Decelerators

Aerodynamic decelerator is a technical term used to describe an object made from textiles designed to produce drag. There are various existing devices which fall under the category of aerodynamic decelerators such as:

1. Parachute
2. Parasail
3. Paraglider or Ram-Air Parachute

1.2.1 Parachute

"A parachute is a device used to slow the motion of an object through an atmosphere by creating drag" (1). The word parachute comes form the French word *para* which means "to prepare for" or "to protect against", and *chute*, a French word for "fall", which means "that which protects against a fall". Parachutes are used extensively for a wide range of applications from recreational activities to military operations. The 'drouge chutes' used by aircrafts, racing cars or the ones used for tow cable retraction, fall into the category of parachutes. Figure 1.1 shows an American paratrooper using a MC1-1C series parachute (1).

1.2.2 Parasail

A parasail is a specially designed parachute used for towing behind a tow vehicle. The first parasail was developed by Pierre-Marcel Lemoigne in 1961 (13). Parasailing, which is also known as parascending, is a popular recreational activity as seen in Figure 1.2.

Figure 1.1. An American paratrooper using a MC1-1C series parachute (1). (See Appendix D for the documentation that this material is in public domain.)

Figure 1.2. Parasail is a towed parachute (2). (See Appendix D for the documentation that this material is in public domain.)

1.2.3 Paraglider

A paraglider or a ram-air parachute is a free flying or towed, foot launched aircraft. It has a rectangular planform with its front end open and the rear end closed, which keeps the canopy inflated, while it is moving through the air. The increased gliding capabilities along with its ability to be maneuvered easily, makes paragliding an enterprising activity for sport enthusiasts. Figure 1.3 shows a ram air parachute in free flight. The main parts of the paraglider are labeled and described below, as defined in Reference (14).

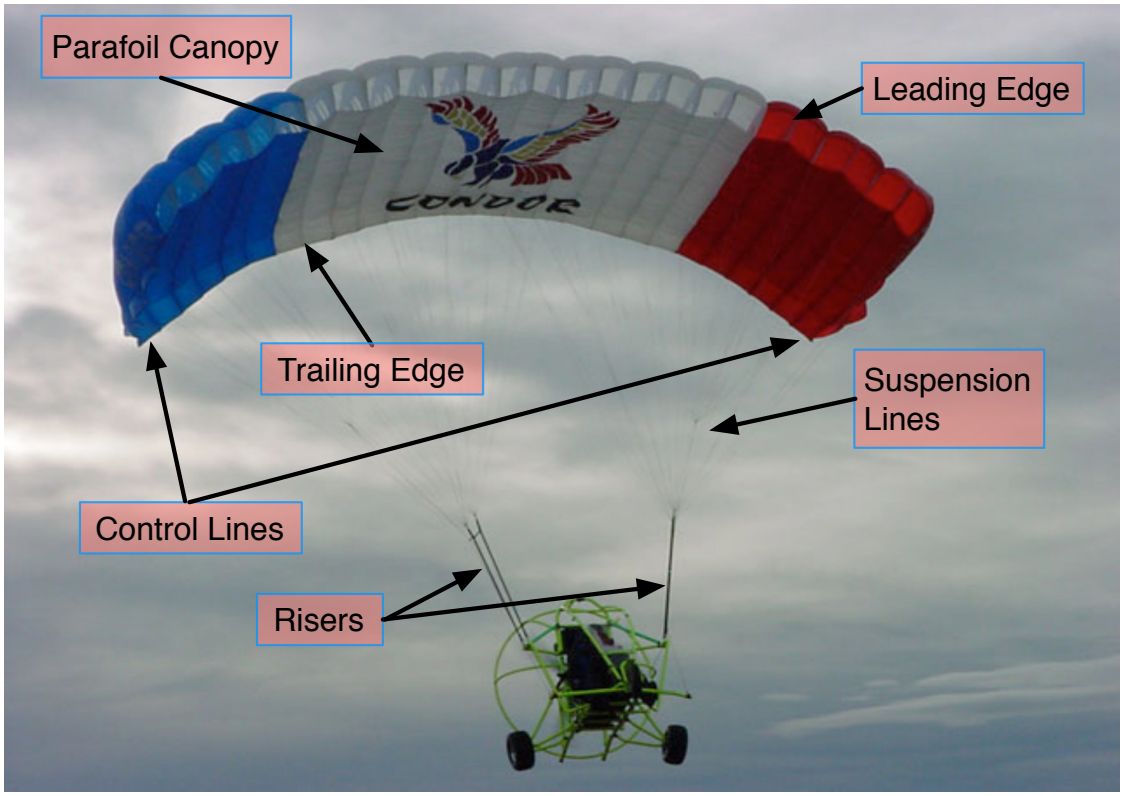

Figure 1.3. Significant parts of a paraglider or ram-air parachute (3). (See Appendix D for the documentation of the permission to republish this image).

1.2.3.1 Parafoil Canopy

When a ram-air parachute or paraglider is inflated it forms the shape of a low aspect ratio wing. The typical airfoil of a paraglider is called a parafoil or canopy. The terms parafoil and paraglider are many times used interchangeably. Typically when a ram air parachute is used for unmanned activities, the system is called a parafoil-payload system.

1.2.3.2 Leading Edge

The front end of the canopy is called the leading edge which has holes or cell openings to allow the air to flow inside.

1.2.3.3 Trailing Edge

The rear end of the canopy is called the trailing edge which is closed to keep the air inside and maintain the pressure for keeping it inflated.

1.2.3.4 Suspension Lines

The suspension lines are the main support chords which connect the canopy with the payload or the harness of the pilot.

1.2.3.5 Control Lines

The control lines are the lines connected to the trailing edge of the canopy on the both sides and are used by the pilot to steer the paraglider by deflecting its trailing edge.

1.2.3.6 Risers

The risers are the short straps or webbing used to connect the suspension lines to the harness or the payload in an organized way so that the pilot can selectively influence certain lines.

1.3 Ship Launched Aerial Delivery System (SLADS)

As discussed above, previously reported research on controlled paragliders focus on the parafoil released from a certain height and guided to a pre-defined target point on the Earth. During naval littoral operations, there is often a need to supply troops. It is required that the system be capable of delivering goods from a ship to unprepared spots on the shore. This is the main motivation behind developing a cargo delivery system which is launched from a ship.

The key mechanical component of a ship launched cargo delivery system is a suitable, light weight airfoil structure. With the space limitations on-board ships, a flexible airfoil structure that can be folded and stored in a small volume is desirable.

The SLADS is a four stage concept as shown in Figure 1.4. The parafoil-payload system is towed up to a desired altitude of about 2000 -2500 feet. Once it reaches this altitude, the tow cable will be detached from the parafoil-payload system and retrieved with the help of a small drag chute. The next stage is free flight wherein the parafoil-payload system will be autonomously guided towards the point on the shore where the cargo is to be delivered. In the third stage, the payload will be dropped along with a small parachute attached. Finally the powered glider will fly back to the tow vessel for retrieval.

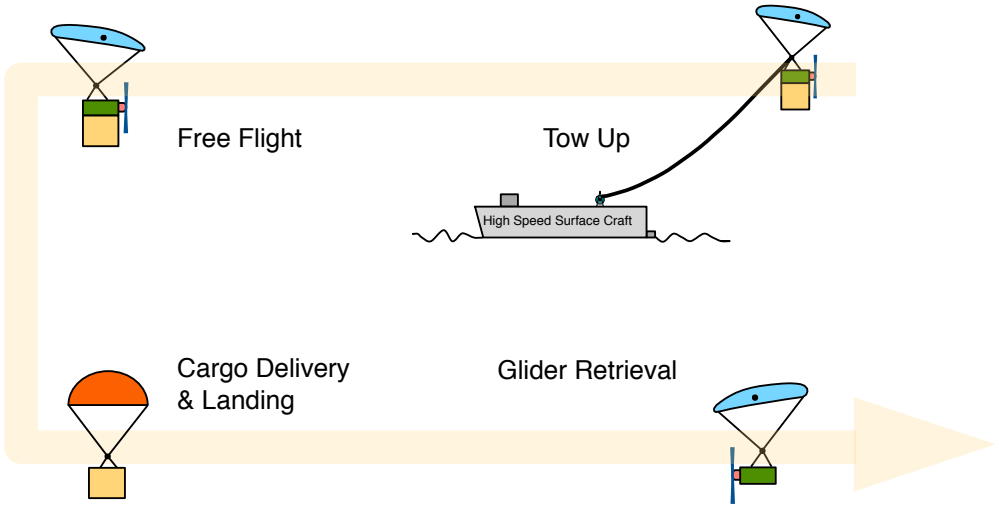

Figure 1.4. Stages of operation of SLADS.

1.4 Research Contributions

Though various models of parafoil-payload systems are available in the literature, they have been developed from the point of view of releasing the system from another airborne vehicle. This research is focused on modeling the parafoil-payload system in its towing phase, so as to successfully tow-up the system from a vessel at sea. The key attributes of the system are speed of deployment and stability. The towed system has been modeled to capture both longitudinal and lateral flight conditions. Model parameters are used in accordance with the testing facilities available at Craft Engineering Associates. The main problem while towing up a parafoil is that of lockout, which will be explained in detail in Chapter 4. Another contribution is the mathematical development and analysis of lockout. After validating the model, control strategy development, which maintains stability while minimizing tow-up time, is developed.

1.5 Dissertation Outline

This document is organized as follows. Chapter 2 presents a comprehensive literature review on various aspects of modeling parafoil-payload systems. A detailed mathematical model of a towed parafoil-payload system is presented in Chapter 3. Chapter 4 elaborates on the main instability problem during the tow-up, which is called 'lockout'. A detailed stability analysis follows, which describes the conditions and causes of lockout. Chapter 5 is dedicated to control system development for optimal towing performance, while maintaining system stability. Chapter 6 concludes with presenting conclusions out of this study and describing the opportunities for further research.

2. Literature Review

This chapter is organized as follows. Section 2.1 briefly reviews the history of flexible kites, hang gliders and paragliders. Section 2.3 describes briefly the research done in the field of dynamic model development of parafoil-payload systems. A detailed discussion of longitudinal and lateral stability analysis follows in Section 2.5. Section 2.6 reviews the methods of modeling the parafoil brakes, followed by Section 2.7 which describes the significance of modeling apparent mass in the aerodynamics of parafoils.

2.1 Parafoil Evolution

The breakthrough in the field of aerodynamic decelerators came with Francis and Gertrude Rogallo's invention of a 'Flexible Kite', US Patent # 2,546,078 issued March 20, 1951 (15). In particular, their invention related to 'kites with completely flexible surfaces'. The invention evolved in two directions. One development was the parawing, a completely flexible parachute-like structure that could be guided and controlled and was investigated for potential use as a recovery mechanism for space craft during re-entry. The other development was the sport hang glider as shown in Figure 2.1. In the mid 1960's, water skiers found that, by adding a weight shift bar, they could release from the towline and glide effortlessly to shore. The tubular frame, flexible kite became known as the Rogallo wing and launched

the popular sport of hang gliding.

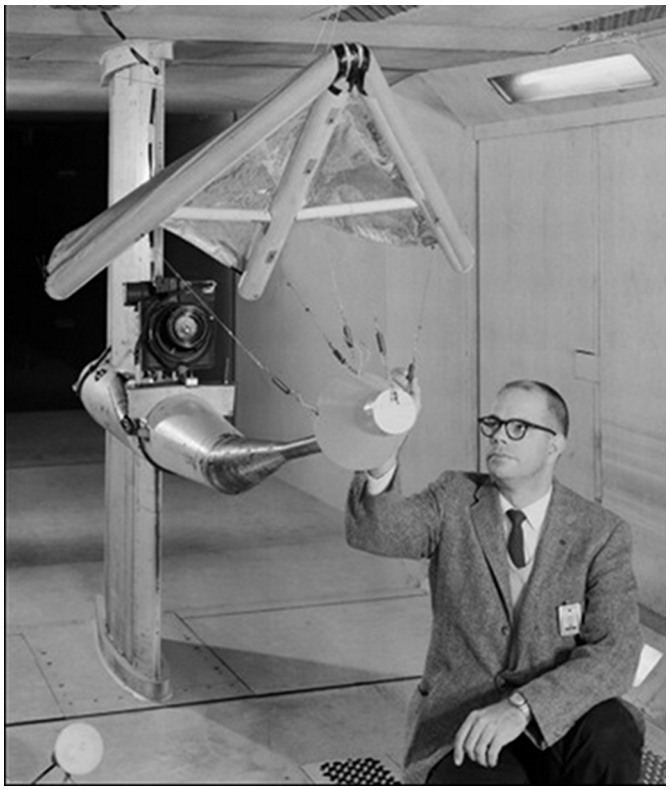

Figure 2.1. Francis Rogallo with his parawing in the wind tunnel. (Photo credit: NASA/courtesy of nasaimages.org. See Appendix D for the documentation that this image is in the public domain.)

The next major breakthrough in lightweight airfoil structures came with Domina Jalbert's invention of a 'Multi-Cell Wing Type Aerial Device', US Patent # 3,285,546, issued November 15, 1966 (16). The invention was a "wing of rectangular or other shape having a canopy or top skin and a lower spaced apart bottom skin and with the skins being disposed in equidistantly spaced relation to each other by ribs of a flexible nature that are fixed to the top and bottom skins and so shaped as to constitute an air foil and with the ribs constituting air channels having a relatively large opening upon the leading edge of the wing." The device is most commonly referred to as a ram-air parachute or a parafoil.

2.2 Hang gliders and Paragliders

Hang gliders and paragliders are both highly maneuverable devices. The main difference lies in the rigidity of the devices. A paraglider can be easily packed like a parachute due to its flexible light weight structure. The rigid tubular structures of the hang glider make it more stable in case of wind turbulence. The hang gliders are faster than paragliders in free flight and can cover larger distances due to their high glide ratios. Table 2.1 shows a comparison of glide ratios of some gliding devices. The turning radius of the paraglider is much lesser than the hang glider, and hence a paraglider can land in much smaller space. Considering all these factors, a paraglider was found to be more suitable for the ship launched cargo delivery application.

Table 2.1.
Maximum Glide Ratios Obtained with Various Gliding Devices. (7)

Gliding Device	Glide Ratio (Lift/Drag)
Powered Parachute	5.6
Paraglider	11
Hang glider	15
Sail plane	70

2.3 Dynamic Models

Parafoil-payload systems in free flight have been modeled in variety of ways to suit the specific applications. One of the first publications on modeling the motion of parafoil-payload systems was made by Lingard *et. al.* (17), (12). He derived equations of motion of a three degrees of freedom (DOF) model by resolving the forces in the horizontal and vertical directions. The velocities calculated from this model were used to generate 2-dimensional

flight trajectories. This model incorporated the effect of wind on the range covered by the system. It also predicted the effects of varying canopy size, line length, rigging method etc. He claimed that the performance of the system could be improved by bifurcating and minimizing the diameter of suspension lines. Significant gains could also be obtained by closing the leading edge of the parachute, which in turn forms its swept wing shape to remain inflated. Glide ratio predicted by these improvement was 6:1, doubling the existing glide ratios of the day.

Yakimenko *et al.* developed a controlled model of a six DOF circular parachute (18). A detailed description of mathematical development along with equations of motion is presented. The final form of the equations are similar to the standard aircraft equations, except the difference of apparent mass terms in the inertial quantities. Equations 2.1 and 2.2 summarize the six DOF model of the circular parachute. The nomenclature used to described these equations is described below:

m = Total mass of the system

I_{xx}, I_{yy}, I_{zz} = Total moment of inertia about three body reference axes

α_{ij} = Terms from apparent mass tensor (6×6)

u, v, w = Translational velocity components of the CG of the system in body reference frame

p, q, r = Rotational velocity components of the system in body reference frame

K = Total mass moment of the system

$\mathbf{F}$ = Sum of all aerodynamic and gravity forces acting on the system

$\mathbf{M}$ = Sum of all aerodynamic moments and the moments caused

by aerodynamic forces about the CG of the system

$$\mathbf{F} = \begin{bmatrix} (m+\alpha_{11})(\dot{u}-vr)+(m+\alpha_{33})wq+(K+\alpha_{15})(\dot{q}+rp) \\ (m+\alpha_{11})(\dot{v}+ur)-(m+\alpha_{33})wp-(K+\alpha_{15})(\dot{p}-qr) \\ (m+\alpha_{33})\dot{w}-(m+\alpha_{11})(uq-vp)-(K+\alpha_{15})\left(p^2+q^2\right) \end{bmatrix} \tag{2.1}$$

$$\mathbf{M} = \begin{bmatrix} (I_{xx}+\alpha_{44})\dot{p}-(K+\alpha_{15})(\dot{v}-wp+ur)-(I_{yy}+\alpha_{44}-I_{zz}-\alpha_{66})qr+(\alpha_{33}-\alpha_{11})vw \\ (I_{yy}+\alpha_{44})\dot{q}-(K+\alpha_{15})(\dot{u}+wq-vr)+(I_{yy}+\alpha_{44}-I_{zz}-\alpha_{66})pr-(\alpha_{33}-\alpha_{11})uw \\ (I_{zz}+\alpha_{66})\dot{r}+(I_{yy}-I_{xx})pq \end{bmatrix} \tag{2.2}$$

Along with the mathematical model, the significant contribution of this work was the geometric description of the system consisting of a G-12 parachute and an A-22 container. Due to the large distance between the canopy and the payload, it was essential to know the mass and inertia properties accurately. A nonlinear system identification algorithm was applied to refine the aerodynamic coefficients. A comprehensive discussion on the mass properties, apparent mass effects, computation of the moments of inertia, computation of forces and moments proved to be an illustrative example for developing a detailed model for towed parafoil-payload system.

Müller *et. al.* developed a high fidelity nonlinear eight DOF model for its application as a NASA X-38 re-entry vehicle shown in Figure 2.2 (19). . In this model it was assumed that the parafoil exhibited six degrees of freedom and the payload had relative motion with an additional two DoF. This assumption is valid for the peculiar system of straps, wherein the payload had significant rotary motion around a pitch axis and a vertical axis only. A detailed mathematical modeling of the forces, moments, reactions at the joints and kinematic

constraints were explained, which provided a deeper insight on how the systems with relative motions are modeled. System response to symmetric brake inputs, lateral wind gusts and relative yaw motion of the payload were also analyzed.

Figure 2.2. NASA X-38 re-entry vehicle (4). Photo credit: NASA/courtesy of nasaimages.org. (See Appendix D for the documentation that this image is in the public domain.)

Thomas Jann at the Institute of Flight Research of the German Aerospace Center (DLR) developed two instrumented test vehicles ALEX I and II (Small Autonomous Parafoil Landing Experiment) (9). With the purpose of system identification and parameter estimation for Guidance Navigation and Control (GNC) design, the paper elaborates on development of both three DOF and four DOF models. Both these models were based on the rigid body assumptions and do not account for the relative motion between the canopy and the payload. In the three DOF model, only the motion of the center of the mass is considered and yaw rate changes due to asymmetric edge deflection were modeled with a first order delay. In the four DOF model, even the roll rate changes due to asymmetric edge deflections were modeled in the actuator dynamics. Parameters related to actuator dynamics and the

aerodynamic coefficients were estimated using the model and the experimentally measured data.

Slegers and Costello (5) developed a nine DOF model of a parafoil payload system to investigate the finer aspects of control using the parafoil brakes. Figure 2.3 shows the schematic of the nine DOF dynamic model [*]. The combined system of parafoil and the payload is assumed to be connected by the labeled joint C. The nine degrees of freedom include three inertial components of joint C along with three Euler orientation angles of parafoil and payload each. They developed this model using the prediction made by Doherr and Schilling (20), that a nine DOF model improves stability predictions as compared to a six DOF model.

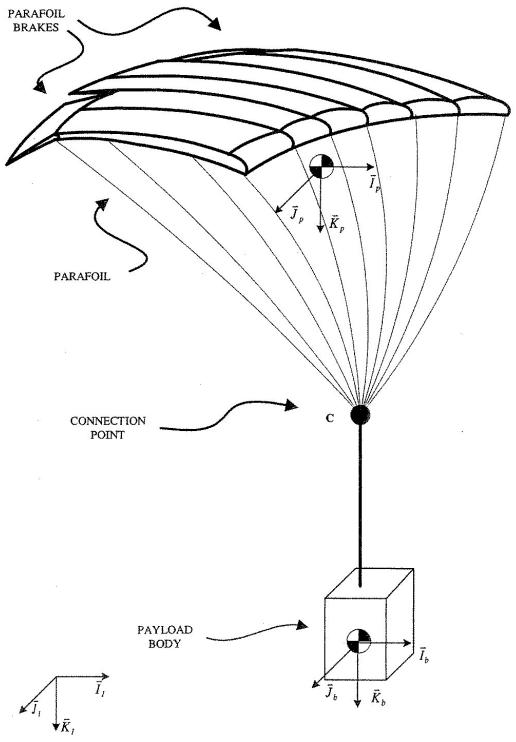

Figure 2.3. Nine DOF dynamic model of parafoil-payload system used by Slegers and Costello (5). (See Appendix D for the documentation of permssion to republish this figure from (5).)

[*] Reprinted with permission of the American Institute of Aeronautics and Astronautics

The interesting findings of this work have provided a deeper insight into the control mechanisms of parafoil-payload system. They claimed that such systems exhibit two modes of operation: roll steering and skid steering. For example, the roll steering mode would turn the system left when right brake is activated, while in skid steering it turns right with the same control input. They used the model to predict the effect of the orientation of the parafoil canopy with respect to the payload, defined by the angle called 'incidence angle' and magnitude of brake deflection on the modes of steering. Also, by modeling the canopy as shown in Figure 2.4, they proved that increasing the canopy curvature can affect the mode of steering [†].

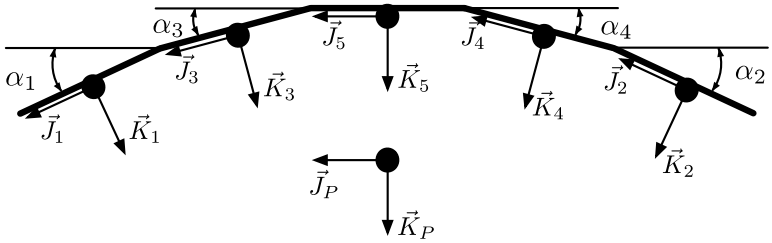

Figure 2.4. Panel discretization used by Slegers and Costello (5). (See Appendix D for the documentation of permssion to republish this figure from (5).)

All these dynamic models were studied in detail to understand the modeling procedures used to suit the specific purpose or application. A thorough understanding of the towed deployment requirements accompanied with the review of these models, prompted the use of a five DOF model of the parafoil-payload system for SLADS.

[†] Reprinted with permission of the American Institute of Aeronautics and Astronautics

2.4 Aerodynamic Theory

This section focuses on review of some basic concepts and terminologies related to aerodynamics, which will be used as standard terms in this dissertation. An object moving through air, is acted upon by the forces and moments created to due to the relative motion between the object and the air. These forces and moments are described mathematically to model their effect in the simulation environment. Following are few terms described which form the part of any standard aerodynamic analysis.

2.4.1 Angle Of Attack (α)

Angle of attack is the angle made by the reference line or the chord line of the airfoil with the vector representing the relative velocity between the object and the fluid through which it is moving. Figure 2.5 shows the angle of attack of a parafoil moving through air, where the relative velocity vector is represented by $\vec{V}_\infty$. Due to the flexible nature of the wing span, the angle of attack of a parafoil, though standard term in theory, is very difficult to measure on the towed system.

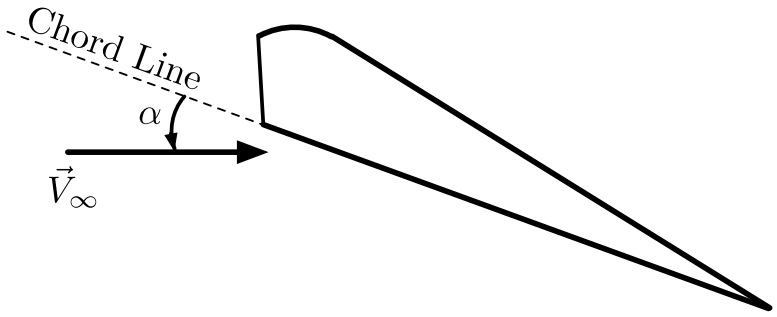

Figure 2.5. Angle of attack α

2.4.2 Side Slip Angle (β)

Side slip angle is the angle made by the aircraft centerline with the direction of the relative velocity vector. Figure 2.6 shows a positive side slip angle of an aircraft. The same definition applies to a paraglider wing in top view.

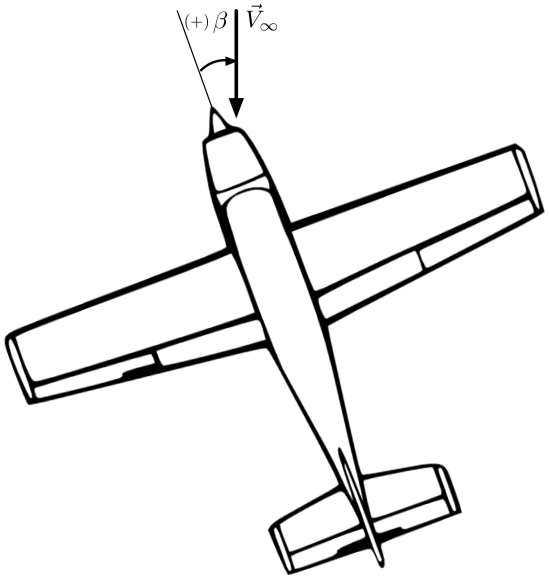

Figure 2.6. Side slip angle β

2.4.3 Aerodynamic Forces

2.4.3.1 Drag

The force of resistance to the motion of an object in a fluid is called drag D. The drag is a function of the magnitude of the relative velocity of the object V_∞, the density of the fluid ρ,the reference area of the object S and drag coefficient C_D. C_D depends on angle of attack α and in case of paragliders, the control input δ_s. This will be discussed in more

detail in Chapter 3.

$$D = f_1\left(V_\infty, \rho, S, C_D\left(\alpha, \delta_s\right)\right) \tag{2.3}$$

2.4.3.2 Lift

An object of an airfoil shape while moving through a fluid is acted upon by a lifting force due to the pressure difference between the top and the bottom surfaces, and is called lift L. The lift force, similar to drag, depends on the magnitude of relative velocity, the density of the fluid, the reference area and the lift coefficient C_L. For small values of angle of attack, the lift coefficient is linearly proportional to the angle of attack.

$$L = f_2\left(V_\infty, \rho, S, C_L\left(\alpha, \delta_s\right)\right) \tag{2.4}$$

2.4.3.3 Side Force

In the case of turns or crosswinds, an aircraft is acted upon by the side force Y, which is mainly the function of side slip angle β and in the case of paragliders, the asymmetric control input δ_a, in addition to the relative velocity, the density of the fluid and the reference area.

$$Y = f_3\left(V_\infty, \rho, S, C_Y\left(\beta, \delta_a\right)\right) \tag{2.5}$$

2.4.4 Aerodynamic Moments

2.4.4.1 Pitching Moment

Pitching moment is a moment imposed on the airfoil by the aerodynamic forces. If the forces are assumed to be acting on the aerodynamic center of the airfoil, it is called the pitching moment, denoted by m, and is in the body reference Y direction. The magnitude of the pitching moment depends on the length of the chord of the airfoil c.

$$m = f_4((V_\infty, \rho, S, c, C_m) \tag{2.6}$$

Here, the pitching moment coefficient C_m is a function of angle of attack α, the pitching angular velocity of the body q, and in the case of paragliders, the symmetric control input δ_s.

$$C_m = C_m(\alpha, q, \delta_s) \tag{2.7}$$

2.4.4.2 Rolling Moment

The moment acting on the aerodynamic center of the wing about the body reference X axis is called as rolling moment, denoted by l. The rolling moment depends on the span of the wing b, and

$$l = f_5((V_\infty, \rho, S, b, C_l) \tag{2.8}$$

The rolling moment coefficient C_l is the function of side slip angle β, asymmetric control input δ_a in case of paragliders, the roll angular velocity of the body p and the yaw angular velocity r.

$$C_l = C_l(\beta, \delta_a, p, r) \tag{2.9}$$

2.4.4.3 Yawing Moment

The moment acting on the aerodynamic center of the wing about the body reference Z axis is called as yawing moment, denoted by n. The yawing moment also depends on the span of the wing b.

$$n = f_6((V_\infty, \rho, S, b, C_n) \tag{2.10}$$

The yawing moment coefficient C_n is the function of side slip angle β, asymmetric control input δ_a in case of paragliders, the roll angular velocity of the body p and the yaw angular velocity r.

$$C_n = C_n(\beta, \delta_a, p, r) \tag{2.11}$$

2.5 Stability Analysis

The study of stability of a parachute-payload system is assumed to have commenced with the Ph.D. work of Wolf (21). Using a ten DOF model he proved that stability was reduced as riser length was increased or parachute weight was increased (5). Thomas Goodrick presented an analysis on static and dynamic longitudinal stability of high performace gliding airdrop systems in 1975 (6). The static analysis illustrated the relationship between the control inputs and glide performance. The dynamic analysis showed the re-

sponse to wind disturbance and control inputs. The static analysis equations described in his paper were elaborated in detail. The pitching moment coefficient obtained from this analysis was used in modeling the longitudinal aerodynamics of the towed parafoil payload system in Chapter 3.

Figure 2.7 shows a parafoil-payload system in longitudinal flight [‡]. Point **C** represents the canopy mass center, which is also the aerodynamic center of the canopy. Point **P** represents the mass center of the payload. The center of mass of the canopy and payload system, point **O** is located as,

$$r_1 + r_2 = d \tag{2.12}$$

where, r_1 is the distance between center of mass of the system **O** and mass center of the payload **P** Similarly, r_2 is the distance between point **O** and mass center of the canopy **C**.

For static analysis it is assumed that the pitching rate is zero i.e. $\dot{\theta} = 0$. Also, the drag acting on the payload is assumed to be negligible.

Assuming that m_1 is the mass of the payload and m_2 represents the total mass of the canopy and the air trapped in it,

$$m_1 r_1 = m_2 r_2 \tag{2.13}$$

Thus,

$$\frac{r_1}{d} = \frac{m_2}{m_1 + m_2} \tag{2.14}$$

$$\frac{r_2}{d} = \frac{m_1}{m_1 + m_2} \tag{2.15}$$

[‡] Reprinted with permission of the American Institute of Aeronautics and Astronautics

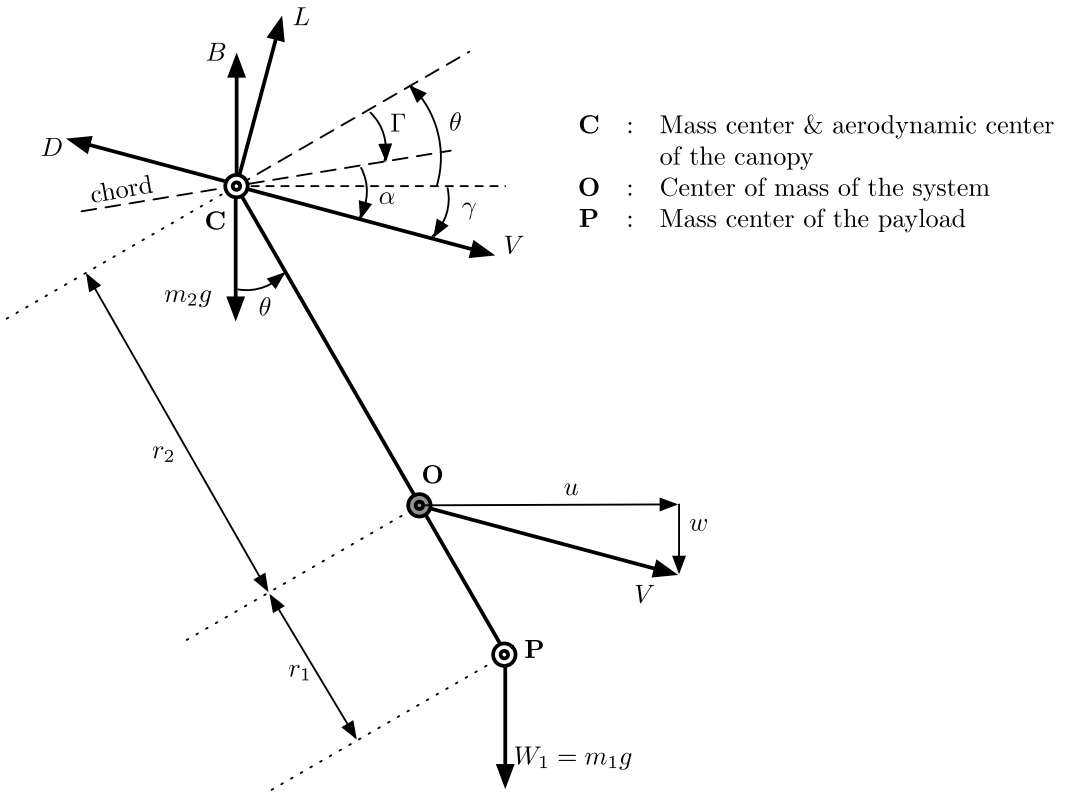

Figure 2.7. Longitudinal static analysis (6). (See Appendix D for the documentation of permssion to reprint this figure from (6).)

The net aerodynamic force acting at the aerodynamic center of the canopy is shown in terms of lift L and the drag force D. Also, the net weight of the canopy is the gravitational force W_2 minus the buoyancy force B caused by the included air mass. Thus,

$$W_2 = m_2 g - B \tag{2.16}$$

The system is assumed to glide steadily with velocity V with an angle of attack α and flight path angle γ. The incidence angle Γ is defined as the angle which the mean chord of the airfoil makes with an imaginary line perpendicular to the line OC. θ represents the pitch angle of the system. The total moment about the center of mass of the system can be written as,

$$\sum M = M_0 + r_2 \{D \cos(\alpha + \Gamma) - L \sin(\alpha + \Gamma) + W_2 \sin\theta\} - W_1 \sin\theta \tag{2.17}$$

Dividing Equation 2.17 by $1/2\rho V^2 Sc$, it can be expressed in dimensionless form.

$$C_m = C_{m_0} + \frac{r_2}{c} \{C_D \cos(\alpha + \Gamma) - C_L \sin(\alpha + \Gamma)\} + \frac{(W_2 r_2 - W_1 r_1)}{1/2\rho V^2 Sc} \sin\theta \tag{2.18}$$

If canopy volume is denoted as Q, then,

$$B = \rho Q g \tag{2.19}$$

The buoyancy constant is usually defined as,

$$C_{B_0} = \frac{2Qg}{Sc} \tag{2.20}$$

where, S is the canopy area and c is the length of the mean chord.

The last term in Equation 2.18 can be re-written using equation 2.16, 2.19 and equation 2.20 as,

$$\begin{aligned}\frac{(W_2 r_2 - W_1 r_1)}{1/2\rho V^2 Sc}\sin\theta &= \frac{[(m_2 g - B)r_2 - m_1 g r_1)}{1/2\rho V^2 Sc}\sin\theta \\ &= \frac{-r_2 \rho Q g}{1/2\rho V^2 Sc} \\ &= -\frac{C_{B_0}}{V^2}\frac{dm_1}{m_1 + m_2} \end{aligned} \tag{2.21}$$

Using the relation $\alpha + \Gamma = \theta + \gamma$ from Figure 2.7, θ can be eliminated from equation 2.18 as shown in Equation 2.22.

$$C_m = C_{m_0} + \frac{dm_1}{m_1 + m_2}\left[\left(\frac{C_D}{c} + \frac{C_{B_0}}{V^2}\sin\gamma\right)\cos(\alpha+\Gamma) - \left(\frac{C_L}{c} + \frac{C_{B_0}}{V^2}\sin\gamma\right)\sin(\alpha+\Gamma)\right] \tag{2.22}$$

Finally, using the steady state glide relations $L = W\cos\gamma$ and $D = W\sin\gamma$ equation 2.22 can be made independent of V and γ. The final form of the equation is given in Equation 2.23.

$$C_m = C_{m_0} + \left(\frac{dm_1}{m_1 + m_2}\right)\left(\frac{1}{c} + \frac{\rho}{2}\frac{C_{B_0}}{W/S}\right)[C_D\cos(\alpha+\Gamma) - C_L\sin(\alpha+\Gamma)] \tag{2.23}$$

Equation 2.23 is used in our analysis of towed parafoil-payload system to model the pitching aerodynamic moment.

Just as Goodrick analyzed the stability of the parafoil-payload system in longitudinal

flight conditions, Crimi studied the lateral flight to determine the relationship of various flight parameters and aerodynamic coefficients on the lateral stability (22). He illustrated typical aerodynamic loading in a parafoil-payload system including side force, rolling moment and yawing moment as a function of side-slip angle, roll rate and yaw rate as shown in Equations 2.24 to 2.26. The system was considered without any parafoil brake inputs.

$$C_Y = f_1(\beta, p, r) \tag{2.24}$$

$$C_l = f_2(\beta, p, r) \tag{2.25}$$

$$C_n = f_3(\beta, p, r) \tag{2.26}$$

The lateral linearized equations of motion are derived in a simplified form as shown in equation 2.27.

$$\dot{\mathbf{x}} = \mathbf{A}^{-1}\mathbf{B}\mathbf{x} \tag{2.27}$$

Here the state vector **x** is defined as,

$$\mathbf{x} = \begin{Bmatrix} \beta \\ \phi \\ \psi \\ \dot{\phi} \\ \dot{\psi} \end{Bmatrix} \tag{2.28}$$

The **A** matrix is defined as,

$$\mathbf{A} = \begin{bmatrix} -2 & 0 & 0 & 0 & 0 \\ 0 & 1 & 0 & 0 & 0 \\ 0 & 0 & 1 & 0 & 0 \\ 0 & 0 & 0 & -h_{xx} & -h_{xz} \\ 0 & 0 & 0 & -h_{xz} & -h_{zz} \end{bmatrix} \tag{2.29}$$

and **B** matrix is defined as,

$$\mathbf{B} = \begin{bmatrix} -C_{Y\beta} & -C_L & -C_L \tan\gamma & y_s & y_\delta \\ 0 & 0 & 0 & 1 & 0 \\ 0 & 0 & 0 & 0 & 1 \\ -2\mu l_\beta & 0 & 0 & -l_p & -l_r \\ -2\mu n_\beta & 0 & 0 & -n_p & -n_r \end{bmatrix} \tag{2.30}$$

The characteristic equation of the matrix $\mathbf{A}^{-1}\mathbf{B}$ yields a 4th order polynomial, the roots of which were used to analyze the lateral stability of the parafoil-payload system.

$$A\lambda^4 + B\lambda^3 + C\lambda^2 + D\lambda + E = 0 \tag{2.31}$$

It was observed that this characteristic equation yielded two real and one complex pair of roots. A stability boundary was plotted with respect to yaw aerodynamic coefficient C_{n_β} and various other parameters. The effect of suspension line lengths, glide slope and dihedral angle were studied. It was concluded that there were two modes of instabilities observed; spiral divergence and oscillatory instability. This methodology is used for the

stability analysis of the towed parafoil-payload system in Chapter 4.

2.6 Control Input

Though it was evident that the primary source of controlling the maneuverable parafoil-payload system is the symmetric and asymmetric control brake inputs, the analytical study of modeling control inputs commenced with the work of Glen J. Brown (23). He determined the relationship of control inputs to the roll and yaw angles of the system in steady turn flight condition. He modeled the control input as the ratio of the trailing edge of the parafoil deflected to the aerodynamic chord of the airfoil. Using the equation obtained from lateral and longitudinal equilibrium, he developed the control input relations analogous to the standard aircraft equations. He proved that the scale of the parafoil-payload system plays an important role in the response to the control inputs. Small parafoils with larger payloads are more sensitive to the control inputs. This causes the system to exhibit, what is called, roll steering. As the scale of the parafoil-payload system increases, the response shifts from roll steering to 'skid' steering. In skid steering, the parafoil takes a turn in the direction of the side, where the brake is applied. In skid steering the yaw moment predominates as compared to rolling moment. Also, the apparent mass effects produce a significant change in the the method of turning of a parafoil-payload system. Due to incrase in apparent mass, the distance between the aerodynamic center and CG of the system changes, causing the anti-roll moment which in turn contributes for skid turn as against the normal turn response. This work gave a significant insight into how the control input affects the lateral response of the system.

2.7 Apparent Mass Effects

For lightly loaded flight vehicles such as parafoils, the apparent mass of the air has a strong effect on the flight dynamics (24). Apparent mass is defined as "the quantity having the dimensions of the mass that is added to the mass of a body moving non-uniformly in a fluid medium in order to take into account the action of the medium on the body" (25). For standard air vehicles such as aircraft, the ratio of the mass of the vehicle to the mass of the air volume displaced is very high, and in turn the significance of apparent mass effects is very low. One more differentiating parameter between standard aircrafts and the paraglider is the 'wing loading', which is the ratio of the weight of the aircraft or the flying object to the area of the wing. For lightly loaded vehicles, such as parafoils, the wing loading is less than $5kg/m^2$. In such cases, the apparent mass terms can be very significant. For a parafoil-payload system, the large distance between the aerodynamic center and the CG of the overall system causes the apparent mass effect to be more pronounced, due to the significantly large amount of moments of inertia created by the apparent mass. For a typical geometry and wing loading, assuming a canopy mass of 10 percent of the payload, the apparent moment of inertia in roll about the apparent principal axis is about five times that of the parafoil-payload mass system itself (24). Therefore it is absolutely essential to take into account the effect of apparent mass and moments of inertia, especially while modeling a parafoil-payload system. Lissaman and Brown (24) have calculated the values of these apparent masses and inertia for a parafoil with respect to its geometric parameters, which have become a standard convention to include in analyzing the motion of parafoil-payload system.

3. Modeling Of Towed Parafoil-Payload System

This chapter is organized as follows. Section 3.1 describes the dynamic model of a towed parafoil-payload system in detail along with all modeling assumptions. Section 3.2 elaborates on the derivation of generalized equations of motion of the dynamic model using Lagrange's equations. The aerodynamics of the parafoil canopy is illustrated in Section 3.3. All the geometric and mass properties of the system are detailed in Section 3.4. Section 3.5 analyzes the longitudinal flight of the system and presents some typical simulation results. Section 3.6 presents the operator-in-the-loop capability to simulate the flight conditions real-time.

3.1 Model Description And Modeling Assumptions

A schematic model of a parafoil-payload system being towed behind a ship is shown in Figure 3.1. The significant points of the model along with the inertial frame of reference are shown. Point 1 represents the point of attachment of the cable at the ship end. Point 2 is the combined center of gravity (CG) of the parafoil payload system. Point 3 is the tow cable attachment point on the parafoil-payload system. Point 4 represents the aerodynamic center of the parafoil canopy, where all the aerodynamic forces and moments are assumed to act. The tow cable length is a variable and is one of the control inputs for optimal tow-up.

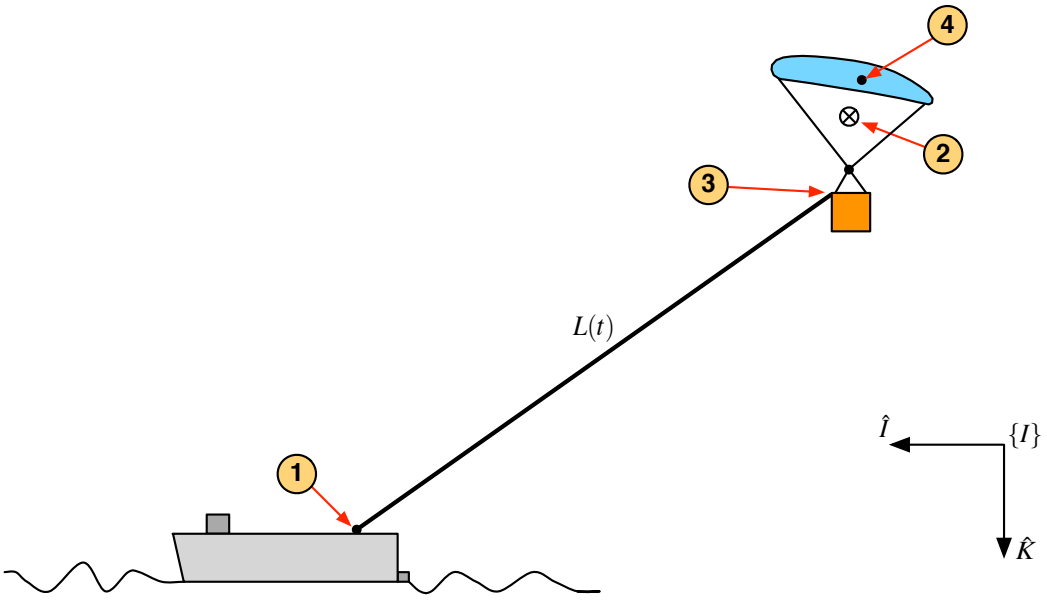

Figure 3.1. Significant points of the model.

Following are some assumptions made in the process of developing a model of practical relevance to its application in Ship Launched Aerial Delivery System (SLADS):

1. The parafoil and the payload are assumed to be rigidly connected by the suspension lines, i.e. No relative motion between the parafoil and payload.

2. The tow cable is assumed to be straight and imposes a kinematic constraint on the otherwise six DOF rigid body. The tow cables are usually made up of high strength para-aramid synthetic fiber called Kevlar. Kevlar has a Young's modulus, in the range of 85-186 GPa (26). The natural frequency of vibration of a Kevlar tow cable was evaluated for the cable length of 100 meters and cross-sectional diameter of 0.022m. It was found that this natural frequency is very high ($\approx$ 120Hz) as compared to the natural frequency of the parafoil-payload system ($\approx$ 1 Hz). Hence it will be assumed that there is no longitudinal vibration of the tow cable..

3. The tow cable is released at a constant rate without any accelerations or jerks.

4. Wind gusts are incorporated so as to affect the aerodynamics of the parafoil only.

5. Payload drag is assumed to be negligible as compared to the drag of parafoil.

3.2 Equations Of Motion

The set of generalized co-ordinates suitable to describe the motion of the system are shown in Equation 3.1, where

1. θ_1 represents the in-plane angle of the tow cable i.e. in XZ inertial frame.

2. ψ_1 represents the off-plane angle of the tow cable i.e. in XY inertial frame.

3. ϕ_2, θ_2 and ψ_2 represent the Euler angles of the parafoil-payload system.

$$q_{k=1..5} = \begin{Bmatrix} \theta_1 \\ \psi_1 \\ \phi_2 \\ \theta_2 \\ \psi_2 \end{Bmatrix} \tag{3.1}$$

The equations of motion of the dynamic system are derived using Lagrange's equations. For modeling purposes, various components of the system are described using three frames of reference: The inertial reference frame $\{I\}$, the reference frame attached to the tow cable $\{T\}$, and the body reference frame attached to the parafoil-payload system $\{B\}$ as shown in Figure 3.2.

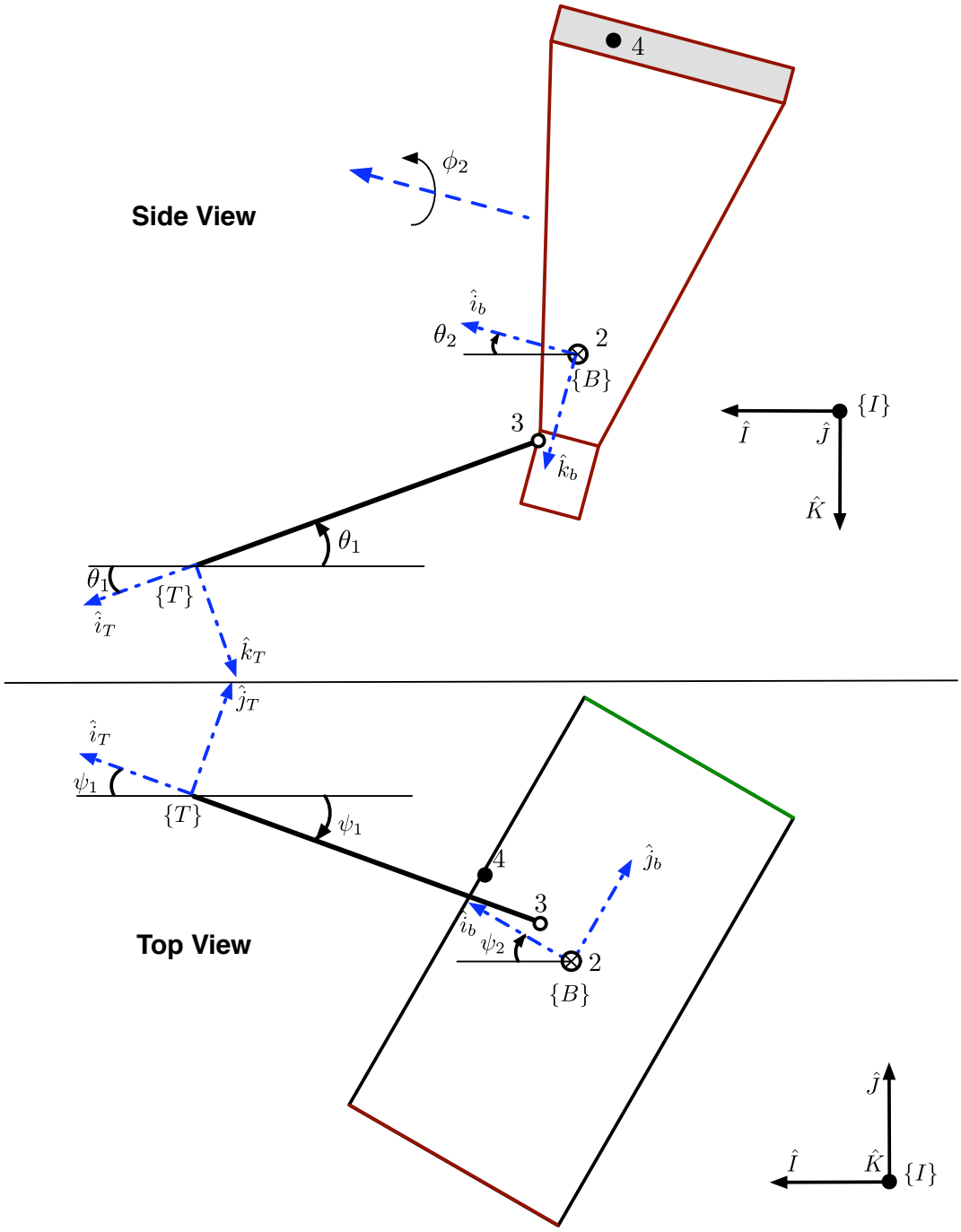

Figure 3.2. Schematic diagram of the states and reference frames of the model.

3.2.1 Rotation Matrices

The $\{T\}$ frame of reference is obtained by first rotating the inertial frame of reference $\{I\}$ about the $\hat{K}$ axis by angle ψ_1 and then by an angle θ_1 about $-\hat{j}_T$ axis as shown in the Figure 3.2. Thus the rotation matrix to transform vectors from inertial frame of reference to tow cable reference frame can be written as shown in Equation 3.2.

$$
{}^{T}_{I}\mathbf{R} = \begin{bmatrix} \cos\theta_1 \cos\psi_1 & \cos\theta_1 \sin\psi_1 & \sin\theta_1 \\ -\sin\psi_1 & \cos\psi_1 & 0 \\ -\sin\theta_1 \cos\psi_1 & -\sin\theta_1 \sin\psi_1 & \cos\theta_1 \end{bmatrix} \tag{3.2}
$$

The angular velocity of the tow cable represented in $\{T\}$ frame is represented as shown in Equation 3.3.

$$
\begin{aligned}
{}^{T}\vec{\omega}_T &= -\dot{\theta}_1 \hat{j}_T + \dot{\psi}_1 \hat{K} \\
&= -\dot{\theta}_1 \hat{j}_T + \dot{\psi}_1 \sin\theta_1 \hat{i}_T + \dot{\psi}_1 \cos\theta_1 \hat{k}_T \\
&= \begin{Bmatrix} \sin\theta_1 \dot{\psi}_1 \\ -\dot{\theta}_1 \\ \cos\theta_1 \dot{\psi}_1 \end{Bmatrix}
\end{aligned} \tag{3.3}
$$

The $\{B\}$ frame of reference is obtained by rotating the inertial frame of reference $\{I\}$ through $3-2-1$ Euler angle rotations as shown in the Figure 3.2. Thus the rotation matrix to transform vectors from inertial frame of reference to body reference frame can be written

as shown in Equation 3.4.

$$
{}^{B}_{I}\mathbf{R} = \begin{bmatrix} \cos\theta_2\cos\psi_2 & \cos\theta_2\sin\psi_2 & -\sin\theta_2 \\ -\cos\phi_2\sin\psi_2 + \sin\phi_2\sin\theta_2\cos\psi_2 & \cos\phi_2\cos\psi_2 + \sin\phi_2\sin\theta_2\sin\psi_2 & \sin\phi_2\cos\theta_2 \\ \sin\phi_2\sin\psi_2 + \cos\phi_2\sin\theta_2\cos\psi_2 & -\sin\phi_2\cos\psi_2 + \cos\phi_2\sin\theta_2\sin\psi_2 & \cos\theta_2\cos\phi_2 \end{bmatrix} \tag{3.4}
$$

The angular velocity of the parafoil-payload system can be represented in the $\{B\}$ frame as shown in Equation 3.5

$$
\begin{aligned}
{}^{B}\vec{\omega}_B &= \dot{\phi}_2\hat{i}_b + \dot{\theta}_2\hat{j}_b'' + \dot{\psi}_2\hat{k}_b' \\
&= \dot{\phi}_2\hat{i}_b + \dot{\theta}_2(\cos\phi_2\hat{j}_b - \sin\phi_2\hat{k}_b) + \dot{\psi}_2(-\sin\theta_2\hat{i}_b + \cos\theta_2\sin\phi_2\hat{j}_b + \cos\theta_2\cos\phi_2\hat{k}_b) \\
&= \begin{Bmatrix} \dot{\phi}_2 - \sin\theta_2\dot{\psi}_2 \\ \dot{\theta}_2\cos\phi_2 + \dot{\psi}_2\cos\theta_2\sin\phi_2 \\ \cos\theta_2\cos\phi_2\dot{\psi}_2 - \dot{\theta}_2\sin\phi_2 \end{Bmatrix}
\end{aligned} \tag{3.5}
$$

3.2.2 Kinematics

The absolute position of the CG of the parafoil-payload system can be written in terms of absolute position of the ship, the relative vector representing the tow cable and the relative vector between point of attachment of the cable at parafoil end and the CG of the parafoil payload system.

$$
\vec{r}_2 = \vec{r}_1 + \vec{r}_{3/1} - \vec{r}_{3/2} \tag{3.6}
$$

Note that $\vec{r}_{i/j}$ is the vector from point j to point i.

Differentiating Equation 3.6 we get the velocity of CG of the parafoil-payload system which will be used in Equation 3.8 to calculate kinetic energy of the parafoil-payload sys-

tem.

$$\vec{v}_2 = \vec{v}_1 + \frac{d}{dt}\vec{r}_{3/1} + \vec{\omega}_T \times \vec{r}_{3/1} - \vec{\omega}_B \times \vec{r}_{3/2} \tag{3.7}$$

3.2.3 Lagrange Equations

In classical mechanics, the Lagrangian $\mathcal{L}$ is defined as kinetic energy T minus the potential energy V. In equation form,

$$\mathcal{L} = T - V$$

where, the kinetic energy of the parafoil-payload system can be expressed as the sum of translational and rotational kinetic energy of the parafoil-payload system as shown in Equation 3.8.

$$T = \frac{1}{2}m\vec{v}_2^T\vec{v}_2 + \frac{1}{2}\vec{\omega}_B^T\mathbf{I}\vec{\omega}_B \tag{3.8}$$

The inertia matrix **I** is assumed to be a diagonal matrix as represented in Equation 3.9, due to the symmetry of the parafoil-payload system about body reference frame axes.

$$\mathbf{I} = \begin{bmatrix} I_{xx} & 0 & 0 \\ 0 & I_{yy} & 0 \\ 0 & 0 & I_{zz} \end{bmatrix} \tag{3.9}$$

If z_2 represents the height of the CG of the parafoil-payload system above datum, the potential energy can be expressed as shown in Equation 3.10.

$$V = -mgz_2 \tag{3.10}$$

If Q_k represents a set of generalized forces acting on the system, the generalized form of Euler-Lagrange equations can be written as shown in Equation 3.11

$$\frac{d}{dt}\frac{\partial \mathcal{L}}{\partial \dot{q}_k} - \frac{\partial \mathcal{L}}{\partial q_k} = Q_k \tag{3.11}$$

3.2.4 Generalized Forces

To determine the generalized forces acting on a rigid body, we first write the expression for the virtual work done on a rigid body by n forces $\mathbf{F_i}$ ($i = 1, 2, ..., n$) at points $\mathbf{r_i}$ and $\boldsymbol{M}^*$ moments ($i = 1, 2, ..., M^*$) are acting on the body (27).

$$\begin{aligned} \delta W &= \sum_{k=1}^{m} \left(\sum_{i=1}^{n} \mathbf{F_i} \cdot \frac{\partial \mathbf{r_i}}{\partial \dot{q}_k} + \mathbf{M}^* \cdot \frac{\partial \boldsymbol{\omega}}{\partial \dot{q}_k} \right) \delta q_k \\ &= \sum_{k=1}^{m} Q_k \delta q_k \end{aligned} \tag{3.12}$$

For the case of a parafoil-payload system the aerodynamic force $\mathbf{F}_4$ and moment $\mathbf{M}_4$ acting at the aerodynamic center 4, at a distance $\mathbf{r}_4$ from the CG contribute as generalized forces. So Equation 3.12 can be written in more specific form as shown in Equation 3.13.

$$\begin{aligned} \delta W &= \sum_{k=1}^{m} \left(\mathbf{F}_4 \cdot \frac{\partial \mathbf{r}_4}{\partial \dot{q}_k} + \mathbf{M}_4 \cdot \frac{\partial \boldsymbol{\omega}}{\partial \dot{q}_k} \right) \delta q_k \\ &= \sum_{k=1}^{m} Q_k \delta q_k \end{aligned} \tag{3.13}$$

The variation of $\vec{v}_4$ can be represented in terms of generalized coordinates.

$$\sum_{k=1}^{m} \frac{\partial \dot{\mathbf{r}}_4}{\partial \dot{q}_k} \delta q_k = \frac{\partial \dot{\mathbf{r}}_4}{\partial \dot{\theta}_1} \delta\theta_1 + \frac{\partial \dot{\mathbf{r}}_4}{\partial \dot{\psi}_1} \delta\psi_1 + \frac{\partial \dot{\mathbf{r}}_4}{\partial \dot{\phi}_2} \delta\phi_2 + \frac{\partial \dot{\mathbf{r}}_4}{\partial \dot{\theta}_2} \delta\theta_2 + \frac{\partial \dot{\mathbf{r}}_4}{\partial \dot{\psi}_2} \delta\psi_2$$

$$\sum_{k=1}^{m} \frac{\partial \boldsymbol{\omega}_B}{\partial \dot{q}_k} \delta q_k = \frac{\partial \boldsymbol{\omega}_B}{\partial \dot{\theta}_1} \delta\theta_1 + \frac{\partial \boldsymbol{\omega}_B}{\partial \dot{\psi}_1} \delta\psi_1 + \frac{\partial \boldsymbol{\omega}_B}{\partial \dot{\phi}_2} \delta\phi_2 + \frac{\partial \boldsymbol{\omega}_B}{\partial \dot{\theta}_2} \delta\theta_2 + \frac{\partial \boldsymbol{\omega}_B}{\partial \dot{\psi}_2} \delta\psi_2 \tag{3.14}$$

Thus the five generalized forces for five dynamic equations are summarized in Equation 3.15.

$$\begin{aligned} Q_{\theta_1} &= \mathbf{F}_4 \cdot \frac{\partial \dot{\mathbf{r}}_4}{\partial \dot{\theta}_1} + \mathbf{M}_4 \cdot \frac{\partial \boldsymbol{\omega}_B}{\partial \dot{\theta}_1} \\ Q_{\psi_1} &= \mathbf{F}_4 \cdot \frac{\partial \dot{\mathbf{r}}_4}{\partial \dot{\psi}_1} + \mathbf{M}_4 \cdot \frac{\partial \boldsymbol{\omega}_B}{\partial \dot{\psi}_1} \\ Q_{\phi_2} &= \mathbf{F}_4 \cdot \frac{\partial \dot{\mathbf{r}}_4}{\partial \dot{\phi}_2} + \mathbf{M}_4 \cdot \frac{\partial \boldsymbol{\omega}_B}{\partial \dot{\phi}_2} \\ Q_{\theta_2} &= \mathbf{F}_4 \cdot \frac{\partial \dot{\mathbf{r}}_4}{\partial \dot{\theta}_2} + \mathbf{M}_4 \cdot \frac{\partial \boldsymbol{\omega}_B}{\partial \dot{\theta}_2} \\ Q_{\psi_2} &= \mathbf{F}_4 \cdot \frac{\partial \dot{\mathbf{r}}_4}{\partial \dot{\psi}_2} + \mathbf{M}_4 \cdot \frac{\partial \boldsymbol{\omega}_B}{\partial \dot{\psi}_2} \end{aligned} \tag{3.15}$$

3.2.5 Dynamic Equations

Using Equation 3.11 and the generalized forces derived in Equation 3.15, the equations of motion were derived in a symbolic math code Maple. The script is given in Appendix B. Equation 3.16 shows the five dynamic equations representing the motion of a towed-parafoil-payload system.

$$\begin{bmatrix} A_{11} & A_{12} & A_{13} & A_{14} & A_{15} \\ A_{21} & A_{22} & A_{23} & A_{24} & A_{25} \\ A_{31} & A_{32} & A_{33} & A_{34} & A_{35} \\ A_{41} & A_{42} & A_{43} & A_{44} & A_{45} \\ A_{51} & A_{52} & A_{53} & A_{54} & A_{55} \end{bmatrix} \begin{Bmatrix} \ddot{\theta}_1 \\ \ddot{\psi}_1 \\ \ddot{\phi}_2 \\ \ddot{\theta}_2 \\ \ddot{\psi}_2 \end{Bmatrix} = \begin{Bmatrix} B_1 \\ B_2 \\ B_3 \\ B_4 \\ B_5 \end{Bmatrix} \tag{3.16}$$

The individual terms of the A and B matrix are given in Appendix A.

3.3 Aerodynamic Model

The external forces and moments acting on the system are the aerodynamic forces and moments acting at point 4. Refer Figure 3.3 for the aerodynamic forces acting at point 4. These forces act in the wind frame $\{W\}$, the x axis of which is attached to the direction of the velocity of point 4 with respect to the wind, and z axis is perpendicular to x-axis and in the plane of symmetry of the canopy.

The velocity of the aerodynamic center, point 4 with respect to wind can be expressed as shown in Equation 3.17.

$$\vec{v}_{4/w} = \vec{v}_2 + \vec{\omega}_B \times \vec{r}_{4/2} - \vec{v}_w \tag{3.17}$$

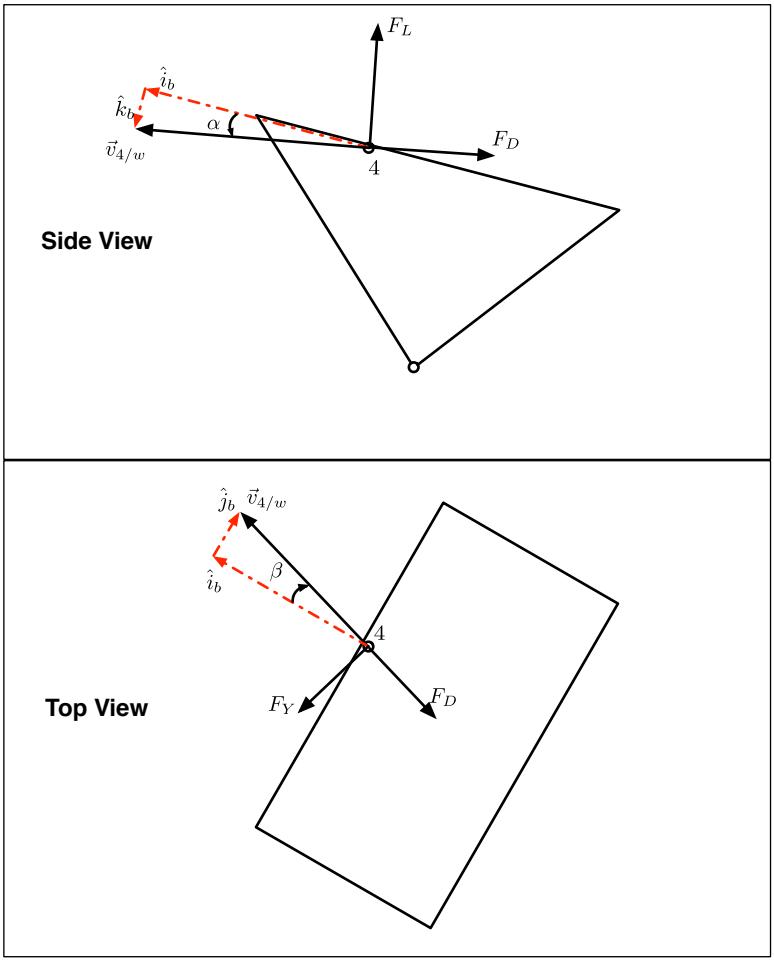

Figure 3.3. Aerodynamic forces

The angle of attack and the side-slip angle are defined similar to standard aircraft equations as shown in Equations 3.18 and 3.19.

$$\alpha = \tan^{-1}\left(\frac{v_{4/w,z}}{v_{4/w,x}}\right) \tag{3.18}$$

$$\beta = \sin^{-1}\left(\frac{v_{4/w,y}}{|\vec{v}_{4/w}|}\right) \tag{3.19}$$

Equation 3.20 shows the transformation of unit vectors from wind frame to body frame of reference.

$$\begin{Bmatrix} \hat{i}_b \\ \hat{j}_b \\ \hat{k}_b \end{Bmatrix} = \begin{bmatrix} \cos\alpha & 0 & -\sin\alpha \\ 0 & 1 & 0 \\ \sin\alpha & 0 & \cos\alpha \end{bmatrix} \begin{bmatrix} \cos\beta & -\sin\beta & 0 \\ \sin\beta & \cos\beta & 0 \\ 0 & 0 & 1 \end{bmatrix} \begin{Bmatrix} \hat{i}_w \\ \hat{j}_w \\ \hat{k}_w \end{Bmatrix} \tag{3.20}$$

Thus the rotation matrix which converts vectors from wind frame to body frame can be written as shown in Equation 3.21

$${}^{B}_{W}\mathbf{R} = \begin{bmatrix} \cos\alpha\cos\beta & -\cos\alpha\sin\beta & -\sin\alpha \\ \sin\beta & \cos\beta & 0 \\ \sin\alpha\cos\beta & -\sin\alpha\sin\beta & \cos\alpha \end{bmatrix} \tag{3.21}$$

The aerodynamic model of an equivalent 500 sq. ft. parafoil, with the payload capacity of 500 lbs is used for modeling purposes as described in Reference (28). One exception in this model is the value of the yaw damping coefficient C_{nr}, the value of which is assumed to be half the value assumed in (28). Also the coefficients in rolling and yawing moment which are functions of asymmetric brake deflection δ_a have been doubled with the assumption that the system is more sensitive to control inputs in the towed condition as compared to that in

free flight. The lift and drag coefficients are the functions of angle of attack and symmetric brake deflections. Since the absolute value of asymmetric deflection of trailing edge adds to the lift of the parafoil, the net lift changes due to absolute value of δ_a too. The lift and drag coeffcients are shown in Equations 3.22 and 3.23.

$$C_L = C_{L_0} + C_{L_\alpha}\alpha + C_{L_{\delta_s}}\delta_s + C_{L_{\delta_a}}|\delta_a| \tag{3.22}$$

$$C_D = C_{D_0} + (C_{D_\alpha} + C_{D_{\delta_s}}\delta_s)C_L^2 \tag{3.23}$$

The side force acting on the parafoil is the function of side slip angle β, angle of attack α, and asymmetric brake deflection δ_a as shown in Equation 3.24.

$$C_Y = (C_{Y_\beta} + C_{Y_{\alpha\beta}}\alpha)\beta + C_{Y_{\delta_a}}\delta_a \tag{3.24}$$

The aerodynamic pitching moment coefficient takes its form as described in chapter 2, which is derived from the static stability analysis done by Thomas Goodrick (6).

$$C_m = C_{m_0} + \frac{dm_{pl}}{m}\left(\frac{1}{c} + \frac{\rho C_{B_0}}{2W/S}\right)(C_D\cos\alpha - C_L\sin\alpha) + C_{m_q}\frac{qc}{2|\vec{v}_{4/w}|} \tag{3.25}$$

Here,

m_{pl} = Mass of the payload

d = Vertical distance between the CG of the canopy and the payload in $\{B\}$ frame

C_{B_0} = Buoyancy constant

W = Total weight of the parafoil-payload system

The rolling moment and yawing moment coefficients are typical lateral coefficients, function of side slip angle β, angle of attack α and asymmetric brake deflections δ_a. The damping terms are also included, which are functions of rolling rate and yawing rate respectively.

$$C_l = \left(C_{l_\beta} + C_{l_{\alpha\beta}}\alpha\right)\beta + C_{l_{\delta_a}}\delta_a + \frac{b}{2|\vec{v}_{4/w}|}\left(C_{l_p}p + C_{l_r}r\right) \tag{3.26}$$

$$C_n = \left(C_{n_\beta} + C_{n_{\alpha\beta}}\alpha\right)\beta + C_{n_{\delta_a}}\delta_a + \frac{b}{2|\vec{v}_{4/w}|}\left(C_{n_p}p + C_{n_r}r\right) \tag{3.27}$$

The values of all the sub-coefficients are listed in Table 3.1.

Finally the aerodynamic forces are calculated using the standard aircraft equations.

$$\begin{aligned} L &= \frac{1}{2}\rho|\vec{v}_{4/w}|^2 S C_L \\ Y &= \frac{1}{2}\rho|\vec{v}_{4/w}|^2 S C_Y \\ D &= \frac{1}{2}\rho|\vec{v}_{4/w}|^2 S C_D \end{aligned}$$

And the total external forces acting on point 4 can be represented in body reference

Table 3.1.
Aerodynamic Sub-Coefficients

Force Coefficients			**Moment Coefficients**		
Symbol	Value	Units	Symbol	Value	Units
C_{D_0}	0.14	n.d.	C_{l_β}	0.2865	rad^{-1}
C_{D_α}	0.25	rad^{-1}	$C_{l_{\alpha\beta}}$	-5.9091	rad^{-2}
$C_{D_{\delta_s}}$	0.2	n.d.	$C_{l_{\delta_a}}$	-0.0126	n.d.
C_{Y_β}	-0.2865	rad^{-1}	C_{l_p}	-0.15	rad^{-1}
$C_{Y_{\alpha\beta}}$	-0.3283	rad^{-2}	C_{l_r}	0.0775	rad^{-1}
$C_{Y_{\delta_a}}$	0.1368	n.d.	C_{m_0}	-0.33	n.d.
C_{L_0}	0.375	n.d.	C_{m_q}	-6.39	rad^{-1}
C_{L_α}	2.1486	rad^{-1}	C_{n_β}	0.4011	rad^{-1}
$C_{L_{\delta_s}}$	0.2	n.d.	$C_{n_{\alpha\beta}}$	-0.9848	rad^{-2}
$C_{L_{\delta_a}}$	0.1	n.d.	$C_{n_{\delta_a}}$	0.038	n.d.
			C_{n_p}	0.023	rad^{-1}
			C_{n_r}	-0.0468	rad^{-1}

frame as

$$ {}^{B}F_4 = {}^{B}_{W}\mathbf{R} \begin{Bmatrix} -D \\ -Y \\ -L \end{Bmatrix} \tag{3.28} $$

The aerodynamic moments acting on parafoil-payload system are

$$ \begin{aligned} M_{4,x} &= \frac{1}{2}\rho|\vec{v}_{4/w}|^2 S C_l b \\ M_{4,y} &= \frac{1}{2}\rho|\vec{v}_{4/w}|^2 S C_m c \\ M_{4,z} &= \frac{1}{2}\rho|\vec{v}_{4/w}|^2 S C_n b \end{aligned} $$

3.3.1 Control Inputs

As discussed in Chapter 2, the primary source of steering a parafoil is by deflecting the trailing edge with the help of control lines. The control input is incorporated into the model,

in a way that the net aerodynamic forces and moments change due to the trailing edge deflection. The most common way of modeling the trailing edge is with the help of a dimensionless quantity called δ. Refer Figure 3.4. If d represents the length of the chord deflected due to the pulling of trailing edge, then the dimensionless control input δ is defined as shown in Equation 3.29,

$$\delta = \frac{d}{c} \tag{3.29}$$

So, for example, if the trailing edge at both the sides of the span is deflected in such a way that the $d = 0.3c$, then,

$$\delta_s = 0.3 \tag{3.30}$$

Now, if the right brake is further pulled down so that on the right side $d = 0.5c$, then

$$\begin{aligned} \delta_s &= 0.3 \\ \delta_a &= 0.2 \end{aligned}$$

Figure 3.5 shows the steady state roll angle ϕ_{2_0} for various possible input conditions. The procedure used to compute steady state values of the states, is described in detail in Section 4.3. It can be seen that the steady state roll angle increases with increase in asymmetric brake deflection at right side of the canopy. When symmetric brake deflection $\delta_s = 0$, there is a particular value of asymmetric brakes, which is $\delta_a = 0.3$ in this case, after which there is no steady state and system goes unstable. This is a possible lockout stage. Also, as the symmetric brake deflection increases, the effect of asymmetric brakes keeps on diminish-

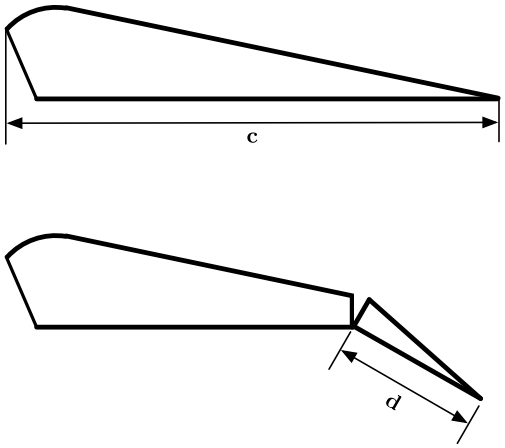

Figure 3.4. Modeling control input or parafoil brake deflection

ing.

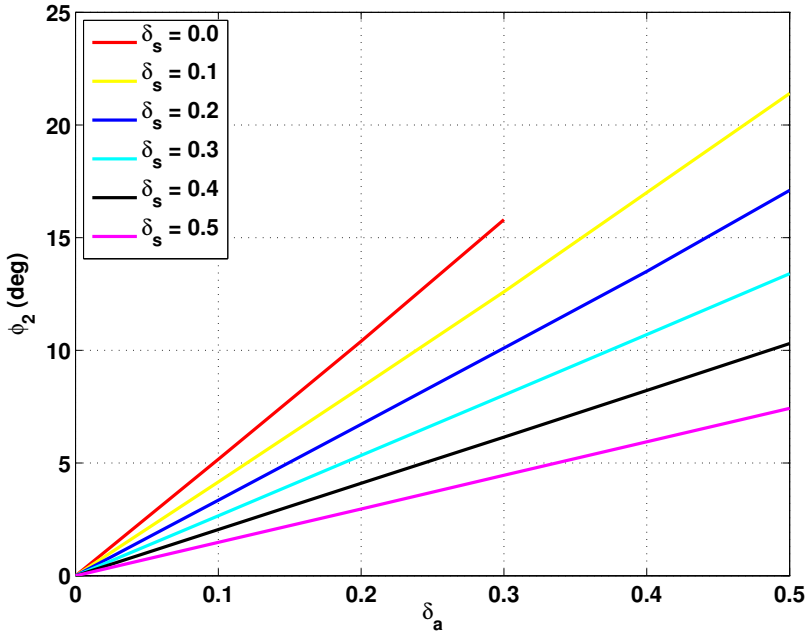

Figure 3.5. Steady state roll angle ϕ_{2_0} for various control inputs

The similar effect is observed with yaw angle also as shown in Figure 3.6, though the net effect on yaw angle is lesser than that of roll angle. The maximum steady state yaw angle is $\psi_{2_0} = 8.3$ degrees. The possible reason for this is due to increasing off plane tow

cable angle in negative direction as shown in Figure 3.7. The absence of any steady state for $\delta_s = 0$ and $\delta_a > 0.3$ is evident in both the lateral states, ψ_1 and ψ_2.

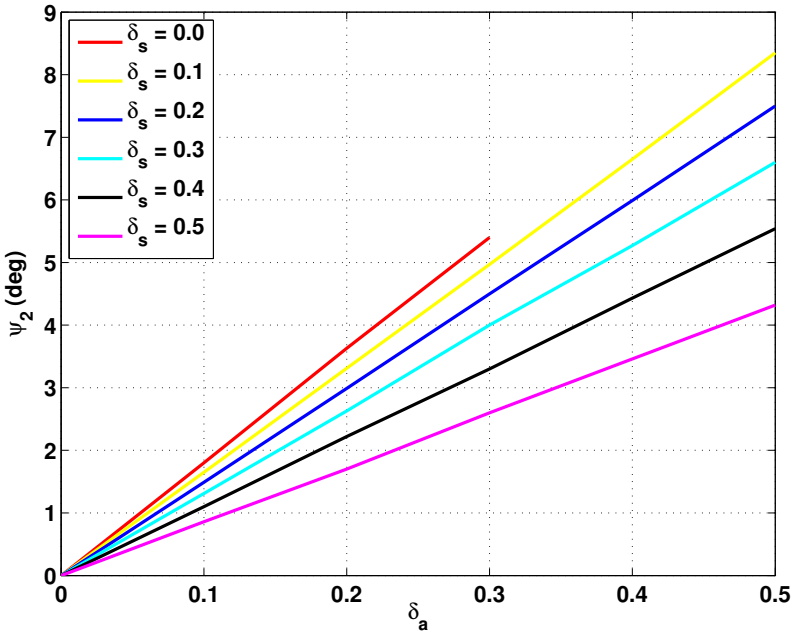

Figure 3.6. Steady state yaw angle ψ_{2_0} for various control inputs

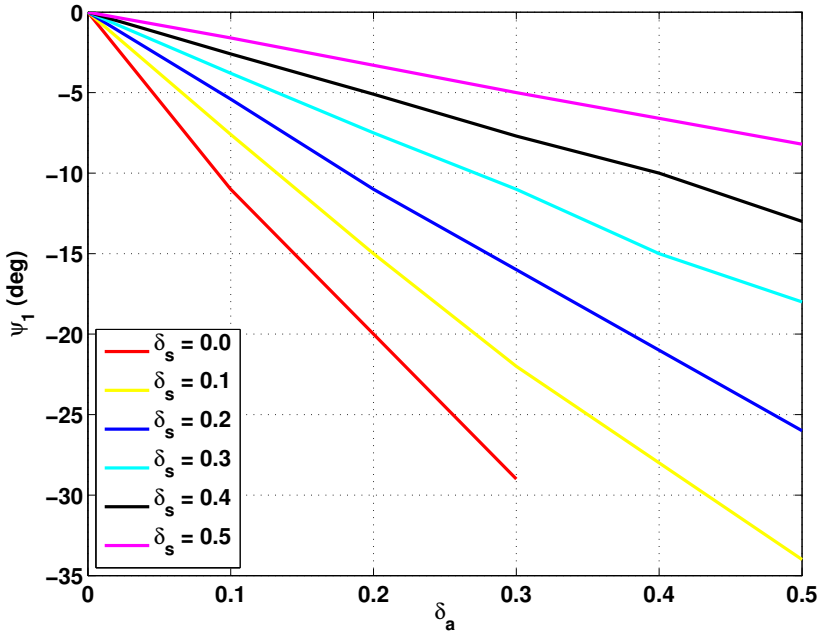

Figure 3.7. Steady state off plane tow angle ψ_{1_0} for various control inputs

3.4 Geometric and Inertial Properties

Due to the large distance between the parafoil canopy and the payload, the geometric properties of the system play an important role in the overall system dynamics. The parafoil used for the simulation purpose has the properties of the one which is being used by Craft Engineering Associates for experimental testing, refer Figure 3.8. It is a 13 cell zero porosity parafoil from Flight Concepts International, Inc. of Norcross, Georgia. The parafoil has a rectangular design (10.6 m span by 4.16 m chord) with a 3:1 aspect ratio, and has been used on commercial powered parachutes. The parafoil has a lift capacity of over 4,000 Newtons and is well suited for a 250 to 300 kg cargo delivery system.

Figure 3.8. Parafoil used for testing. (courtesy: Flight Concepts Int'l, Inc. See Appendix D for the documentation of the permission to republish this image)

A rectangular frame which will house the payload and related avionics is shown in Figure 3.9. It is 1.25 meters long, 1.65 meters wide and 1.07 meters tall. The tow cable attachment is at height of 0.8 meters from the bottom and the attachment is 0.6 meters wide.

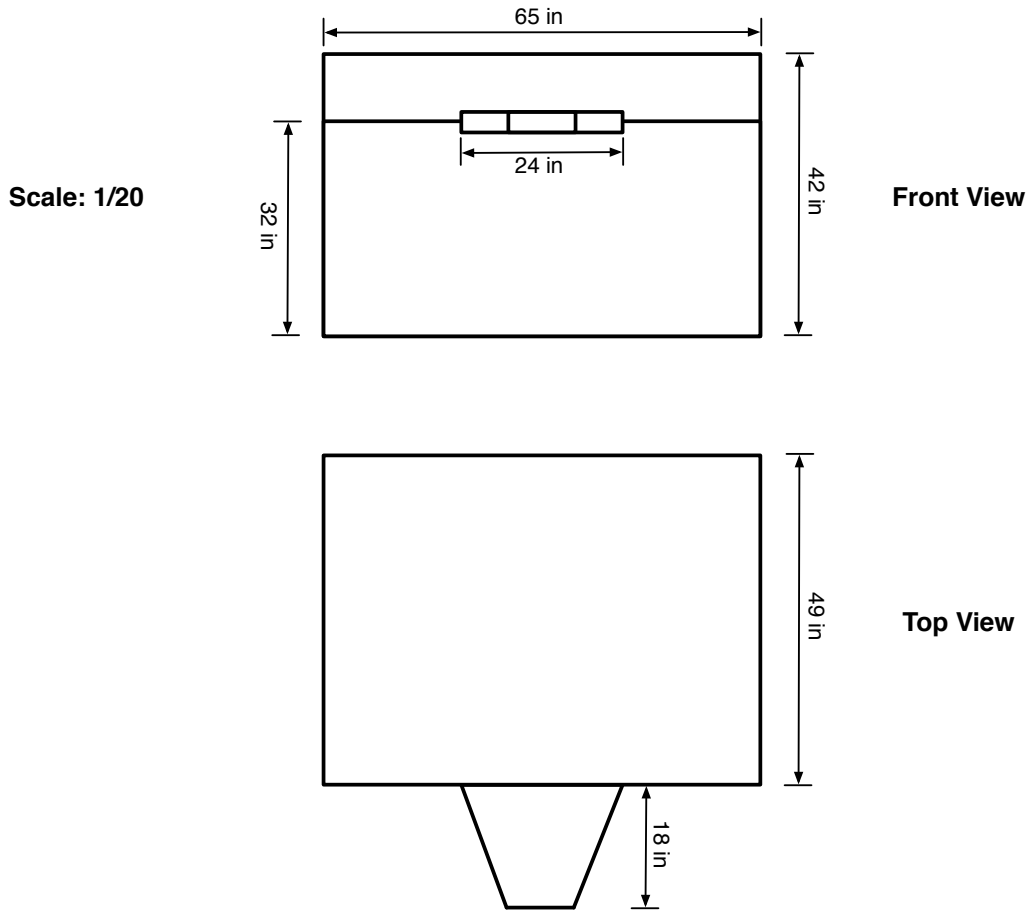

Figure 3.9. Payload dimensions

Some of the important model parameters are listed in Table 3.2.

Table 3.2.
Model Parameters

Object	Parameter	Symbol	Value	Units
Canopy	Span	b	10.6	meters
	Chord	c	4.16	meters
	Arch	a	2.28	meters
	Thickness	t	0.61	meters
	Area	S	50	sq. mts
	Mass	m_{cpy}	6.44	kg
	Mass of air	m_{air}	21.67	kg
	Apparent mass	m_{app}	0.8*m_{air}	kg
Payload	Max weight	m_{pl}	226.8	kg
	Dim in Inertial X	pl_x	1.25	meters
	Dim in Inertial Y	pl_y	1.65	meters
	Dim in Inertial Z	pl_z	1.07	meters

3.4.1 Inertia Calculations

Since the parafoil-payload system is considered to be a rigid body, to model the system dynamics more accurately, the system mass and inertia properties are calculated using actual values. The mass of the air, large distance between parafoil canopy and payload and the apparent mass effects have a significant role in the overall CG and inertia calculations. Consider the parafoil-payload system in side view as shown in the Figure 3.10. Due to the symmetry of both the canopy and the payload along the inertial Y axis, all the center of masses are assumed to be in the inertial XZ plane. Point C represents the mass center of the canopy, which is also the aerodynamic center where all aerodynamic forces and moments are assumed to act. Point P is the payload mass center. The top edge of the payload and the vertical passing through the CG of the payload are considered to reference datum for CG calculations, as indicated in Figure 3.10. x_c and z_c are the horizontal and vertical distances

of the canopy mass center from the datum. Similarly x_p and z_p locate the payload CG. It should be noted that $x_p = 0$, since the reference datum is assumed to be passing through payload CG. The total mass of the canopy m_{cpy}, mass of the air m_{air} and the apparent mass of the air m_{app} is denoted by m_c.

$$m_c = m_{cpy} + m_{air} + m_{app} \tag{3.31}$$

Thus the overall CG of the system can be calculated by using Equations 3.32 and 3.33.

$$x_{cg} = \frac{m_{pl}x_p + m_c x_c}{m_{pl} + m_c} \tag{3.32}$$

$$z_{cg} = \frac{m_{pl}z_p + m_c z_c}{m_{pl} + m_c} \tag{3.33}$$

The payload moments of inertia about its mass center P are calculated using standard formulae for a rectangular solid box.

$$I_{x_{pl}} = \frac{m_{pl}\left(pl_y^2 + pl_z^2\right)}{12} \tag{3.34}$$

$$I_{y_{pl}} = \frac{m_{pl}\left(pl_x^2 + pl_z^2\right)}{12} \tag{3.35}$$

$$I_{z_{pl}} = \frac{m_{pl}\left(pl_x^2 + pl_y^2\right)}{12} \tag{3.36}$$

The parafoil canopy is assumed to of a rectangular planform, with very less thickness as compared to its span and chord. So the formulae of a rectangular plate are used to model the inertia of the parafoil canopy (28).

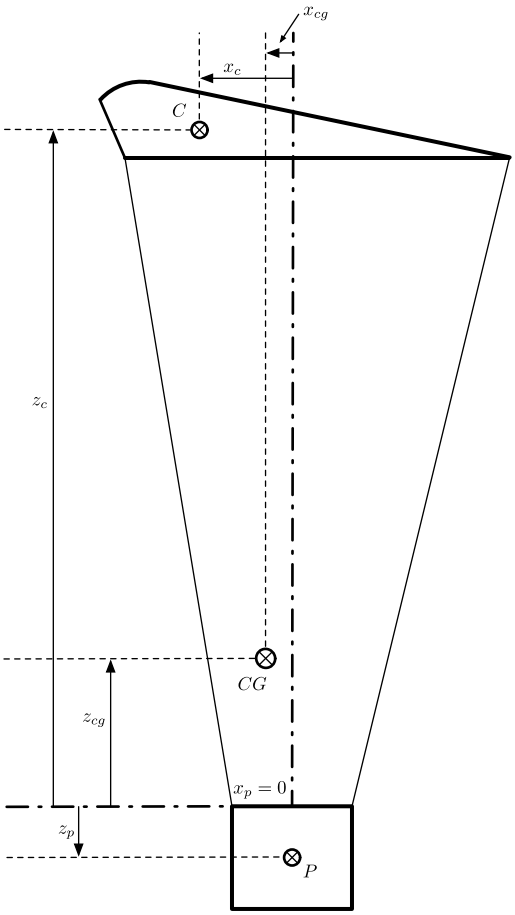

Figure 3.10. Side view of a parafoil payload system for net CG calculation

$$I_{x_c} = \frac{m_c b^2}{12} \tag{3.37}$$

$$I_{y_c} = \frac{m_c c^2}{12} \tag{3.38}$$

$$I_{z_c} = \frac{m_c \left(b^2 + c^2\right)}{12} \tag{3.39}$$

Finally using parallel axis theorem, the total inertia about all three axes are calculated using Equations 3.40 to 3.42.

$$I_{xx} = I_{x_{pl}} + I_{x_c} + m_{pl}\left(z_p - z_{cg}\right)^2 + m_c\left(z_c - z_{cg}\right)^2 \tag{3.40}$$

$$I_{yy} = I_{y_{pl}} + I_{y_c} + m_{pl}\left(z_p - z_{cg}\right)^2 + m_c\left(z_c - z_{cg}\right)^2 \tag{3.41}$$

$$I_{zz} = I_{z_{pl}} + I_{z_c} + m_{pl}\left(x_p - x_{cg}\right)^2 + m_c\left(x_c - x_{cg}\right)^2 \tag{3.42}$$

3.5 2D Simulation Results

To analyze the dynamics of the towed parafoil-payload system, a longitudinal flight simulation was developed. In this study, only the variables affecting the longitudinal flight are studied for their effect on overall dynamics. Firstly the steady state calculations are made using static analysis to determine the steady state values of in-plane tow angle θ_1 and the pitch angle of the parafoil-payload system, θ_2. This exercise is repeated for various ship velocities and a range of payload weights. Figure 3.11 shows the variation of these two angles.

It can be observed that for a specific payload weight, there is a minimum ship speed

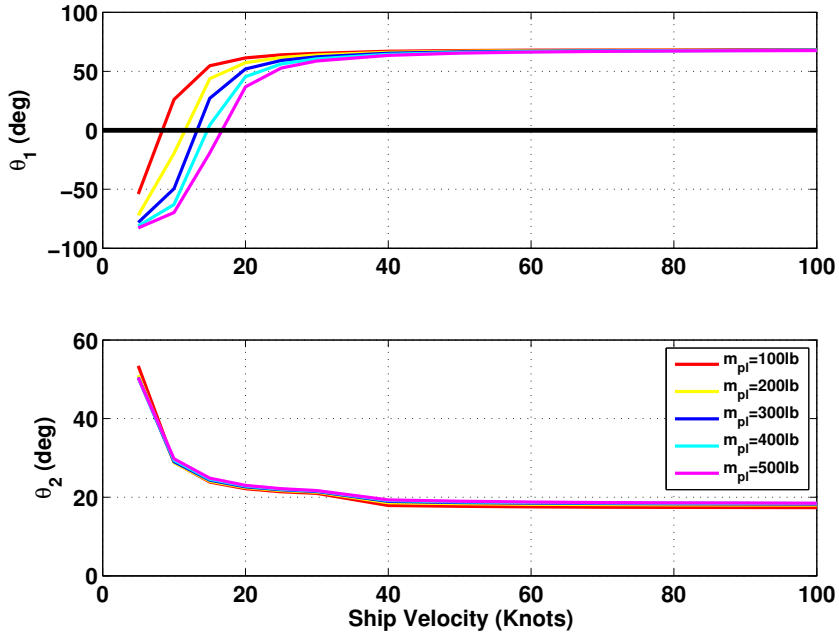

Figure 3.11. Steady state values of in-plane tow angle θ_1 and pitch angle θ_2

required to keep the parafoil-payload system above the ground in steady state. For example, if the payload weight is $m_{pl} = 300$ lb, then the minimum ship speed is about 13 knots to keep it flying behind the ship in steady state. In the first subplot in Figure 3.11 the intersection of solid horizontal black line with the plots, indicate this critical ship speed for different payload weights. When the ship speed increases beyond 40 knots, the steady state in-plane tow angle becomes independent of the payload mass. The ship speed is high enough for the parafoil-payload system to remain afloat at a particular height irrespective of the payload weight. Due to the kinematic constraint applied by the tow cable, the steady state value of the in-plane tow angle reaches a constant value for higher ship speeds. The higher ship speed results in higher tension force in the tow cable.

Payload weight, has hardly any effect on the steady state pitch angle, as seen in second subplot of the Figure 3.11. Also, beyond the ship speed of 40 knots, even the ship speed does not have any effect on the steady state pitch angle. So if we select the optimum ship

speed, then it is possible to have a steady longitudinal flight of the parafoil-payload system behind the ship. Figure 3.12 shows the in-plane tow angle for various symmetric brake inputs. The mass of the payload is assumed to be $m_{pl} = 200$lb, equivalent to an average person's weight. It can be seen that beyond the practical ship speed, which is 15 knots, pulling the symmetric brakes reduces the steady state height of the parafoil-payload system slightly. This helps in keeping the tow cable tension in limit due to increasing ship speed.

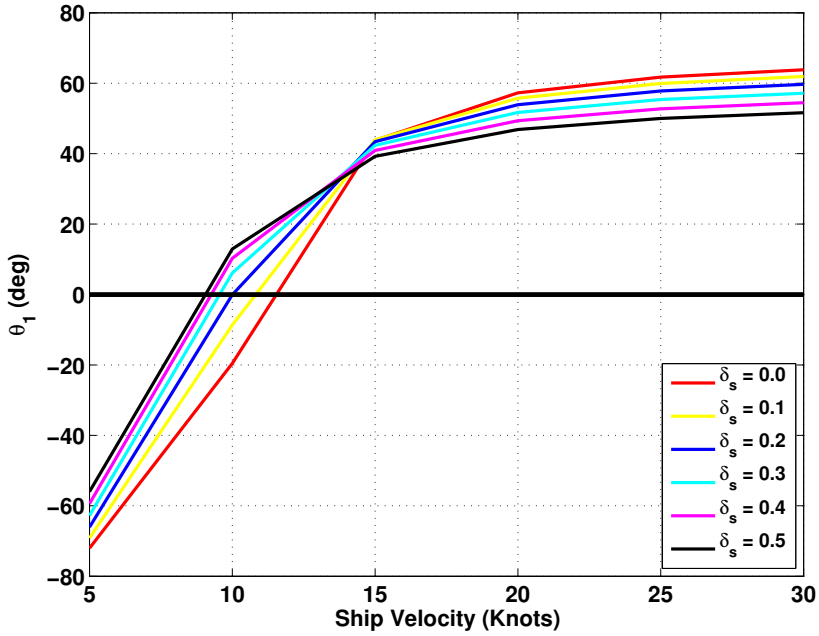

Figure 3.12. Steady state values of in-plane tow angle θ_1 for various symmetric brake inputs

Similarly Figure 3.13 shows the effect of symmetric brake inputs on the steady state pitch angle. Again for all practical values of ship speeds beyond 15 knots, the symmetric brakes increase the steady state picth angle, in accordance with the intuitive observation of the pilot.

In another exercise to test the the longitudinal flight scenario, the system is tested for tow cable release. The ship speed is assumed to be 15 knots, while the payload weight is 200 lbs. The simulation is started with any given values of θ_1 and θ_2. Refer Figures

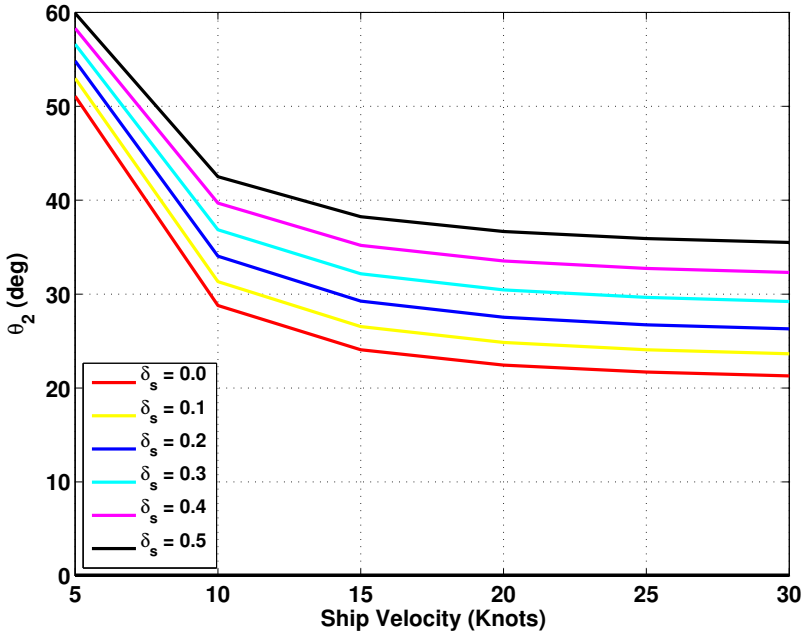

Figure 3.13. Steady state values of pitch angle θ_2 for various symmetric brake inputs

3.14 and 3.15. Until 100 secs, the system comes to a steady state, wherein the steady state values are the same for ship speed of 15 knots and payload weight of 200 lbs as seen in Figure 3.11. After 100 seconds, the tow cable is released at a constant rate. It causes the initial transient where the relative Z distance between the ship and the parafoil-payload system decreases, but soon the parafoil-payload system starts gaining height at a constant rate. Also the relative X distance keeps on increasing at constant rate. Three different cable release rates are studied, $\dot{L} = 0.1$, $\dot{L} = 0.3$ and $\dot{L} = 0.5$ meters per second. As the cable release rate increases, the excess cable is utilized in increasing the relative distance between the ship and the parafoil. In another words, the climb rate of the parafoil-payload system doesnt increase as fast as the cable payout speed.

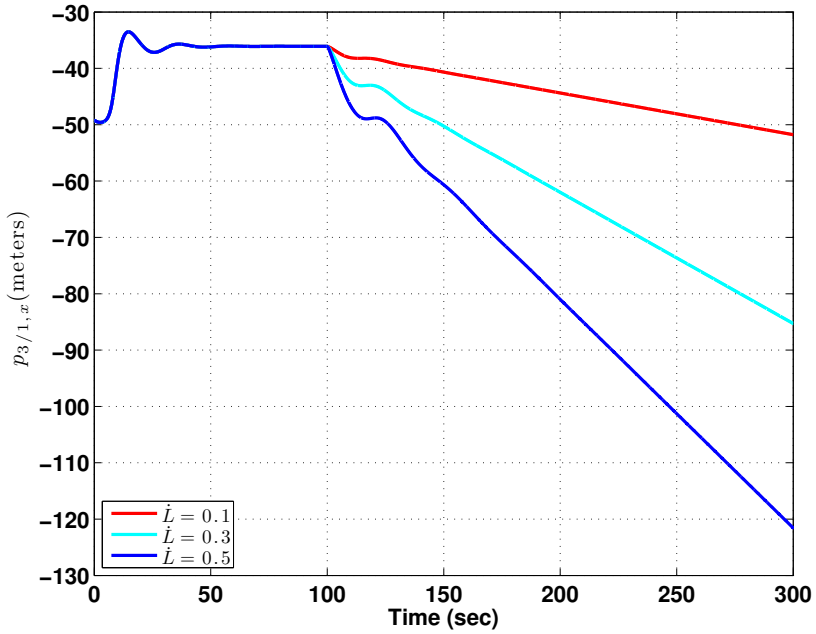

Figure 3.14. Inertial X component of the relative vector between point of attachment at ship and the parafoil-payload system

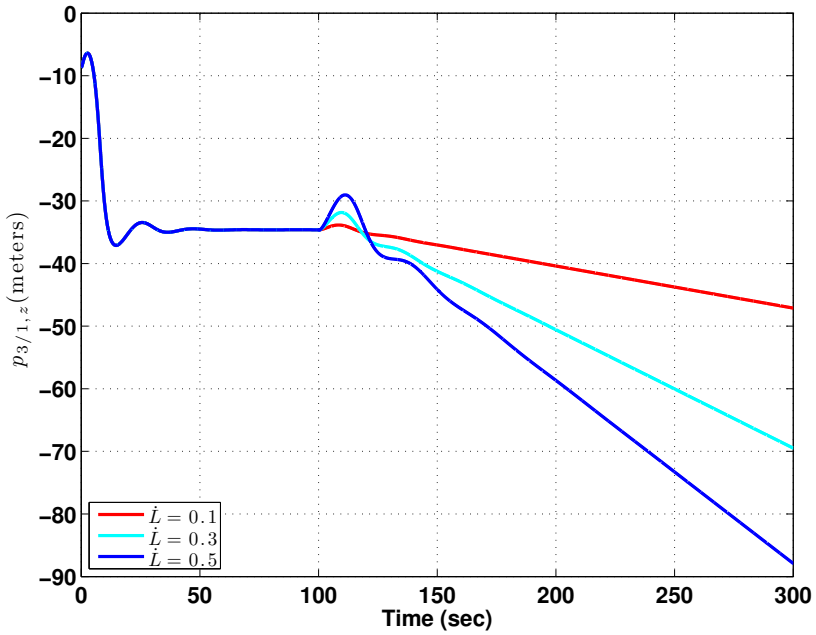

Figure 3.15. Inertial Z component of the relative vector between point of attachment at ship and the parafoil-payload system

3.6 Operator-In-The-Loop Simulation

A real-time simulation tool has been developed in the Intelligent Systems and Control Laboratory in the Mechanical Engineering Department of Michigan Technological University. This tool, developed with dSPACE ds1103 diagnostic board within MATLAB/Simulink and ControlDesk environment, has the capability of testing various control inputs on the towed flight performance. Figure 3.16 shows a view of this system. Two analog joysticks are used to provide calibrated input to the system. The inputs which are provided include:

Figure 3.16. Operator-In-Loop simulation setup

1. Symmetric brake deflection

2. Asymmetric brake deflection

3. Cable payout rate

4. Ship velocity in inertial Y direction

The ControlDesk console has the capabilities of recording all the flight variables in a way analogous to an aircraft in flight. The towed parafoil-payload system has been extensively tested in this open-loop flight scenario before understanding various key issues during towed deployment. One major concern is that of lockout, which will be discussed more in detail in the Chapter 4. The lockout phenomenon has been simulated and the reasons and conditions under which this instability occurs is analyzed.

4. Stability Analysis

When a pilot tows behind a tow vehicle using a paraglider, one of his main concerns is to avoid a peculiar unstable flight condition called lockout. The purpose of this chapter is to model and simulate lockout by analyzing the stability of the parafoil-payload system. This chapter is organized as follows. Section 4.1 presents a motivation for considering stability analysis of towed flight systems. Section 4.2 describes the linear model used for analysis. The steady state fight calculations used for linearization are illustrated in Section 4.3. Comparison of the nonlinear and linear models for disturbances is illustrated by simulation in Section 4.4. Section 4.5 presents the stability of the system as a function of specific flight conditions and physical parameters. The chapter concludes with the summary of results in Section 4.6 and motivation and goals of a control strategy to be developed and presented in the Chapter 5.

4.1 Motivation

The main difference between a pilot flying a paraglider in towed flight as compared to free flight is the tow cable tension acting on the vehicle. In towed flight, it is essential for the velocity vector of the tow vehicle and the wind relative velocity of the vehicle to lie in the same vertical plane. If the vehicle is displaced away from the path of the towing

vehicle, the pilot is taught to bring it back behind the tow vehicle, using the parafoil brakes and weight shifting techniques. If this control is not provided in time, or if the pilot provides an over-control, the towed system can reach a configuration, wherein no matter how much control input is provided, the system will never come back to its steady state and eventually the towed system will crash. This instability is called 'lockout'. One of the main factors contributing to lockout is the tow line tension. As described in the United States Hangliding and Paragliding Association (USHGA) towing manual (29), the following are three signs of an impending lockout situation:

1. A lockout could occur if the pilot is pulled in front of the paraglider canopy by more than 45°, i.e. $\theta_2 > 45^\circ$ or the angle of attack $\alpha > 45^\circ$ in steady flight. This situation can occur due to excessive tension in the tow cable.

2. A lockout could occur if the flight path of the paraglider diverges away from the velocity vector of the towed vehicle by more than 45°, i.e. $\psi_1 > 45^\circ$.

3. A lockout could occur if the canopy rolls by an angle more than 45°, i.e. $\phi_2 > 45^\circ$.

To avoid lockout, it is essential to understand the main flight conditions and physical parameters which can cause it. The main causes are listed below (30):

1. A sudden gust of wind causing the parafoil canopy to roll.

2. Over control of brakes while making a correction to bring the system to a desired steady state flight condition

3. Launching in cross wind conditions

Although lockout is well understood amongst pilots, very little analysis has been done to explain it. The purpose of this study is to analytically quantify the physical parameters, control inputs and flight conditions which can lead to this unstable flight scenario.

4.2 Linear Model

4.2.1 Lyapunov's Linearization Method

The stability analysis approach followed in this chapter is similar to the one used in Reference (22). Stability of a nonlinear system can be analyzed using Lyapunov's linearization method (31). This method is useful to analyze the stability around the vicinity of an equilibrium point, i.e. local stability. Consider a nonlinear system represented by Equation 4.1.

$$\underline{\dot{x}} = \mathbf{f}\left(\underline{x}, \underline{u}\right) \tag{4.1}$$

Neglecting the higher order terms, the linearized system can be represented as shown in the Equation 4.2.

$$\underline{\dot{x}} = \left(\frac{\partial \mathbf{f}}{\partial \underline{x}}\right)_{(\underline{x}=\underline{x}^*, \underline{u}=\underline{u}^*)} \underline{\Delta x} + \left(\frac{\partial \mathbf{f}}{\partial \underline{u}}\right)_{(\underline{x}=\underline{x}^*, \underline{u}=\underline{u}^*)} \underline{\Delta u} \tag{4.2}$$

where, $[\underline{x}^*, \underline{u}^*]$ is the equilibrium point around which the system is linearized. If the Jacobian of **f** with respect to $\underline{x}$ at $[\underline{x}^*, \underline{u}^*]$ is denoted by **A** and the Jacobian of **f** with respect to $\underline{u}$ at $[\underline{x}^*, \underline{u}^*]$ is denoted by **B**, i.e.

$$\mathbf{A} = \left(\frac{\partial \mathbf{f}}{\partial \underline{x}}\right)_{(\underline{x}=\underline{x}^*, \underline{u}=\underline{u}^*)} \tag{4.3}$$

$$\mathbf{B} = \left(\frac{\partial \mathbf{f}}{\partial \underline{u}}\right)_{(\underline{x}=\underline{x}^*, \underline{u}=\underline{u}^*)} \tag{4.4}$$

the linearization of the nonlinear system in Equation 4.1 around the equilibrium point $[\underline{x}^*, \underline{u}^*]$ can be represented as shown in Equation 4.5.

$$\dot{\underline{x}} = \mathbf{A}\underline{\Delta x} + \mathbf{B}\underline{\Delta u} \tag{4.5}$$

The stability of the system can be predicted from Equation 4.5 using theorem 3.1 related to Lyapunov's linearization method cited from Reference (31), which states:

- "If all the eigenvalues of **A** are strictly in the left-half complex plane, then the equilibrium point is asymptotically stable (for the actual nonlinear system)".
- "If at least one eigenvalue of **A** is strictly in the right-half complex plane, then the equilibrium point is unstable".
- "If all the eigenvalues of **A** are in the left-half complex plane, but at least one of them is on the imaginary axis, then one cannot conclude from the linear approximation (the equilibrium point may be stable, asymptotically stable or unstable for the nonlinear system)".

4.2.2 Linearization of Dynamic System

A linear model of the system is first developed around an operating point. The dynamic equations of the parafoil-payload system developed in Chapter 3 are linearized about the

nominal operating flight conditions. The generalized form of the dynamic equations are summarized in Equation 4.6, where $\underline{x}$ is the state vector and $\underline{u}$ is the input vector.

$$\dot{\underline{x}} = \mathbf{F}(\underline{x}, \underline{u}, t) = \left\{ \begin{array}{c} f_1(\underline{x}, \underline{u}, t) \\ f_2(\underline{x}, \underline{u}, t) \\ . \\ . \\ f_{10}(\underline{x}, \underline{u}, t) \end{array} \right\} \tag{4.6}$$

The ten-dimensional state vector $\underline{x}$ is formed by

1. In-plane and off-plane tow cable angles θ_1 and ψ_1,
2. Three Euler angles of the parafoil-payload system; ϕ_2, θ_2 and ψ_2,
3. Angular rates $\dot{\theta}_1$, $\dot{\psi}_1$, $\dot{\phi}_2$, $\dot{\theta}_2$ and $\dot{\psi}_2$.

as shown in Equation 4.7.

$$\underline{x} = \left\{ \begin{array}{c} \theta_1 \\ \psi_1 \\ \phi_2 \\ \theta_2 \\ \psi_2 \\ \dot{\theta}_1 \\ \dot{\psi}_1 \\ \dot{\phi}_2 \\ \dot{\theta}_2 \\ \dot{\psi}_2 \end{array} \right\} \tag{4.7}$$

The input vector consists of symmetric and asymmetric brake angles as represented in Equation 4.8.

$$\underline{u} = \left\{ \begin{array}{c} \delta_s \\ \delta_a \end{array} \right\} \tag{4.8}$$

To linearize the nonlinear dynamic equations, the states and the inputs of the system are expressed as the sum of their nominal operating values and perturbations about them as shown in 4.9

$$\begin{aligned} \underline{x} &= \underline{x}_0 + \underline{\Delta x} \\ \underline{u} &= \underline{u}_0 + \underline{\Delta u} \end{aligned} \tag{4.9}$$

The state vector can be represented as shown in Equation 4.10.

$$\underline{x} = \underline{x}_0 + \underline{\Delta x} = \left\{ \begin{array}{c} \theta_{1_0} + \Delta\theta_1 \\ \psi_{1_0} + \Delta\psi_1 \\ \phi_{2_0} + \Delta\phi_2 \\ \theta_{2_0} + \Delta\theta_2 \\ \psi_{2_0} + \Delta\psi_2 \\ \dot{\theta}_{1_0} + \Delta\dot{\theta}_1 \\ \dot{\psi}_{1_0} + \Delta\dot{\psi}_1 \\ \dot{\phi}_{2_0} + \Delta\dot{\phi}_2 \\ \dot{\theta}_{2_0} + \Delta\dot{\theta}_2 \\ \dot{\psi}_{2_0} + \Delta\dot{\psi}_2 \end{array} \right\} \tag{4.10}$$

The input vector in its perturbations form can be represented as shown in Equation 4.11.

$$\underline{u} = \underline{u}_0 + \underline{\Delta u} = \left\{ \begin{array}{c} \delta_{s_0} + \Delta\delta_s \\ \delta_{a_0} + \Delta\delta_a \end{array} \right\} \tag{4.11}$$

Equation 4.6 is linearized about an equilibrium point $(\underline{x}_0, \underline{u}_0)$ and the linearized dynamic equations of the system are represented in Equation 4.12.

$$\underline{\dot{\Delta x}} = \mathbf{A}\underline{\Delta x} + \mathbf{B}\underline{\Delta u} \tag{4.12}$$

where, **A** and **B** are the Jacobians shown in Equation 4.13 and Equation 4.14.

$$\mathbf{A} = \left[\begin{array}{ccccc} \frac{\partial f_1}{\partial x_1} & \frac{\partial f_1}{\partial x_2} & . & . & \frac{\partial f_1}{\partial x_{10}} \\ \frac{\partial f_2}{\partial x_1} & \frac{\partial f_2}{\partial x_2} & . & . & \frac{\partial f_2}{\partial x_{10}} \\ . & . & . & . & . \\ . & . & . & . & . \\ \frac{\partial f_{10}}{\partial x_1} & \frac{\partial f_{10}}{\partial x_2} & . & . & \frac{\partial f_{10}}{\partial x_{10}} \end{array} \right] \tag{4.13}$$

$$\mathbf{B} = \left\{ \begin{array}{cc} \frac{\partial f_1}{\partial u_1} & \frac{\partial f_1}{\partial u_2} \\ \frac{\partial f_2}{\partial u_1} & \frac{\partial f_2}{\partial u_2} \\ . & . \\ . & . \\ \frac{\partial f_{10}}{\partial u_1} & \frac{\partial f_{10}}{\partial u_2} \end{array} \right\} \tag{4.14}$$

4.3 Steady State Flight

To analyze the stability of a linear model, first the nominal operating point has to be calculated. This operating point consists of a $[\underline{x}_0, \underline{u}_0]$ set consistent with Equation 4.6. This is a unique solution of Equation 3.16, when all the rate terms are set to zero, and is a set of five nonlinear equations. This equation transforms into five equations of the form shown in Equation 4.15

$$\underline{g}\left(\underline{x}_0, \underline{u}_0\right) = 0 \tag{4.15}$$

A code was written using the symbolic manipulation software 'Maple' to auto-generate $\underline{g}$ for any set of physical parameters and $[\underline{x}_0, \underline{u}_0]$. Since a closed form solution was elusive, MATLAB was used to solve Equation 4.15. for each particular steady state input condition $\underline{u}_0$. Since all the rate terms are set to zero, the five unknowns of $\underline{x}_0$ are shown in Equation 4.16.

$$\underline{x}_{0,1..5} = \left\{ \begin{array}{c} \theta_{1_0} \\ \psi_{1_0} \\ \phi_{2_0} \\ \theta_{2_0} \\ \psi_{2_0} \end{array} \right\} \tag{4.16}$$

The steady state solution is then used as an operating point in another Maple code to auto-generate the linear model of the system. For example, consider the tow vehicle moving at a constant speed of 13 knots, i.e. 6.68 meters per second. A payload of 200 lbs (90.7 kg) is being towed by the 500 square foot (46 meter square) parafoil canopy. The steady state

values of the states for a symmetric brake deflection of $\delta_{s_0} = 0.2$ and an asymmetric brake deflection of $\delta_{a_0} = 0.1$ are shown in Equation 4.17. The steady state configuration is shown in Figure 4.1 which is a snapshot of a MATLAB real-time animation software.

$$\begin{Bmatrix} \theta_{1_0} \\ \psi_{1_0} \\ \phi_{2_0} \\ \theta_{2_0} \\ \psi_{2_0} \end{Bmatrix} = \begin{Bmatrix} 32.44^\circ \\ -6.16^\circ \\ 3.32^\circ \\ 29.29^\circ \\ 1.27^\circ \end{Bmatrix} \tag{4.17}$$

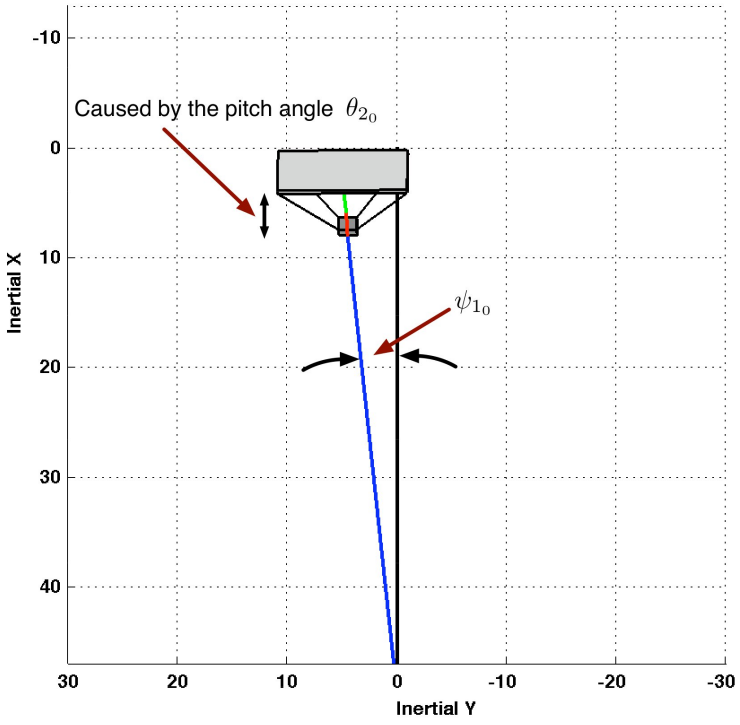

Figure 4.1. Steady state flight condition for symmetric brake input $\delta_{s_0} = 0.2$ and asymmetric brake input $\delta_{a_0} = 0.1$

It can be observed that due to the asymmetric brake deflection, the system yaws in the

positive direction, rolls in positive direction and the tow line sways away from the ship velocity vector in the positive inertial Y direction. In the ensuing analysis the linear model of the system is developed about nominal operating points and then the stability of the system is analyzed using the eigenvalue approach described earlier.

4.4 Linear and Nonlinear Model Comparison

Before analyzing the linear model for determining stability characteristics, the transient effect of the perturbations was examined to help build confidence of the correctness of the simulations. The vehicle was set to steady state flight conditions using the steady state calculator described in Section 4.3. Then a Symmetric brake deflection pulse was applied for 10 seconds with a magnitude of $\Delta\delta_s = 0.1$ and time constant of 0.2 seconds. The input profile is shown in Figure 4.2.

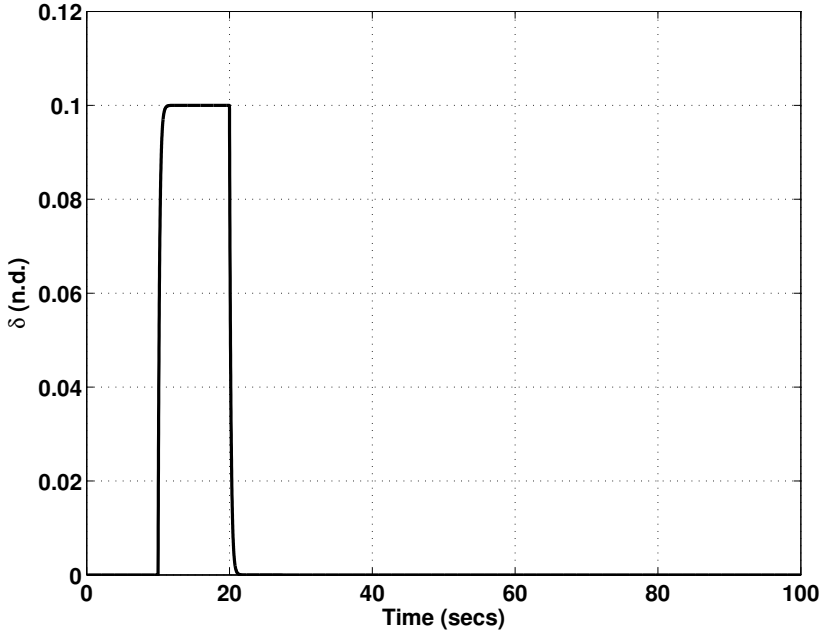

Figure 4.2. Brake input perturbation of $\Delta\delta = 0.1$

Figure 4.3 shows the longitudinal states θ_1 and θ_2 of both the linear and the nonlinear model. It can be observed that both the models almost correspond to each other. More importantly, as the pulse amplitude is decreased the error between the linear and nonlinear models decreases which is the proper trend.

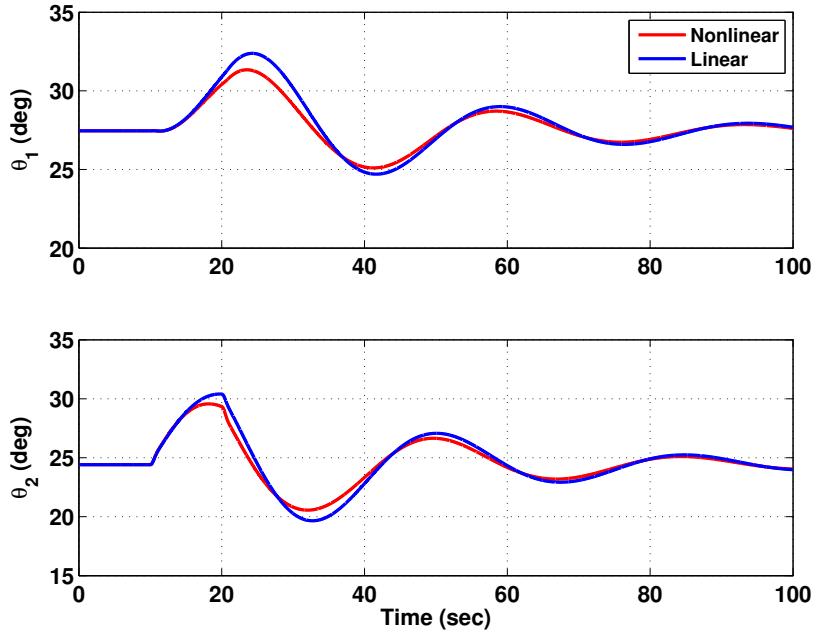

Figure 4.3. Linear and nonlinear model comparison of longitudinal states to a symmetric brake perturbation

Also, the lateral flight response was compared for asymmetric brake deflection perturbations, keeping the symmetric brakes to zero. The input profile of the asymmetric brakes is similar to the symmetric brakes as shown in Figure 4.2. The lateral states of both the models also correspond to each other well as shown in Figure 4.4.

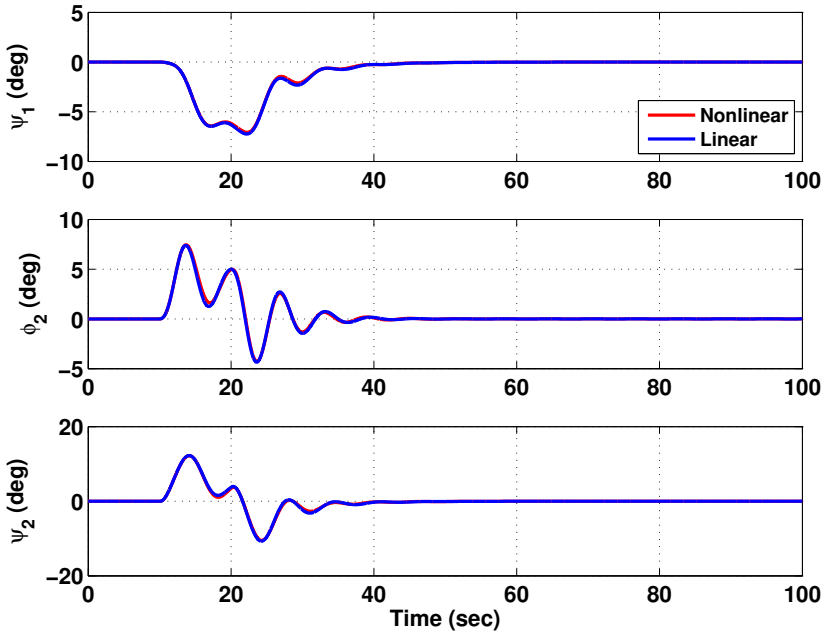

Figure 4.4. Linear and nonlinear model comparison of lateral states

4.5 Stability Boundaries

The main objective of the linear model is to analyze the stability of the parafoil-payload system about various operating points. The linear model developed in Section 4.2 is used to develop the stability boundaries. The rationale behind choosing the physical parameters and flight conditions which might affect the stability is based on the causes and conditions in which lockout may occur as described in Section 4.1. One of the main factors which can cause lockout is the cross wind. The wind input is modeled using three parameters:

1. The magnitude of the wind velocity vector v_w,
2. The azimuth angle or the angle it makes with the Inertial X direction in XY plane μ and
3. The elevation angle or the angle in the XZ plane η as shown in Figure 4.5

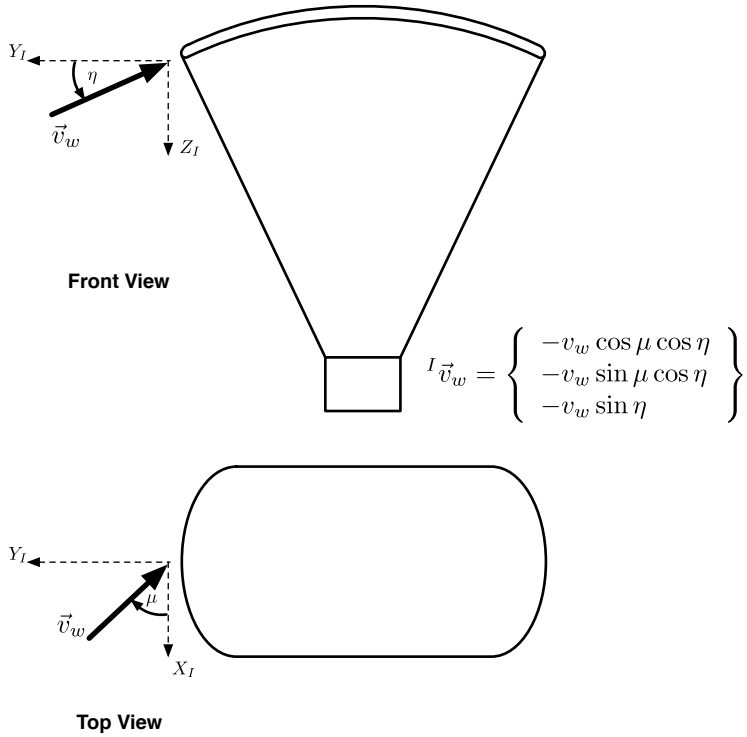

Figure 4.5. Wind Input modeled using three parameters: v_w,μ and η

The effect of the magnitude of the cross wind and the elevation angle, η, is analyzed for various steady flight conditions. The procedure adopted for stability analysis is as follows:

1. Set vehicle physical parameters and flight conditions to desired values. The significant physical parameters and flight conditions are listed below:

   (a) Mass of the payload, m_{pl}

   (b) Speed of the towing vehicle, v_s

   (c) The wind velocity magnitude, v_w

   (d) Azimuth angle of the wind velocity vector, μ

   (e) Elevation angle of the wind velocity vector, η

   (f) Symmetric brake deflection, δ_s

(g) Asymmetric brake deflection, δ_a

2. Calculate steady state values of the states shown in Equation 4.16 for each case of step #1.

3. Use these steady state values to evaluate the linear model, specifically the eigenvalues of the **A** matrix.

4. Eigenvalues of the **A** matrix are analyzed for any poles in right half plane.

4.5.1 Elevation Angle η

Figure 4.6 shows the stability plot of wind velocity versus the asymmetric brake input δ_a for various wind elevation angles, η. The physical parameters and flight conditions were:

1. Mass of the payload, $m_{pl} = 200$ lbs (90.7 Kg)

2. Symmetric brake deflection, $\delta_s = 0.2$

3. Ship velocity, $v_s = 13$ knots (6.68 m/s)

4. The wind velocity azimuth angle, $\mu = 90^\circ$

Figure 4.6 shows four stability contours for specific values of wind elevation angle η. These contours are the stability boundaries, exterior to which, the system is unstable. Due to the peculiar shape of this contour, it can be termed as stability envelope. The stability envelope depicts that for a particular value of η, there is a limit to the magnitude of wind velocity, beyond which the system is unstable. This magnitude decreases with increasing asymmetric brake deflection. Also, large values of the wind angle η, require smaller wind velocities to maintain stability. This effect can be explained by considering the wind vector's inertial

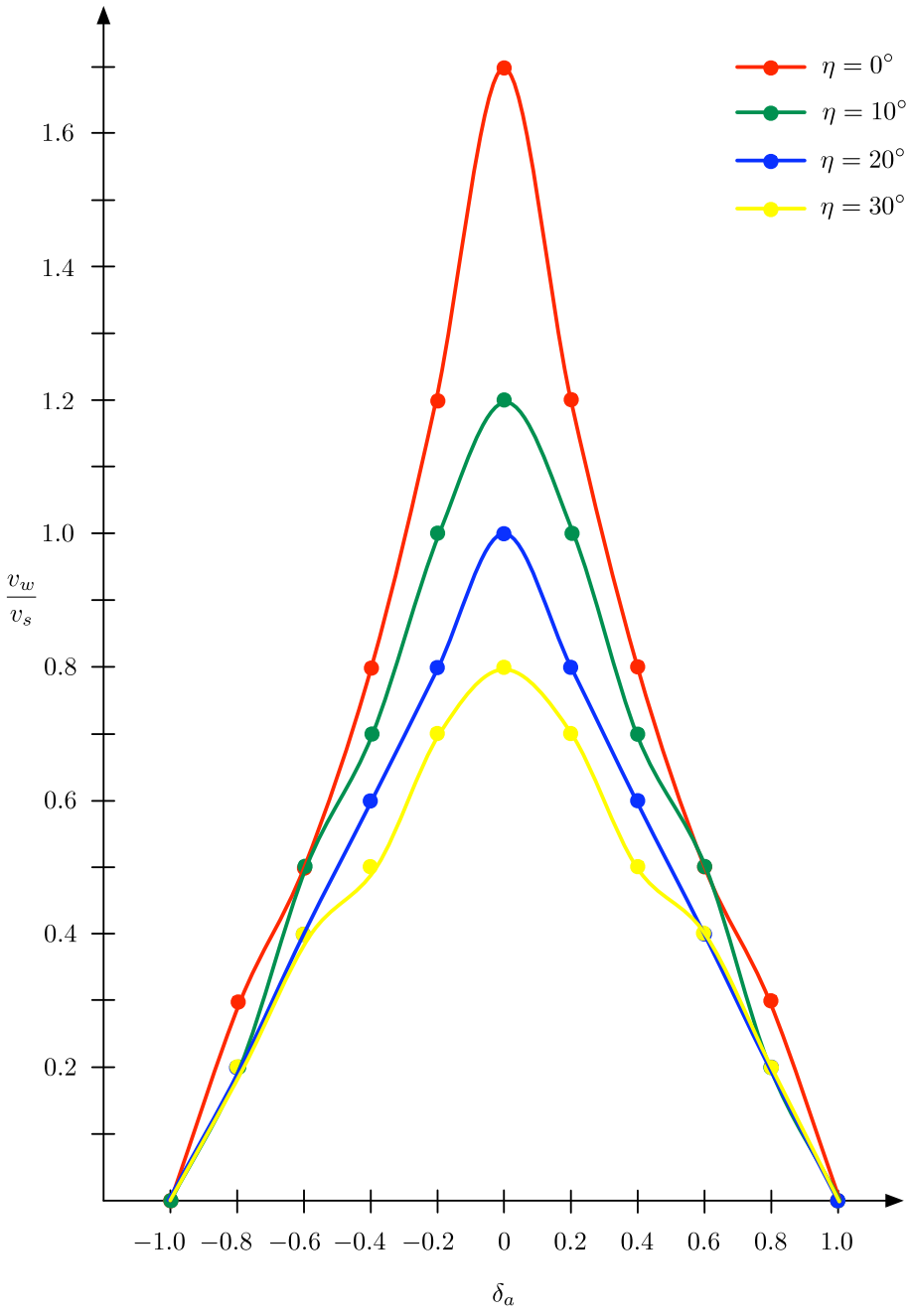

Figure 4.6. Stability boundaries for various η. Regions interior to each contour are stable, and unstable exterior to a contour.

Z component as shown in Equation 4.18. The Z component increases the relative velocity of the aerodynamic center of the parafoil canopy with respect to the wind $\vec{v}_{4/w}$ as shown in Equation 4.19. This increases the airfoil angle of attack and thus the aerodynamic forces and moments. In turn, the tow cable tension increases which promotes lockout.

$$ {}^{I}\vec{v}_{w} = \left\{ \begin{array}{l} -v_w \cos\mu \cos\eta \\ -v_w \sin\mu \cos\eta \\ -v_w \sin\eta \end{array} \right\} \tag{4.18} $$

$$ \begin{aligned} {}^{I}\vec{v}_{4/w} &= {}^{I}\vec{v}_{4} - {}^{I}\vec{v}_{w} \\ &= \left\{ \begin{array}{l} v_{4,x} \\ v_{4,y} \\ v_{4,z} \end{array} \right\} - \left\{ \begin{array}{l} -v_w \cos\mu \cos\eta \\ -v_w \sin\mu \cos\eta \\ -v_w \sin\eta \end{array} \right\} \end{aligned} \tag{4.19} $$

The steady state values of all the states are presented in Table 4.1 to Table 4.5. These values correspond to the data represented by the blue line of $\eta = 20^{\circ}$ in the Figure 4.6. The values marked with red color indicate that the steady state configuration is unstable. It can be observed from Table 4.1 that the steady state in-plane tow angle θ_{1_0} increases with increase in the magnitude of wind velocity for any given value of asymmetric brake deflection. This is consistent with the observed effect of increase in the altitude with the increase in relative wind speed. But as the altitude increases, for constant tow cable length, i.e. $\dot{L} = 0$, the tension in the cable increases, which favors lockout. This is the unstable flight regime marked with red color.

Table 4.2 shows the steady state pitch angle which is maximum for the zero wind velocity and decreases as the ratio of wind magnitude to the ship velocity increases.

Table 4.1
Steady state values of in-plane tow angle θ_{1_0} (deg) for $\eta = 20°$

1.0						71.7					
0.9					62.5	69.5	62.5				
0.8					61.1	66.7	61.1				
0.7				49.2	59	63.4	59	49.2			
0.6				48	56.1	59.5	56.1	48			
0.5			37.4	45.8	52.4	55	52.4	45.8	37.4		
0.4			35.8	42.9	48.2	50.1	48.2	42.9	35.8		
0.3		26.8	33.6	39.4	43.6	44.9	43.6	39.4	33.6	26.8	
0.2		25.2	31	35.8	39.2	40	39.2	35.8	31	25.2	
0.1	17.5	23.2	28.3	32.5	35.2	35.8	35.3	32.5	28.3	23.2	17.5
0	16.1	21.4	26	30	32	32.4	32	30	26	21.4	16.1
$\frac{v_w}{v_s} \Uparrow$ $\delta_a \Rightarrow$	-1	-0.8	-0.6	-0.4	-0.2	0.0	0.2	0.4	0.6	0.8	1.0

Table 4.2
Steady state values of pitch angle θ_{2_0} (deg) for $\eta = 20°$

1.0						10.8					
0.9					11.8	11.8	11.8				
0.8					13.2	13.1	13.2				
0.7				14.3	14.7	14.6	14.7	14.3			
0.6				16.1	16.4	16.2	16.4	16.1			
0.5			17.5	18.1	18.3	18.1	18.3	18.1	17.5		
0.4			19.8	20.2	20.3	20.1	20.3	20.2	19.8		
0.3		21.4	22.1	22.5	22.5	22.3	22.5	22.5	22.1	21.4	
0.2		23.9	24.5	24.8	24.8	24.6	24.8	24.8	24.5	23.9	
0.1	25.3	26.3	26.8	27.1	27.1	26.9	27.1	27.1	26.8	26.3	25.3
0	27.6	28.5	29.1	29.3	29.4	29.2	29.4	29.3	29.1	28.5	27.6
$\frac{v_w}{v_s} \Uparrow$ $\delta_a \Rightarrow$	-1	-0.8	-0.6	-0.4	-0.2	0.0	0.2	0.4	0.6	0.8	1.0

Table 4.3, 4.4 and 4.5 show the lateral steady state values. The increase in asymmetric brake deflection in the positive direction is analogous to a pilot pulling the right side parafoil brakes. This causes the canopy to yaw and roll in the positive direction. Also, the towed vehicle displaces in the positive inertial Y direction, which is indicated by the negative values of ψ_1. The lateral steady states corroborate the actual behavior of the parafoil canopy for asymmetric control inputs.

Table 4.3

Steady state values of off-plane tow angle ψ_{1_0} (deg) for $\eta = 20°$

1.0						43.2					
0.9					79.8	40.2	0.6				
0.8					71.7	37	2.1				
0.7				80.9	63.5	33.3	3.1	-14.2			
0.6				72.2	55.4	29.4	3.5	-13.4			
0.5			73.4	63.2	47.4	25.2	2.9	-12.9	-23		
0.4			64.5	54.3	39.7	20.6	1.5	-13.1	22.6		
0.3		62.8	55.6	45.7	32.3	15.7	-0.78	-14.2	-24.1	-31.3	
0.2		54.3	47	37.4	25.2	10.6	-3.9	-16.1	-25.7	-33	
0.1	51.9	46.2	39	29.8	18.4	5.4	-7.7	-19	-28.2	-35.5	-41.1
0	44.6	38.8	31.6	22.7	12.1	0	-12.1	-22.7	-31.6	-38.8	-44.6
$\frac{v_w}{v_s} \Uparrow$ $\delta_a \Rightarrow$	-1	-0.8	-0.6	-0.4	-0.2	0.0	0.2	0.4	0.6	0.8	1.0

Table 4.4

Steady state values of roll angle ϕ_{2_0} (deg) for $\eta = 20°$

1.0						0					
0.9					-12	0	12				
0.8					-10.8	0	10.8				
0.7				-19.6	-9.7	0	9.7	19.6			
0.6				-17.7	-8.8	0	8.8	17.7			
0.5			-24.5	-16.2	-8.1	0	8.1	16.2	24.5		
0.4			-22.6	-15	-7.5	0	7.5	15	22.6		
0.3		-28.6	-21.2	-14.1	-7	0	7	14.1	21.2	28.6	
0.2		-27.4	-20.3	-13.5	-6.7	0	6.7	13.5	20.3	27.4	
0.1	-33.9	-26.8	-19.9	-13.2	-6.6	0	6.6	13.2	19.9	26.8	33.9
0	-34	-26.9	-20	-13.3	-6.6	0	6.6	13.3	20	26.9	34
$\frac{v_w}{v_s} \Uparrow$ $\delta_a \Rightarrow$	-1	-0.8	-0.6	-0.4	-0.2	0.0	0.2	0.4	0.6	0.8	1.0

Table 4.5
Steady state values of yaw angle ψ_{2_0} (deg) for $\eta = 20°$

1.0						43.2					
0.9					35.8	40.2	44.6				
0.8					33	36.9	40.9				
0.7				26.2	29.8	33.3	36.9	40.5			
0.6				22.9	26.2	29.4	32.6	35.9			
0.5			16.1	19.2	22.2	25.2	28.1	31.1	34.3		
0.4			12.1	15.1	17.9	20.6	23.3	26.2	29.1		
0.3		4.9	7.7	10.5	13.6	15.7	18.3	21.0	23.8	26.6	
0.2		0.1	2.9	5.5	8.1	10.6	13.2	15.8	18.4	21.2	
0.1	-7.9	-5.1	-2.4	0.3	2.9	5.4	7.9	10.5	13.1	15.8	18.7
0	-13.5	-10.7	-7.9	-5.2	-2.6	0	2.6	5.2	7.9	10.7	13.5
$\frac{v_w}{v_s} \Uparrow$ $\delta_a \Rightarrow$	-1	-0.8	-0.6	-0.4	-0.2	0.0	0.2	0.4	0.6	0.8	1.0

Additional steady state values for $\eta = 0°$, $10°$ and $30°$ are presented in Appendix C.

Consider the case of $\delta_a = 0$ and $\frac{v_w}{v_s} = 0.4$ for the steady state configuration in Table 4.1 to Table 4.5 marked in blue. For this case the **A** matrix and **B** matrix is shown in Equation 4.20. The eigenvalues of the **A** matrix are all stable: $-3.0 \pm 2.01i$, $-0.44 \pm 1.46i$, $-0.197 \pm 0.271i$, $-0.143 \pm 0.737i$, -17.6 and -0.25.

$$\underline{\dot{\Delta x}} = \mathbf{A}\underline{\Delta x} + \mathbf{B}\underline{\Delta u} \tag{4.20}$$

where,

$$A = \begin{bmatrix} 0 & 0 & 0 & 0 & 0 & 1 & 0 & 0 & 0 & 0 \\ 0 & 0 & 0 & 0 & 0 & 0 & 1 & 0 & 0 & 0 \\ 0 & 0 & 0 & 0 & 0 & 0 & 0 & 1 & 0 & 0 \\ 0 & 0 & 0 & 0 & 0 & 0 & 0 & 0 & 1 & 0 \\ 0 & 0 & 0 & 0 & 0 & 0 & 0 & 0 & 0 & 1 \\ -0.28 & 0 & 0 & -0.43 & 0 & 1.27 & 0 & 0 & 0 & \\ 0 & -0.29 & -1.19 & 0 & 1.32 & 0 & 4.61 & -1.49 & 0 & 0.57 \\ 0 & -0.36 & -8.56 & 0 & 17.67 & 0 & 77.76 & -24.38 & 0 & 8.39 \\ -1.31 & 0 & 0 & -7.97 & 0 & 35.53 & 0 & 0 & -8.27 & 0 \\ 0 & 1.07 & -0.43 & 0 & 3.23 & 0 & 19.33 & -5.37 & 0 & 0.75 \end{bmatrix}$$

and,

$$B = \begin{bmatrix} 0 & 0 \\ 0 & 0 \\ 0 & 0 \\ 0 & 0 \\ 0 & 0 \\ 0.17 & 0 \\ 0 & -0.05 \\ 0 & 0.82 \\ 3.62 & 0 \\ 0 & 1.43 \end{bmatrix}$$

4.5.2 Symmetric Brake Deflection δ_s

The stability boundaries with respect to various symmetric brake inputs are plotted in Figure 4.7. The dotted lines represent the practical limits of the asymmetric brakes for a given

symmetric brake setting. It can be seen that the stability envelope widens with increasing symmetric brake inputs, but at the same time the range of asymmetric brake decreases. With $\delta_s = 0$, the system is more sensitive to δ_a as compared to $\delta_s = 0.2$ or $\delta_s = 0.4$. So to optimize between the sensitivity and range of asymmetric brake inputs, a compromise value of the symmetric brake inputs must be used for stable and controllable flight.

4.5.3 Effect of Tow Point Location

Since the main difference between a towed paraglider and a free flying paraglider is the tow cable force and the moments created by this force about the CG of the system, the tow point location is an important factor to be considered for stability analysis. In Figure 4.8 X-axis represents the z component of the relative vector between the tow point and the CG of the system $r_{3/2,z}$ in meters. On the y axis the ratio of the magnitude of the wind velocity to the ship velocity is shown. The positive values of $r_{3/2,z}$ represent that the tow point is located below the CG of the system. It can be clearly seen that that as the tow point moves below CG, the system can sustain larger magnitudes of wind gusts. Hence the tow point should be located below the CG of the system for increasing stability in crosswind conditions. Due to the limitation of the standard optimization routines in Matlab to calculate exact steady state of the nonlinear dynamic system, a curve is fit to the steady state values as shown in the Figure 4.8.

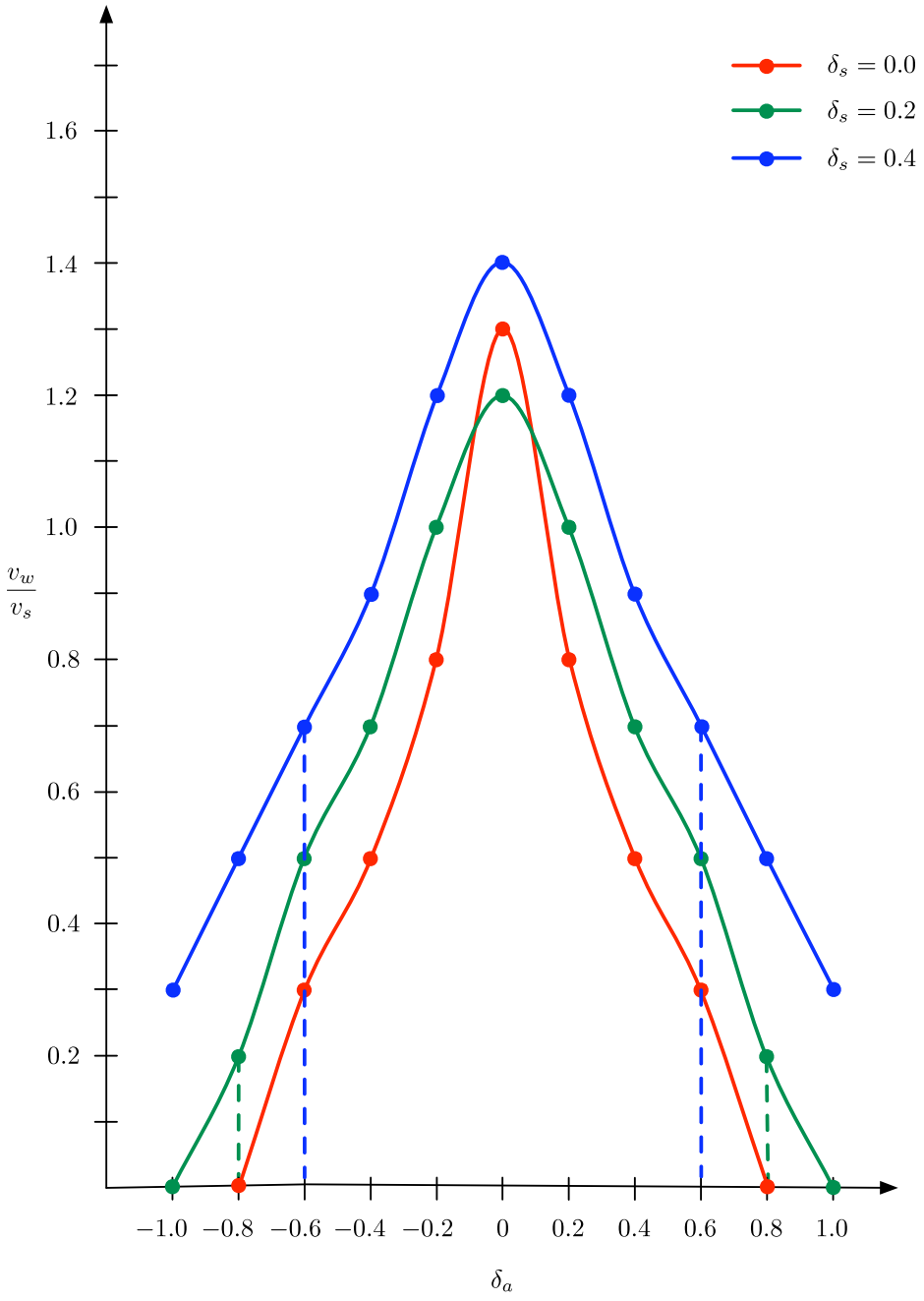

Figure 4.7. Stability boundaries for various δ_s

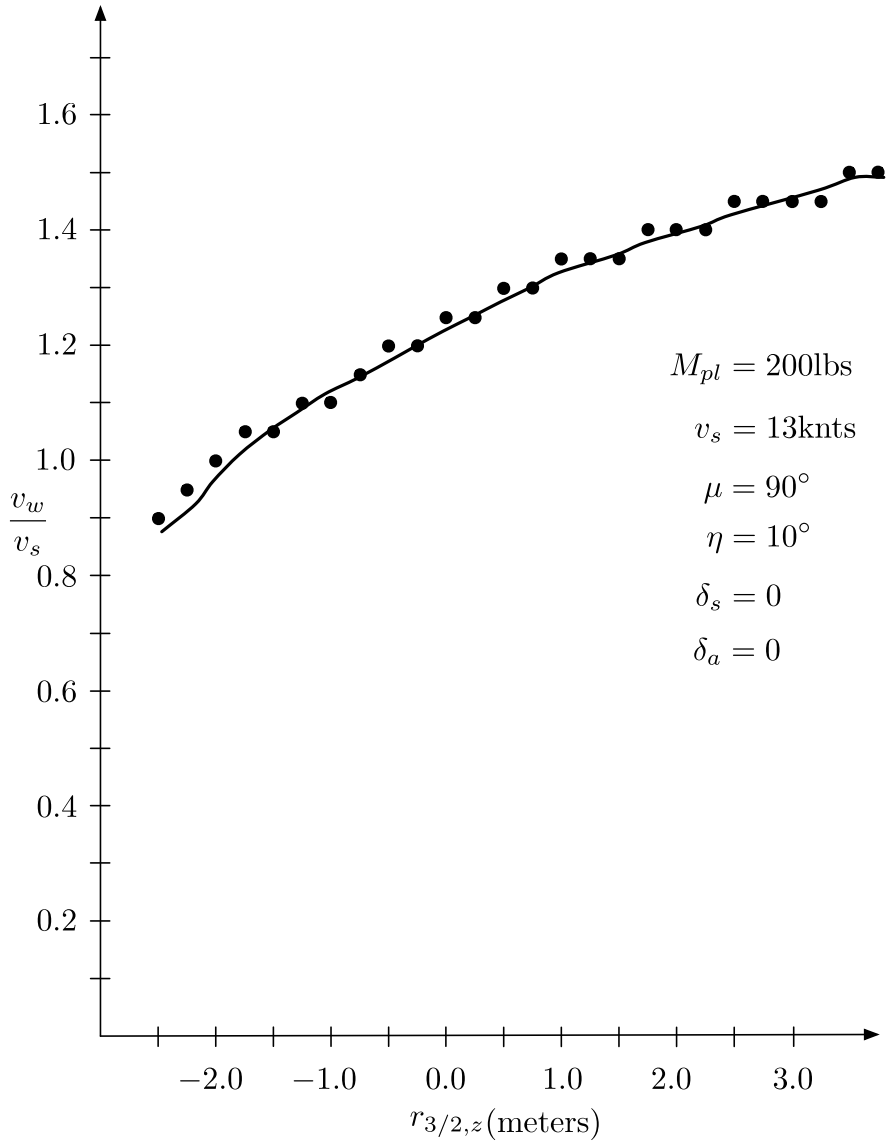

Figure 4.8. Stability boundary showing the effect of tow point location

4.6 Summary

As discussed earlier, the main problem with towed paragliders is lockout. This unstable flight condition has been modeled using the linear model and anaylzing the stability for various flight conditions and input parameters. The stability boundaries indicate that there is a limitation on the amount of control input that can be used to counter the cross wind disturbances. This is consistent with pilot's experiences of lockout sensitivity to crosswinds. Also, to tow up the system as fast as possible, without loosing the stability, a closed loop control strategy is essential to maintain stability due to high cable forces. Stability was also shown to be sensitive to tow cable force which confirms the practical understanding of lockout. This chapter provided an insight into which factors are important while considering the problem of lockout. The next chapter will focus on the control strategy development based on the observations made in this chapter. For stability control, the only two inputs are symmetric and asymmetric brake setting. The sensitivity and range of these control inputs will play an important role in designing the control strategy.

5. Control System Design

This chapter is organized as follows. Considering the main goals of SLADS as outlined in Section 1.3, and the stability analysis results of the towed flight system in Chapter 4, significant control objectives are outlined in Section 5.1. In order to develop a control strategy based on the linear model, the controllability and observability of the system is assessed in Section 5.2. A tow up control system using the longitudinal linear model is developed in Section 5.3. Section 5.4 provides a control strategy design to expand the stable flight regimes, in the case of lateral disturbance. The chapter concludes with observations and conclusions, followed by a proposed future work in the area of control system development for towed parafoil-payload systems in Section 5.5.

5.1 Control Objectives

As discussed in Chapter 1, one of the main objectives of the Ship Launched Aerial Delivery System (SLADS) is that the system be able to precisely deliver cargo from ship to shore quickly. To accomplish this objective, the parafoil-payload system has to be towed up, as fast as possible since the main objective during the free flight phase is the precision of the delivery. Moreover, it is essential to keep the towed system in line with the towing vehicle to maintain stability as discussed in Chapter 4. Since the focus of this research is

on the towed phase, the main objectives of the control system are:

1. Tow up the system as fast as possible
2. Maintain stability

With these two goals, the linear model developed in Chapter 4 is used to develop the control strategy in MATLAB/Simulink environment. These control objectives are first put forth in mathematical terms in relation to the model developed and then investigated using simulation.

1. To maximize the rate of ascent of the parafoil-payload system, defined by, $\dot{p}_{2/1,z}$ using two longitudinal control inputs:
   (a) Symmetric brake deflection, δ_s
   (b) Tow cable payout rate, $\dot{L}$
2. To keep the eigenvalues of the closed loop system in the left half plane using asymmetric brake deflection δ_a, to counter the effect of lateral wind disturbance defined by three parameters:
   (a) Wind velocity magnitude, v_w
   (b) Azimuth angle, μ
   (c) Elevation angle, η

5.2 Controllability And Observability

The linear model developed in Chapter 4 is used to develop the control strategies. Before designing a control strategy, it is essential to analyze whether the system states can be

controlled using the available set of inputs. The linear model, using perturbed states and inputs, can be described as shown in the Equation 5.1.

$$\underline{\dot{\Delta x}} = \mathbf{A}\underline{\Delta x} + \mathbf{B}\underline{\Delta u} \tag{5.1}$$

where, the linearized state vector $\underline{\Delta x}$ is defined as described in Chapter 4.

$$\underline{\Delta x} = \begin{bmatrix} \Delta\theta_1 & \Delta\psi_1 & \Delta\phi_2 & \Delta\theta_2 & \Delta\psi_2 & \Delta\dot{\theta}_1 & \Delta\dot{\psi}_1 & \Delta\dot{\phi}_2 & \Delta\dot{\theta}_2 & \Delta\dot{\psi}_2 \end{bmatrix}^T \tag{5.2}$$

The general **A** matrix has the form as shown in Equation 5.3.

$$\mathbf{A} = \begin{bmatrix} 0 & 0 & 0 & 0 & 0 & 1 & 0 & 0 & 0 & 0 \\ 0 & 0 & 0 & 0 & 0 & 0 & 1 & 0 & 0 & 0 \\ 0 & 0 & 0 & 0 & 0 & 0 & 0 & 1 & 0 & 0 \\ 0 & 0 & 0 & 0 & 0 & 0 & 0 & 0 & 1 & 0 \\ 0 & 0 & 0 & 0 & 0 & 0 & 0 & 0 & 0 & 1 \\ A_{61} & A_{62} & A_{63} & A_{64} & A_{65} & A_{66} & A_{67} & A_{68} & A_{69} & A_{610} \\ A_{71} & A_{72} & A_{73} & A_{74} & A_{75} & A_{76} & A_{77} & A_{78} & A_{79} & A_{710} \\ A_{81} & A_{82} & A_{83} & A_{84} & A_{85} & A_{86} & A_{87} & A_{88} & A_{89} & A_{810} \\ A_{91} & A_{92} & A_{93} & A_{94} & A_{95} & A_{96} & A_{97} & A_{98} & A_{99} & A_{910} \\ A_{101} & A_{102} & A_{103} & A_{104} & A_{105} & A_{106} & A_{107} & A_{108} & A_{109} & A_{1010} \end{bmatrix} \tag{5.3}$$

The **B** matrix with respect to the perturbations of input vector $\Delta\underline{u}$,

$$\underline{\Delta u} = \left\{ \begin{array}{c} \Delta\delta_s \\ \Delta\delta_a \end{array} \right\} \tag{5.4}$$

is,

$$\mathbf{B} = \left[\begin{array}{cc} 0 & 0 \\ 0 & 0 \\ 0 & 0 \\ 0 & 0 \\ 0 & 0 \\ B_{61} & B_{62} \\ B_{71} & B_{72} \\ B_{81} & B_{82} \\ B_{91} & B_{92} \\ B_{101} & B_{102} \end{array} \right] \tag{5.5}$$

5.2.1 Definition

If a system is controllable then a control input $\underline{\Delta u}$ exists that can move the system from an initial state $\underline{\Delta x}_0$ to any final state $\underline{\Delta x}$. A n dimensional p input state equation or the pair (A, B) is said to be controllable, if the $n \times np$ controllability matrix

$$\mathcal{C} = \left[\begin{array}{cccccc} B & AB & A^2B & \cdots & A^{n-1}B \end{array} \right] \tag{5.6}$$

has rank n (full row rank) (32).

Observability is a dual property to controllability. If a system is observable, then all

the states can be computed at time t_1 by knowing the input $\underline{\Delta u}(t)$ for all $t \leq t_1$ and the measurements $\underline{\Delta y}(t)$ for all $t \leq t_1$. A n dimensional q output state equation or the pair (A, C) is said to be controllable, if the $nq \times n$ observability matrix

$$\mathcal{O} = \begin{bmatrix} C \\ CA \\ . \\ . \\ . \\ CA^{n-1} \end{bmatrix} \tag{5.7}$$

has rank n (full column rank) (32).

The **A**,**B** and **C** matrices are expressed numerically for specific representative cases of steady states and the controllability and observability are assessed for those cases. The states of the system are the five angles and their derivatives. All of these states can be measured in the experimental setup. Depending on the control strategy objective, the output matrix **C** will be chosen.

5.2.2 Case I

Consider a steady state flight condition where the ship is moving with the speed of 13 knots, towing a 500 square feet paraglider with a payload of 200 lbs. The symmetric brakes are set at $\delta_s = 0.2$ and the asymmetric brakes are set at $\delta_a = 0.2$. The cross wind velocity magnitude is 0.5 times the velocity of the ship. The cross wind is acting on the parafoil aerodynamic center at an azimuth angle $\mu = 90^\circ$ and elevation angle $\eta = 20^\circ$. The steady state values of the states are given in Table 4.1 to 4.5. The steady state vector is summarized

in Equation 5.8.

$$\underline{x}_0 = \begin{bmatrix} 52.4^\circ & 2.9^\circ & 8.1^\circ & 18.3^\circ & 28.1^\circ & 0 & 0 & 0 & 0 & 0 \end{bmatrix}^T \tag{5.8}$$

The steady state input vector is shown in Equation 5.9.

$$\underline{u}_0 = \begin{Bmatrix} 0.2 \\ 0.2 \end{Bmatrix} \tag{5.9}$$

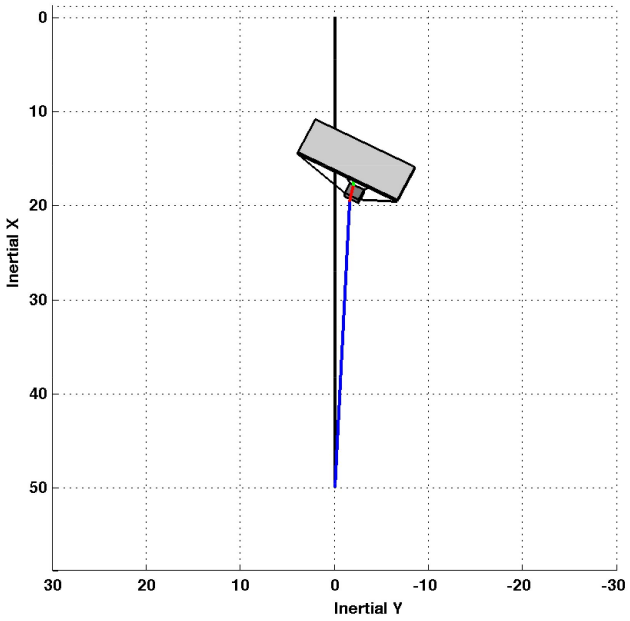

Figure 5.1. Top view of the steady state configuration in case I

The top view of the steady state flight configuration is shown in Figure 5.1. This steady state configuration was found to be stable with all the eigenvalues of the system in the left half plane. Equation 5.10 gives the **A** and **B** matrices of linear model. Note that the inputs to the system consist of the symmetric and asymmetric brake perturbations. The

controllability matrix was evaluated using Maple and the rank of the controllability matrix was found to be 10, which is equal to the full row rank. Hence the system is completely controllable in this configuration. Also, the observability matrix associated with complete state output has rank 10 and hence the system is observable too.

$$\underline{\dot{\Delta x}} = \begin{bmatrix} 0.0 & 0.0 & 0.0 & 0.0 & 0.0 & 1.0 & 0.0 & 0.0 & 0.0 & 0.0 \\ 0.0 & 0.0 & 0.0 & 0.0 & 0.0 & 0.0 & 1.0 & 0.0 & 0.0 & 0.0 \\ 0.0 & 0.0 & 0.0 & 0.0 & 0.0 & 0.0 & 0.0 & 1.0 & 0.0 & 0.0 \\ 0.0 & 0.0 & 0.0 & 0.0 & 0.0 & 0.0 & 0.0 & 0.0 & 1.0 & 0.0 \\ 0.0 & 0.0 & 0.0 & 0.0 & 0.0 & 0.0 & 0.0 & 0.0 & 0.0 & 1.0 \\ -0.3 & -0.001 & -0.3 & -0.5 & 0.3 & 2.0 & 0.6 & -0.4 & -0.5 & 0.06 \\ -0.003 & -0.3 & -1.0 & 0.4 & 1.0 & 2.0 & 4.0 & -1.0 & 0.2 & 0.5 \\ -0.3 & -0.4 & -9.0 & -3.0 & 20.0 & 50.0 & 70.0 & -20.0 & -1.0 & 8.0 \\ -1.0 & 0.2 & 0.1 & -9.0 & -2.0 & 30.0 & -8.0 & 0.8 & -8.0 & -1.0 \\ 0.5 & 1.0 & -0.3 & -3.0 & 3.0 & 20.0 & 20.0 & -5.0 & -1.0 & 0.4 \end{bmatrix} \underline{\Delta x}$$

$$+ \begin{bmatrix} 0 & 0 \\ 0 & 0 \\ 0 & 0 \\ 0 & 0 \\ 0 & 0 \\ 0.18 & -0.01 \\ -0.08 & -0.05 \\ 0.2 & 0.83 \\ 3.92 & -0.19 \\ 0.44 & 1.5 \end{bmatrix} \underline{\Delta u} \qquad (5.10)$$

5.2.3 Case II:

The flight conditions and parameters are chosen similar to Case I, except that all the brake deflections are set to zero, i.e.

$$U_0 = \begin{Bmatrix} 0 \\ 0 \end{Bmatrix} \tag{5.11}$$

The steady state vector is shown in Equation 5.12. Note that the roll angle is zero, since the asymmetric brakes are set to zero. The steady state configuration is shown in Figure 5.2.

$$X_0 = \begin{bmatrix} 56.02^\circ & 25.17^\circ & 0.0^\circ & 13.17^\circ & 25.17^\circ & 0 & 0 & 0 & 0 & 0 \end{bmatrix}^T \tag{5.12}$$

The linear system is represented in Equation 5.13. Note that the longitudinal and the lateral

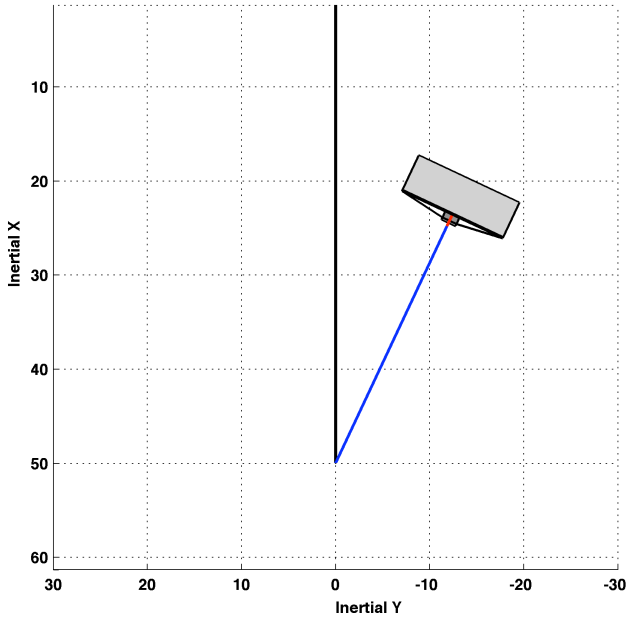

Figure 5.2. Top view of the steady state configuration in case II

states can be decoupled in this steady state configuration as shown in the equation 5.13 by

blue and green colors respectively.

$$
\underline{\dot{\Delta x}} = \begin{bmatrix}
0.0 & 0.0 & 0.0 & 0.0 & 0.0 & 1.0 & 0.0 & 0.0 & 0.0 & 0.0 \\
0.0 & 0.0 & 0.0 & 0.0 & 0.0 & 0.0 & 1.0 & 0.0 & 0.0 & 0.0 \\
0.0 & 0.0 & 0.0 & 0.0 & 0.0 & 0.0 & 0.0 & 1.0 & 0.0 & 0.0 \\
0.0 & 0.0 & 0.0 & 0.0 & 0.0 & 0.0 & 0.0 & 0.0 & 1.0 & 0.0 \\
0.0 & 0.0 & 0.0 & 0.0 & 0.0 & 0.0 & 0.0 & 0.0 & 0.0 & 1.0 \\
-0.19 & 0.0 & 0.0 & -0.33 & 0.0 & 1.1 & 0.0 & 0.0 & -0.52 & 0 \\
0.0 & -0.20 & -1.1 & 0.0 & 1.3 & 0.0 & 4.0 & -1.5 & 0.0 & 0.41 \\
0.0 & -0.29 & -5.6 & 0.0 & 14.0 & 0.0 & 51.0 & -18.0 & 0.0 & 4.3 \\
-0.90 & 0.0 & 0.0 & -7.2 & 0.0 & 31.0 & 0.0 & 0.0 & -7.4 & 0 \\
0.0 & 0.62 & 0.68 & 0.0 & 0.34 & 0.0 & 3.6 & -0.70.0 & 0.0 & -1.0
\end{bmatrix}
\begin{Bmatrix}
\Delta\theta_1 \\ \Delta\psi_1 \\ \Delta\phi_2 \\ \Delta\theta_2 \\ \Delta\psi_2 \\ \Delta\dot{\theta}_1 \\ \Delta\dot{\psi}_1 \\ \Delta\dot{\phi}_2 \\ \Delta\dot{\theta}_2 \\ \Delta\dot{\psi}_2
\end{Bmatrix}
+ \begin{bmatrix}
0.0 & 0.0 \\ 0.0 & 0.0 \\ 0.0 & 0.0 \\ 0.0 & 0.0 \\ 0.0 & 0.0 \\ 0.14 & 0.0 \\ 0.0 & -0.059 \\ 0.0 & 0.69 \\ 2.8 & 0 \\ 0.0 & 1.5
\end{bmatrix}
\begin{Bmatrix}
\Delta\delta_s \\ \Delta\delta_a
\end{Bmatrix} \tag{5.13}
$$

The controllability matrix developed for this configuration also has rank 10, and hence the system is controllable in the vicinity of this steady state flight. Also the observability matrix for a complete state output has the rank 10 and the system is thus observable.

5.2.4 Case III:

A unstable steady state case will be presented here for assessing the system's controllability and observability. Refering to Table 4.1 to Table 4.5, the steady state for asymmetric brake deflection of $\delta_a = 0.2$ and $\frac{v_w}{v_s} = 0.8$, the system is unstable. The remaining physical parameters and flight conditions are the same as in Case I. The steady state vector is shown in Equation 5.14. The steady state configuration is shown in Figure 5.3. Note the large yaw angle of the system in this configuration, leading to instability.

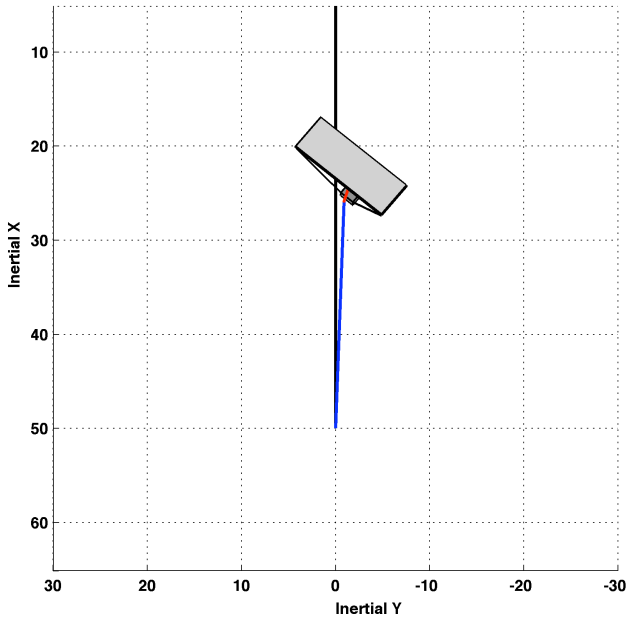

Figure 5.3. Top view of the steady state configuration in case III

$$X_0 = \begin{bmatrix} 61.1^\circ & 2.1^\circ & 10.8^\circ & 13.2^\circ & 40.9^\circ & 0 & 0 & 0 & 0 & 0 \end{bmatrix}^T \tag{5.14}$$

The linear system is represented in Equation 5.15.

$$\underline{\dot{\Delta x}} = \begin{bmatrix} 0.0 & 0.0 & 0.0 & 0.0 & 0.0 & 1.0 & 0.0 & 0.0 & 0.0 & 0.0 \\ 0.0 & 0.0 & 0.0 & 0.0 & 0.0 & 0.0 & 1.0 & 0.0 & 0.0 & 0.0 \\ 0.0 & 0.0 & 0.0 & 0.0 & 0.0 & 0.0 & 0.0 & 1.0 & 0.0 & 0.0 \\ 0.0 & 0.0 & 0.0 & 0.0 & 0.0 & 0.0 & 0.0 & 0.0 & 1.0 & 0.0 \\ 0.0 & 0.0 & 0.0 & 0.0 & 0.0 & 0.0 & 0.0 & 0.0 & 0.0 & 1.0 \\ -0.47 & -0.0028 & -0.62 & -0.65 & 0.50 & 2.8 & 0.81 & -0.64 & -0.47 & 0.087 \\ -0.012 & -0.47 & -1.7 & 0.93 & 1.9 & 4.1 & 3.4 & -1.8 & 0.45 & 0.56 \\ -0.83 & -0.45 & -11.0 & -4.8 & 22.0 & 82.0 & 48.0 & -26.0 & -1.2 & 5.9 \\ -2.0 & 0.43 & -0.064 & -11.0 & -2.9 & 25.0 & -8.7 & 0.84 & -8.7 & -1.6 \\ 1.2 & 1.1 & 0.47 & -4.4 & 2.8 & 25.0 & 8.4 & -4.7 & -1.9 & -0.58 \end{bmatrix} \underline{\Delta x}$$
$$+ \begin{bmatrix} 0.0 & 0.0 \\ 0.0 & 0.0 \\ 0.0 & 0.0 \\ 0.0 & 0.0 \\ 0.0 & 0.0 \\ 0.18 & -0.026 \\ -0.19 & -0.070 \\ 0.25 & 0.90 \\ 4.7 & -0.35 \\ 0.73 & 1.9 \end{bmatrix} \underline{\Delta u} \tag{5.15}$$

In this case also, the system is both controllable and observable, as evaluated in Maple. Since the **A**, **B** and **C** matrices have forms similar to one of the representative cases mentioned above, it appears that the system is controllable and observable in the vicinity of all the steady state configurations under study.

5.3 Tow Up Control Strategy

One of the main objectives of SLADS is to tow up the parafoil-payload system to the desired altitude as fast as possible. Before developing any tow up control strategy, the various significant parameters affecting the tow up were analyzed by simulation. A general schematic of the open loop plant is shown in Figure 5.4.

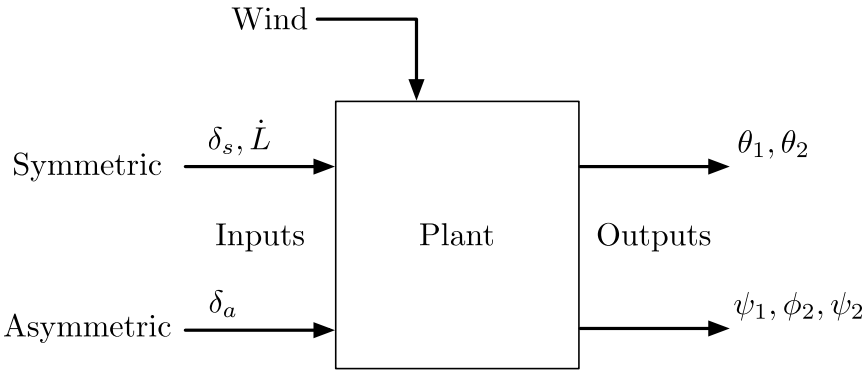

Figure 5.4. Open Loop Plant Schematic

The symmetric brake inputs δ_s and the tow cable payout rate $\dot{L}$, affect only the symmetric states θ_1 and θ_2, assuming no cross winds. Also, it has been observed that in steady state flight condition with zero asymmetric brake deflection $\delta_a = 0$, the system can be decoupled into longitudinal and lateral states as seen in subsection 5.2.3. Effect of δ_s and $\dot{L}$ on the rate of ascent of the parafoil-payload system is analyzed in longitudinal flight mode. Figure 5.8 shows the effect of symmetric brake deflection on the ascent rate. It can be observed that

the ascent rate is the minimum for $\delta_s = 0$, with significant loss of altitude in the transient phase. Also, the ascent rate increases with increasing symmetric brake deflection upto a certain limit, in this case $\delta_s = 0.4$. Beyond this, the ascent rate decreases with increase in the symmetric brake deflection. Hence it is essential to keep the symmetric deflection at some non zero value but below this transition point.

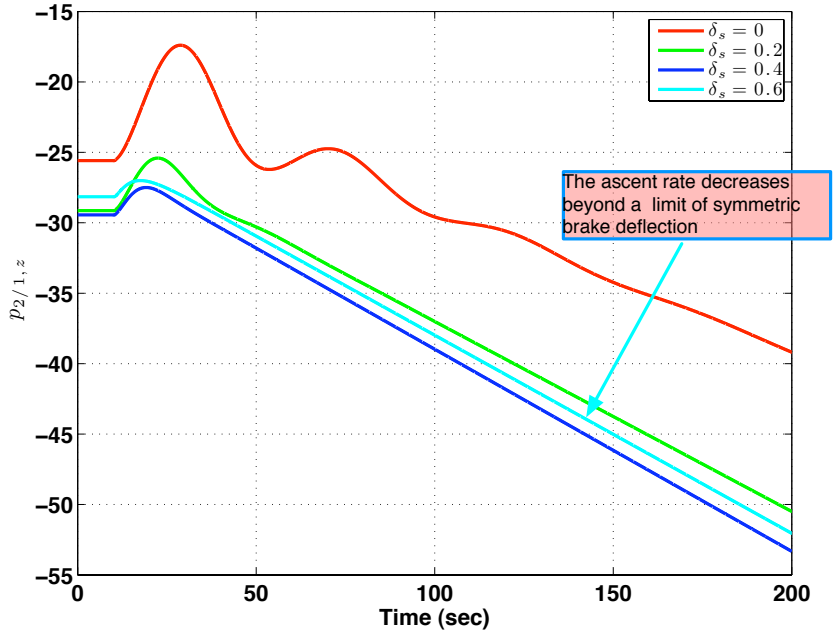

Figure 5.5. Effect of symmetric brake deflection on ascent rate. Cable payout rate is 0.3 meters/sec starting at 10 sec, negative $p_{2/1,z}$ is an upward motion.

A similar study was conducted to analyze the net effect of cable payout rates and the symmetric brake deflection on the ascent rate. The ascent rate data is shown in Table 5.1. As expected, the ascent rate increases as the cable payout rate is increased. However, the tow cable payout rate should be increased gradually to decrease the loss of altitude in the transient phase.

One more important factor from the perspective of optimal tow up is the tension in the cable. Data showing the tow cable tension for various symmetric brake deflection and

Table 5.1
Ascent rate $\dot{p}_{2/1,z}$ in meters/second for various cable payout rates $\dot{L}$ in meters/second and symmetric brake deflections δ_s

0.6	0.0505	0.1407	0.2146	0.271	0.3086
0.4	0.0524	0.1435	0.2149	0.2646	0.2905
0.2	0.0508	0.1349	0.1933	0.223	0.2208
0.0	0.0414	0.0992	0.1397	0.1045	0.0433
$\delta_s \Uparrow$, $\dot{L} \Rightarrow$	0.1	0.3	0.5	0.7	0.9

cable payout rate combination is presented in Table 5.2. The tension should be kept as low as possible to avoid lockout instability. It can be seen that with the increasing symmetric brake deflection the tension in the tow cable increases. So there is a limit to which the symmetric brakes can be increased, such that the parafoil payload system ascends as fast as possible without compromising stability.

Table 5.2
Tow cable tension in Newtons for various cable payout rates $\dot{L}$ in meters/second and symmetric brake deflections δ_s

0.6	2496	2375	2251	2125	1997
0.4	1799	1713	1625	1533	1439
0.2	1236	1176	1113	1047	976
0.0	817	774	726	676	621
$\delta_s \Uparrow$, $\dot{L} \Rightarrow$	0.1	0.3	0.5	0.7	0.9

5.3.1 Controller for Ascent Rate

After analyzing the factors affecting ascent rate, it was concluded that the controller for the ascent rate can be developed in the longitudinal flight mode. The schematic of the feedback control law is shown in the Figure 5.6.

The input to the system is the tow cable payout rate at the ship end. Two types of control

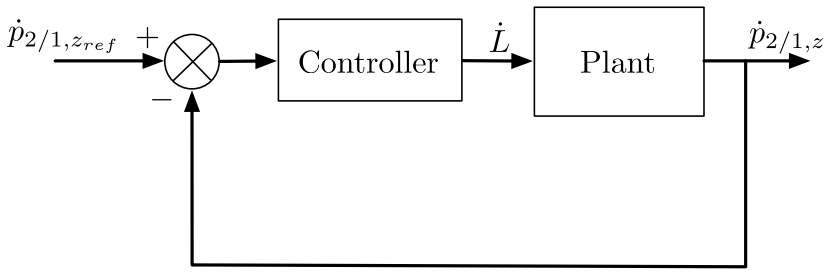

Figure 5.6. Schematic of tow up ascent rate controller for parafoil-payload system

systems are developed and compared. A simple proportional controller is designed to tow up the parafoil-payload system at a particular ascent rate. The proportional control law is shown in the Equation 5.16

$$\dot{L} = K_p \left(\dot{p}_{2/1,z_{ref}} - \dot{p}_{2/1,z} \right) \tag{5.16}$$

Similarly, the proportional-derivative (PD) controller is represented as shown in Equation 5.17.

$$\dot{L} = K_p \left(\dot{p}_{2/1,z_{ref}} - \dot{p}_{2/1,z} \right) + K_d \frac{d}{dt} \left(\dot{p}_{2/1,z_{ref}} - \dot{p}_{2/1,z} \right) \tag{5.17}$$

The ascent rate obtained with these two control systems is shown in Figure 5.7. The symmetric brakes are held constant at $\delta_s = 0.2$. The system is allowed to fly in longitudinal steady state flight condition and the control system is set 'on' at 10 seconds after starting the simulation time. Though both the controllers reach the same steady state ascent rate, the proportional controller has much less damping effect as compared to the proportional derivative controller. It should be noted that the steady state ascent rate is the maximum ascent rate possible with this configuration of symmetric brakes as shown in Table 5.1. The settling time with the PD controller is much better, at about 133 seconds, than the

proportional control law, for which it is more than 300 seconds.

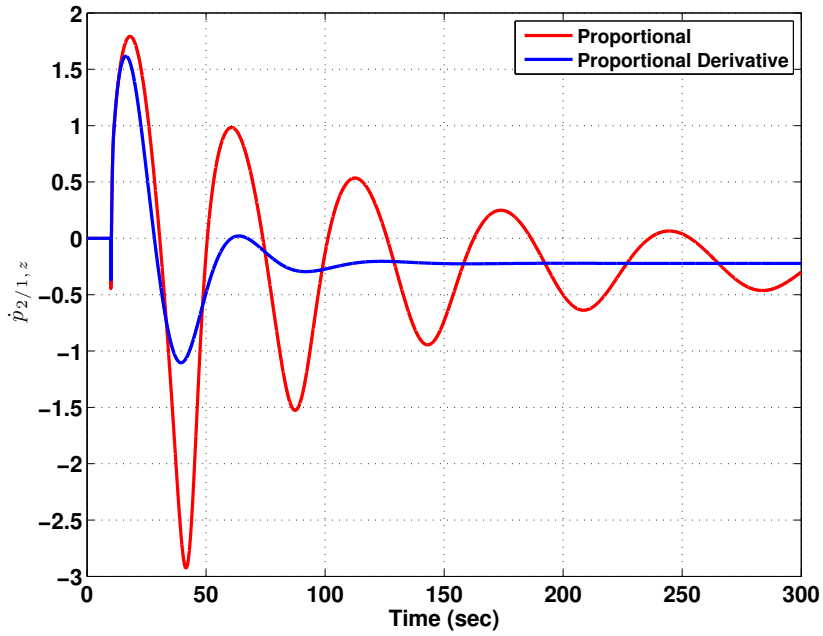

Figure 5.7. Ascent rate comparison obtained with two types of controllers

Figure 5.8 shows the relative altitude of the parafoil-payload system with respect to the ship. The negative sign indicates that the system is moving above the ground, since the inertial frame of reference has positive Z direction towards earth. The initial loss of altitude in the transient phase is minimized using the PD controller.

The input, the tow cable payout rate, is shown in Figure 5.9. The steady state tow cable payout rate corresponds to the maximum ascent rate in Table 5.1. Note that the $\dot{L}$ is always positive. As discussed earlier, the tow cable tension is also an important factor, which should be kept within certain limits, to avoid unstable flight regimes due to lateral disturbance. Hence the tow cable tension is monitored for both the controllers as shown in Figure 5.10. The tension in the cable reduces initially, which corresponds to the sudden cable payout. The sudden increase in the tension, due to the proportional control transients correspond to the reduced tow cable payout rate. These transients are significantly reduced

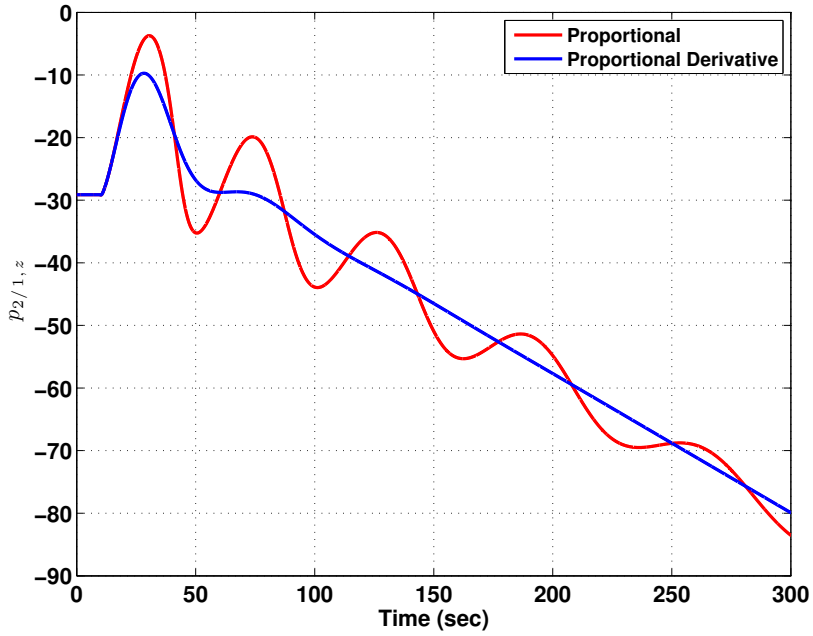

Figure 5.8. Relative altitude between parafoil-payload system and ship:comparison obtained with two types of controllers

using the proportional derivative controller.

Overall, it can be concluded that a simple proportional controller can create significant oscillating tow up with large tension in the cable during transient response. Instead, a proportional derivative controller provides much faster and smoother tow up.

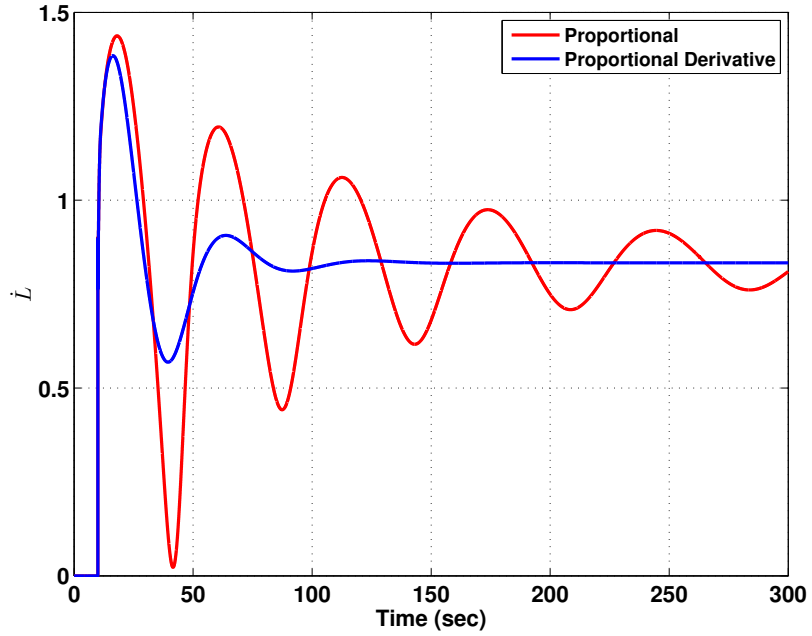

Figure 5.9. The tow cable payout rate required with two types of controllers

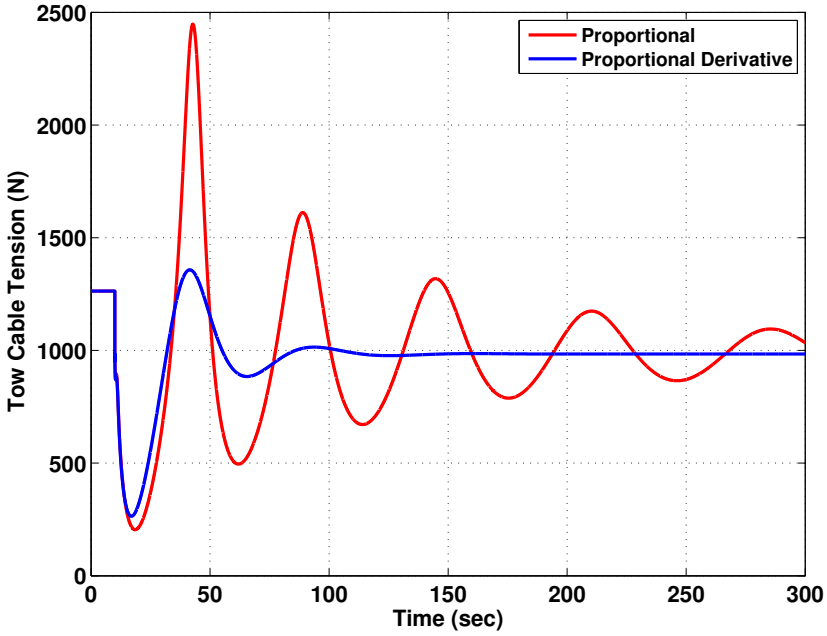

Figure 5.10. The Tow Cable Tension With Two Types of Controllers

5.4 Lateral Stability Control

In addition to the speed of the tow up, the other main objective of the control design is to maintain the lateral stability of the flight, in the event of wind disturbances. This section will focus on the control system development to stabilize the unstable open loop flight regimes. As discussed earlier, in the steady state flight condition with zero asymmetric brake deflection, the linear model can be easily decoupled into the longitudinal and lateral state equations. A lateral state feedback controller is presented in next subsection. For all the steady state configurations with nonzero asymmetric brake deflection, the system *cannot* be decoupled into longitudinal and lateral models. In those cases, a full state feedback control law has to be used, which will be illustrated in subsection 5.4.2.

5.4.1 Lateral State Feedback Controller

The states ψ_1, ϕ_2 and ψ_2 and their corresponding rates form the lateral model. To differentiate lateral state vector from the full state vector, it will be represented with **x** symbol.

$$\mathbf{x} = \begin{bmatrix} \Delta\psi_1 & \Delta\phi_2 & \Delta\psi_2 & \Delta\dot{\psi}_1 & \Delta\dot{\phi}_2 & \Delta\dot{\psi}_2 \end{bmatrix}^T \tag{5.18}$$

The input is the asymmetric brake deflection δ_a. An A_{lat} matrix of size 6×6, the lateral input model B_{lat} of size 6×1 and a output matrix C_{lat}, of size 6×6 forms the system. The lateral model is represented as shown in Equation 5.19.

$$\begin{aligned} \dot{\mathbf{x}} &= A_{lat}\mathbf{x} + B_{lat}\delta_a \\ \mathbf{y} &= C_{lat}\mathbf{x} \end{aligned} \tag{5.19}$$

In the state feedback control, the input δ_a is obtained from the states as shown in Equation 5.20.

$$\delta_a = -K_{lat}\mathbf{x} \tag{5.20}$$

where, K_{lat} is of size 1×6 in this case. Substituting Equation 5.20 in Equation 5.19 yields,

$$\begin{aligned} \dot{\mathbf{x}} &= (A_{lat} - B_{lat}K_{lat})\,\mathbf{x} \\ \mathbf{y} &= C_{lat}\mathbf{x} \end{aligned} \tag{5.21}$$

The lateral state feedback control system is shown in Figure 5.11. The purpose of this controller is to stabilize the linear model around an unstable steady state configuration. Consider a steady state configuration with reference to Table 4.1 to Table 4.5, with asymmetric brake deflection set to zero and the wind is blowing at an azimuth angle of $\mu = 90^\circ$ and elevation angle of $\eta = 20^\circ$ such that, $\left|\frac{V_w}{V_{shp}} = 1\right|$. This is an unstable steady state configuration in open loop. The lateral model in this configuration is computed using Maple and is described in Equation 5.22.

$$\begin{Bmatrix} \Delta\dot{\psi}_1 \\ \Delta\dot{\phi}_2 \\ \Delta\dot{\psi}_2 \\ \Delta\ddot{\psi}_1 \\ \Delta\ddot{\phi}_2 \\ \Delta\ddot{\psi}_2 \end{Bmatrix} = \begin{bmatrix} 0.0 & 0.0 & 0.0 & 1.0 & 0.0 & 0.0 \\ 0.0 & 0.0 & 0.0 & 0.0 & 1.0 & 0.0 \\ 0.0 & 0.0 & 0.0 & 0.0 & 0.0 & 1.0 \\ -0.59 & -3.9 & 3.8 & 5.5 & -3.7 & 0.85 \\ -0.53 & -12.0 & 25.0 & 42.0 & -27.0 & 5.4 \\ 1.0 & 1.3 & 3.4 & 7.5 & -4.0 & -0.70 \end{bmatrix} \begin{Bmatrix} \Delta\psi_1 \\ \Delta\phi_2 \\ \Delta\psi_2 \\ \Delta\psi_1 \\ \Delta\phi_2 \\ \Delta\psi_2 \end{Bmatrix} + \begin{bmatrix} 0.0 \\ 0.0 \\ 0.0 \\ -0.17 \\ 1.0 \\ 2.4 \end{bmatrix} \delta_a \tag{5.22}$$

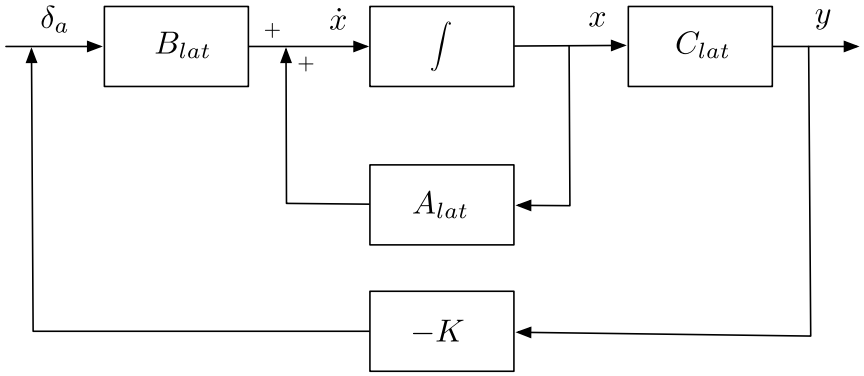

Figure 5.11. Laterel State Feedback Control Law

The eigenvalues of this system are shown in Equation 5.23

$$\lambda_{1..6} = \left\{ \begin{array}{c} -20.67 \\ -0.66 \pm 1.94i \\ 0.02 \pm 0.56i \end{array} \right\} \tag{5.23}$$

It can be observed that a pair of eigenvalues is in the right half plane and hence the system is unstable. The purpose of the state feedback controller is to place all the poles in the left half plane. Let the desired eigenvalues be as shown in Equation 5.24.

$$\lambda_{des_{1..6}} = \left\{ \begin{array}{c} -20.67 \\ -0.66 \pm 1.94i \\ -0.98 \pm 0.56i \end{array} \right\} \tag{5.24}$$

The rationale behind choosing these desired eigen values is to cause minimum change in the poles to stabilize the system, so that the controller gain values are not very high. Using the place command in Matlab, the controller gains can be determined to place the closed loop poles in the desired location, while minimizing the L_2 norm of the gain vector. The K

matrix is shown in Equation 5.25

$$K = [\ -0.4285 \quad -0.0781 \quad 2.0875 \quad 2.0032 \quad -0.4334 \quad 1.1762\ ] \tag{5.25}$$

The controller performance is tested in Matlab/Simulink environment. Three systems are considered:

1. Open loop nonlinear system
2. Open loop linear system
3. Closed loop linear system

All the systems are started with steady state flight condition. A wind disturbance input is provided to all the systems starting at 10 seconds, with a time constant of 0.2 seconds as shown in Figure 5.12.

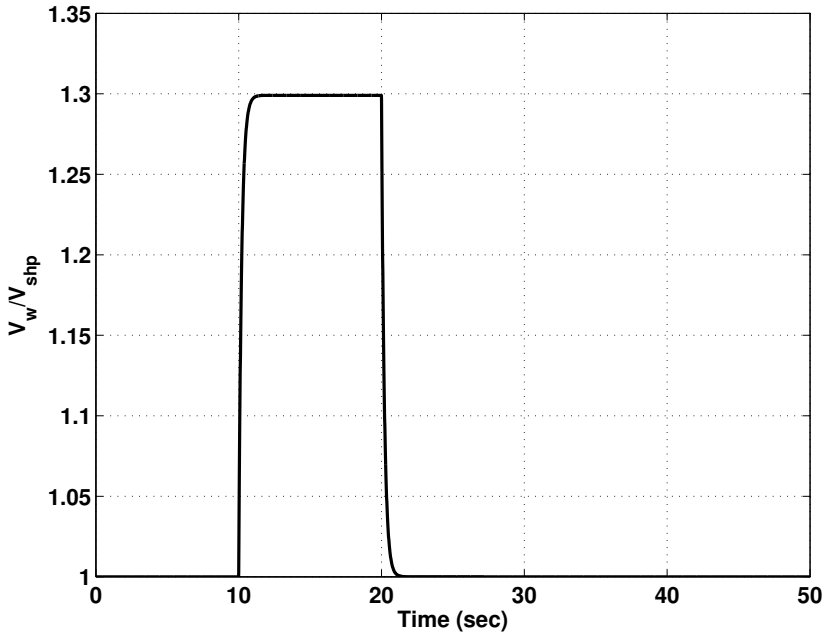

Figure 5.12. Wind Disturbance Input to Unstable Steady State Flight Equilibrium

The open loop nonlinear and linear systems go unstable due to this wind disturbance. The linear system with closed loop lateral state feedback controller stabilizes the system and brings it back to its steady state equilibrium flight condition as shown in Figure 5.13.

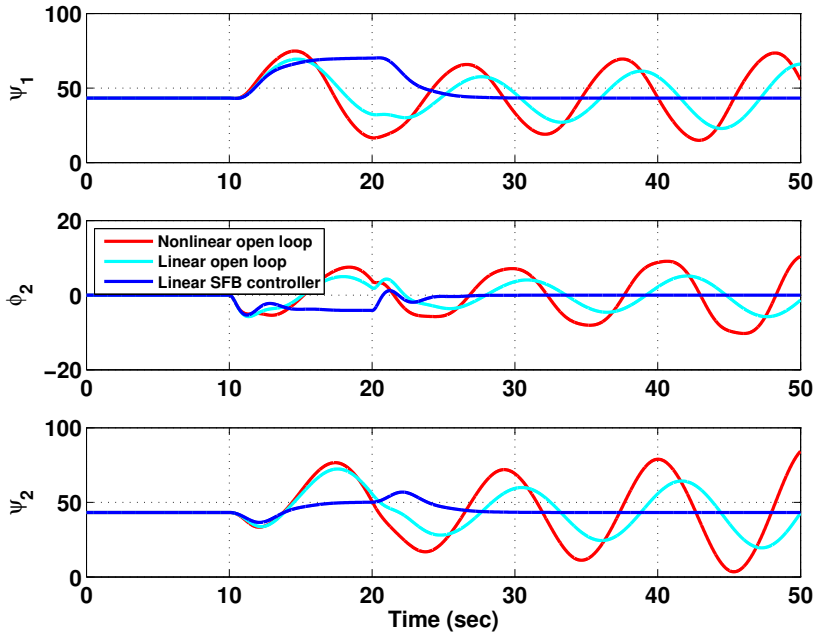

Figure 5.13. The lateral state feedback controller performance

This stabilizing efect is achieved with minimal control effort in asymmetric brake deflection as shown in Figure 5.14.

5.4.2 Full State Feedback Controller

The lateral state feedback controller is designed for the steady state flight configuration with zero asymmetric brake deflections. There are other steady states, where the asymmetric brake deflection is not zero. Moreover, as the asymmetric brake increases, the stability regime keeps on reducing and the instability is caused due to slightest disturbances in the inputs. To avoid such instabilities, a full state feedback controller is required. A schematic of the full state feedback controller is shown in Figure 5.15.

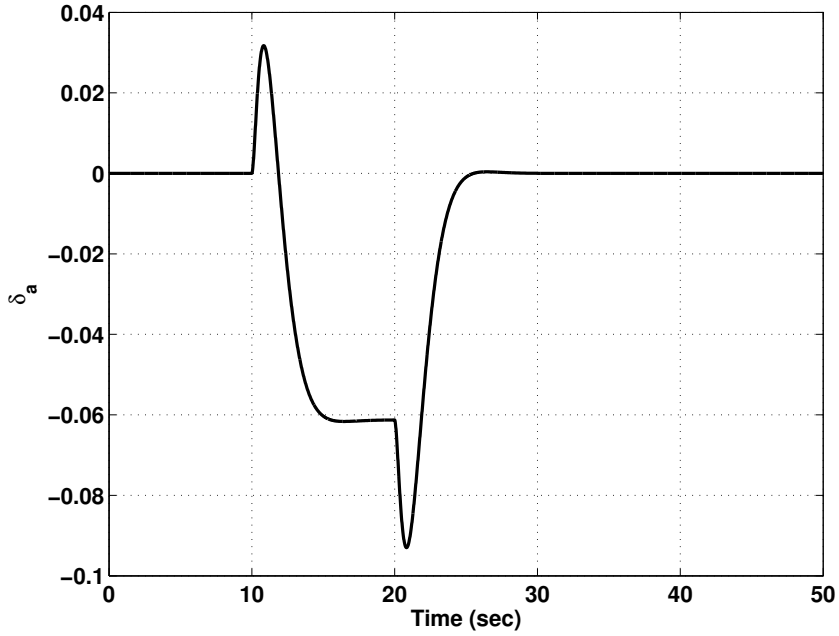

Figure 5.14. The Lateral State Feedback Controller Input: δ_a

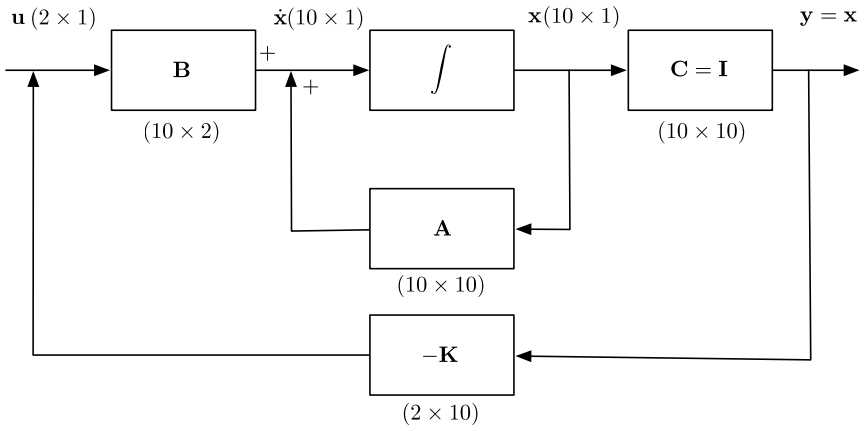

Figure 5.15. The schematic of Full State Feedback Controller

An unstable steady state flight condition with non-zero asymmetric brake deflection is chosen for stability control as discussed in subsection 5.2.4. The linear model is developed using Maple and is shown in Equation 5.15. The eigenvalues of this unstable flight condition are:

$$\lambda_{1..10} = \left\{ \begin{array}{l} -19.67 \\ -4.57 \\ -1.95 \\ -0.55 \pm 1.74i \\ -0.89 \pm 0.26i \\ 0.02 \pm 0.51i \\ -0.33 \end{array} \right\} \tag{5.26}$$

The state feedback control gain matrix is evaluated in MATLAB and is shown in Equation 5.27.

$$K = \left[\begin{array}{cccccccccc} -1.13 & -0.05 & -0.45 & -0.29 & -0.08 & 1.46 & 0.02 & -0.07 & -0.23 & 0.06 \\ -3.80 & -0.50 & -0.93 & 1.89 & 3.33 & -0.58 & 5.92 & -0.77 & 0.90 & 2.22 \end{array} \right] \tag{5.27}$$

Figure 5.16 shows the wind disturbance acting on the three systems which will be compared: Nonlinear, linear and the linear with full state feedback controller.

Figure 5.17 and 5.18 shows the lateral and the longitudinal states of the system for all the three systems under test. It can be observed that the state feedback controller stabilizes all the states to its equilibrium values.

In full state feedback controller, both the control inputs δ_s and δ_a are used to stabilize the system, since the linear state system is coupled. It should be noted that both the inputs are set to a equilibrium value of 0.2 in steady state flight.

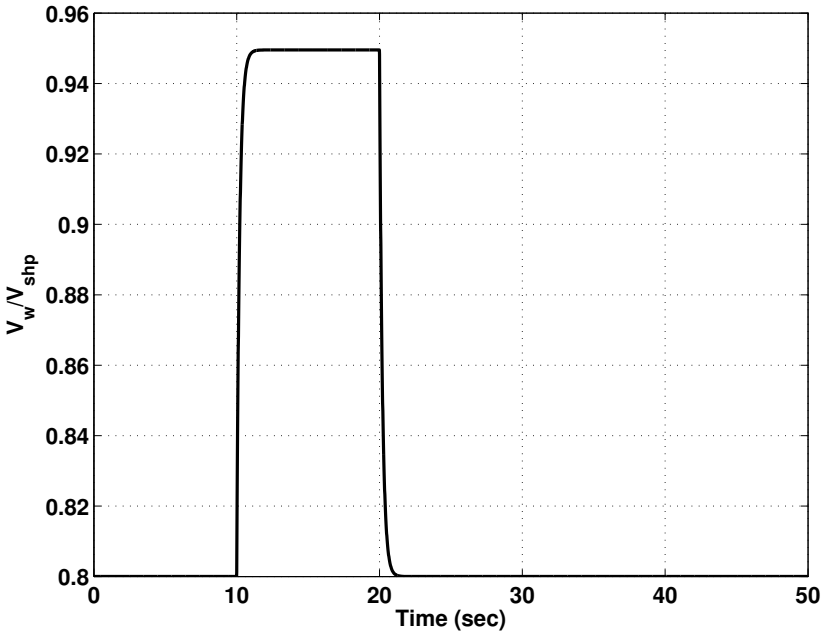

Figure 5.16. Wind Disturbance Input to Unstable Steady State Flight Equilibrium with $\delta_{a_0} = 0.2$

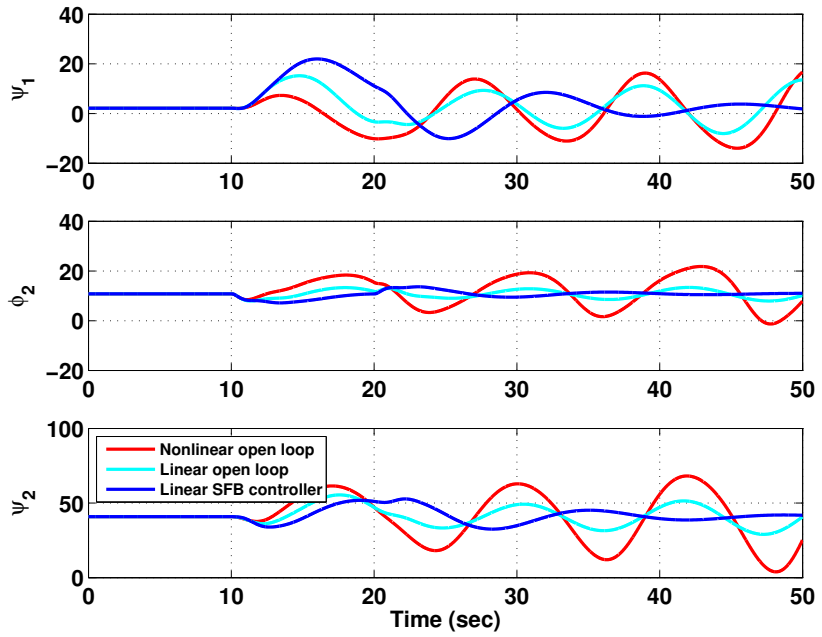

Figure 5.17. Lateral States

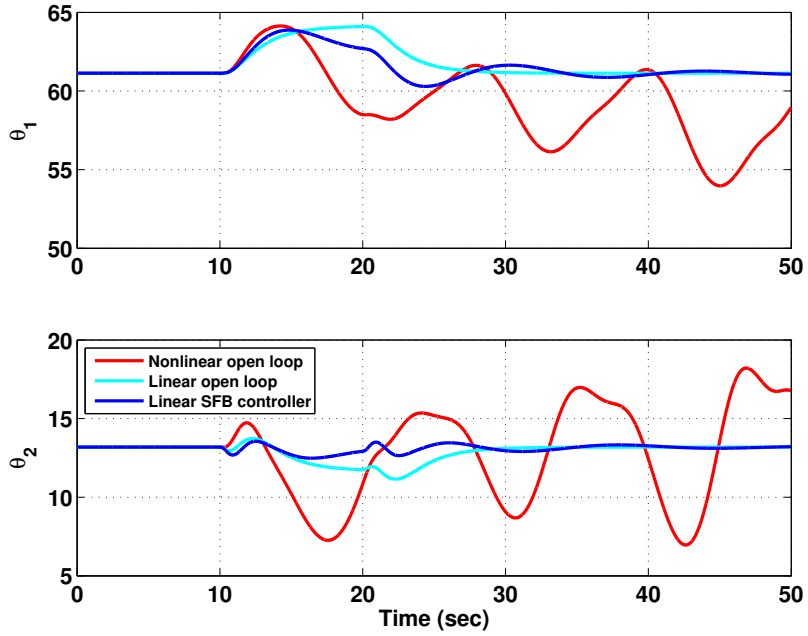

Figure 5.18. Longitudinal States

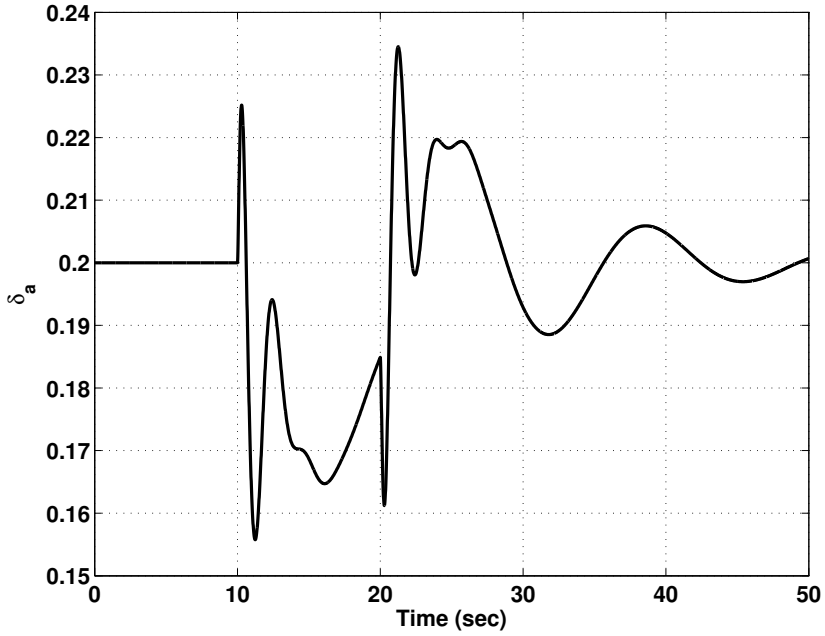

Figure 5.19. The State Feedback Controller Input: δ_a

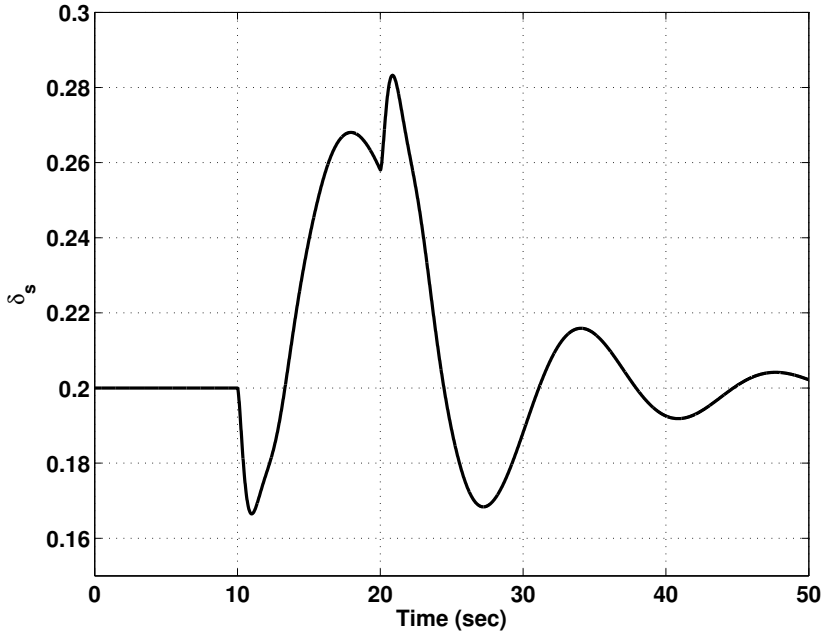

Figure 5.20. The State Feedback Controller Input: δ_s

5.5 Conclusions

The two main control goals during tow up are stability and ascent rate. The various factors affecting the tow up performance are analyzed in simulation environment. It was found that the symmetric brake deflection and the cable payout rate are the two main inputs of the longitudinal model, which can be used to design the tow up control strategy decoupled from the lateral control system. A simple proportional controller, along with a PD controller are designed and tested. The PD controller is better suited for tow up control, for smooth and fast tow up.

The stability of the system was analyzed in Chapter 4. Two different type of controllers are investigated for their ability to stabilize an unstable equilibrium point. In steady state flight conditions with zero asymmetric brake deflection, a lateral state feedback controller can be used to stabilize the system for wind disturbances. In more severe equilibrium states,

involving non zero asymmetric brake deflection, a full state feedback controller can be used to stabilized the system.

6. Conclusions And Future Work

While previous research has focused on modeling the parafoil-payload system which is released from an airborne vehicle, this research focused on the modeling, simulation and control design of a towed parafoil-payload system. A nonlinear dynamic model of the towed parafoil-payload system was developed for its application to the Ship Launched Aerial Delivery System, SLADS. The main difference between the paragliders and conventional gliders is the flexible wing structure without a stabilizer, due to which, the aerodynamics of paragliders is significantly different than that of conventional aircraft. Moreover, due to the large vertical distance between the aerodynamic center of the parafoil and the center of mass of the parafoil-payload system, aerodynamic forces create large moment about the center of mass.

A high fidelity model of the towed parafoil-payload system was developed, which incorporated both, the aerodynamic characteristics of a paraglider, and the actual geometric and inertial properties of the parafoil-payload system. The main mechanism of steering a paraglider, the parafoil brakes, were incorporated into the aerodynamic model of the paraglider. The model was simulated in MATLAB/simulink environment, with realistic inputs, parameters and flight conditions. The model was partially validated using a real time simulation using MATLAB and dSPACE, to replicate the flight experience of a pilot towing a paraglider.

The peculiar unstable flight condition of a towed paragliders, called lockout, was investigated by analyzing the stability of the linearized system. It was observed that lockout is more favorable in higher magnitudes of wind gusts, with increasing angle of elevation of the cross wind, higher tensions in the tow cable and larger asymmetric brake deflections. All these effects are consistent with the experiences of a paraglider pilot being towed. Hence it can be concluded that one of the main objectives of modeling the lockout has been successfully accomplished.

One of main objective of SLADS is to tow up the system as fast as possible and maintain stability. A linear model was used to develop the control strategies for accomplishing this. The controllability and observability of the linear model was assessed before designing the control systems. It was found that the system is completely controllable and observable for the available set of inputs and measurable outputs. The inputs include symmetric and asymmetric brake deflections, while the measurable outputs include the tow angles and the angular rates of the parafoil-payload system. A closed loop control strategy was developed for rapid deployment of the system. It was concluded that tow up control can be developed using symmetric brake deflection and cable payout rate in the longitudinal flight mode, decoupled from the lateral control system. Two different types of state feedback controllers were investigated for stabilizing the unstable equilibrium points. It was concluded that the otherwise, irrecoverable flight condition, lockout, can be controlled using a sate feedback controller.

Thus a mathematical model of a towed parafoil-payload system was developed and simulated. The linear model of the system was used to design control strategies for rapid deployment and maintaining stability. Since this is the first formal treatment of towed paragliders, there is a vast amount of scope to further investigate the complex dynamics of the towed flight systems. A few important steps forward in this area of research are

outlined below.

1. One of the main control inputs used by the pilots towing a paraglider, in addition to the trailing edge deflection, is the weight shifting technique. A higher degree of freedom model, which can incorporate relative motion between parafoil and payload can be developed to simulate the towed system in more realistic way.

2. The experimental investigation of the towed paragliders can facilitate more refined aerodynamic characteristics of this flexible wing structure.

3. The launching phase of the towed paraglider is very critical in terms of rapid deployment and stability. A more detailed model can be developed to incorporate the initial launching phase.

4. The control strategies developed in this work, can be tested in the actual towed autonomous paraglider systems.

5. A more comprehensive control strategy can be developed to maintain stability in severe wind disturbances and use advanced control techniques to recover from a range of unstable flight configurations.

REFERENCES

[1] "A Wikipedia article on parachutes [Internet]." Available from: http://en.wikipedia.org/wiki/Parachute.

[2] Manske M, "Parasailing image in public domain [Internet]," February 5 2008. Available from: http://en.wikipedia.org/wiki/File:ParasailingDR.JPG.

[3] "Copyright image owned by Flight Concepts International [Internet]." Available from: http://flightconceptsint.com/powered.

[4] "NASA Photo: EC01-0339-146, Dryden Flight Research Center [Internet]," December 13 2001. Available from: http://www.dfrc.nasa.gov/gallery/photo/X-38/Medium/EC01-0339-146.jpg.

[5] Slegers N, Costello M, "Aspects of Control for a Parafoil and Payload System," *Journal of Guidance, Control and Dynamics*, vol. 26, pp. 898–905, November-December 2003.

[6] Goodrick TF, "Theoretical Study of the Longitudinal Stability of High-Performance Fliding Airdrop Systems," in *5th AIAA Aerodynamic Decelerator Systems Technology Conference and Seminar*, (Albuquerque, NM), November 1975.

[7] "A Wikipedia article on Gliding Flight [Internet]." Available from: http://en.wikipedia.org/wiki/Gliding_flight.

[8] Hartsfield J, "NASA News[Internet]," February 4 2000. Available from: http://www.nasa.gov/centers/johnson/news/releases/1999_2001/j00-9.html.

[9] Jann T, "Aerodynamic Model Identification and GNC Design For The Parafoil-Load System ALEX," in *16th AIAA Aerodynamic Decelerator Systems Technology Conference and Seminar*, (Boston, MA), 2001.

[10] Tsai HB, Meiners MA, Lahr EK, "Analytical and Experimental Study of a Recovery Guidance System at Iowa State University," tech. rep., Iowa State University of Science and Technology, Ames, IA, 1999.

[11] Sego WK, "Development of a High Glide Autonomous Aerial Delivery System - 'Pegasus 500 (APADS)'," in *16th AIAA Aerodynamic Decelerator Systems Technology Conference and Seminar*, (Boston, MA), 2001.

[12] Yakimenko OA, "On The Development of a Scalable 8-DoF Model for a Generic Parafoil-Payload Delivery System," in *18th AIAA Aerodynamic Decelerator Systems Technology Conference and Seminar*, (Munich, Germany), 2005.

[13] "A Wikipedia article on parasailing [Internet]." Available from: http://en.wikipedia.org/wiki/Parasailing.

[14] Pagen D, *The Art Of Paragliding*. Black Mountain Books, 1st ed., 2001.

[15] Rogallo GS, Rogallo FM, "Patent: Flexible Kite," March 1951. Patent No. 2546078.

[16] Jalbert DC, "Patent: Multi-Cell Wing Type Aerial Device," November 1966. Patent No. 3285546.

[17] Lingard JS, “The Performance and Design of Ram-Air Parachutes,” Tech. Rep. TR-81-103, UK Royal Aircraft Establishment, Farnborough, 1981.

[18] Dobrokhodov VN, Yakimenko OA, Junge CJ, “Six-Degree-of-Freedom Model of a Controlled Circular Parachute,” in *AIAA Atmospheric Flight Mechanics Conference*, (Monterey, CA), August 2002.

[19] Müller S, Wagner O, Sachs G, “A High-Fidelity Nonlinear Multibody Simulation Model For Parafoil Systems,” in *17th AIAA Aerodynamic Decelerator Systems Technology Conference and Seminar*, (Monterey, CA), May 2003.

[20] Doherr K, Schilling H, “9DOF-Simulation Of Rotating Parachute Systems,” in *11th AIAA Aerodynamic Decelerator Systems Technology Conference and Seminar*, (Baltimore, MD), 1991.

[21] Wolf DF, *The Dynamic Stability of a Non-Rigid Parachute and Payload System*. PhD thesis, University of Rhode Island, Kingston, RI, 1968.

[22] Crimi P, “Lateral Stability of Gliding Parachutes,” *Journal of Guidance, Control and Dynamics*, vol. 13, pp. 1060–1063, November-December 1990.

[23] Brown GJ, “Parafoil Steady Turn Response To Control Input,” in *12th AIAA Aerodynamic Decelerator Systems Technology Conference and Seminar*, (London, England), 1993.

[24] Lissaman PBS, Brown GJ, “Apparent Mass Effects On Parafoil Dynamics,” in *12th AIAA Aerodynamic Decelerator Systems Technology Conference and Seminar*, (London, England), 1993.

[25] Farlex Inc., "Content on TheFreeDictionary.com distributed under the terms of GNU Free Documentation License [Internet]." Available from: http://encyclopedia2.thefreedictionary.com/Apparent+Mass.

[26] Akovali G, *Handbook of Composite Fabrication*. Smithers Rapra Press, 1st ed., January 1 2001. 204 p.

[27] Baruh H, *Analytical Dynamics*. McGraw-Hill Science/Engineering/Math, 1st ed., 1998. 744 p.

[28] Mortaloni PA, Yakimenko OA, Dobrokhodov VN, Howard RM, "On The Develpment Of A Six-Degree-Of-Freedom Model Of A Low-Aspect-Ratio Parafoil Delivery System," in *17th AIAA Aerodynamic Decelerator Systems Technology Conference and Seminar*, (Monterey, CA), May 2003.

[29] "USHPA Pilot Proficiency Program," tech. rep., United States Hang Gliding and Paragliding Association, Inc., Colorado Springs, CO 80904, 2007.

[30] Pagen D, Bryden B, *Towing Aloft*. Black Mountain Books, 1st ed., 1997.

[31] Slotine JJE, Li W, *Applied Nonlinear Control*. Prentice Hall, 1st ed., 1991.

[32] Chen CT, *Linear System Theory and Design*. Oxford University Press, Inc., 3rd ed., 1998.

[33] "NASA images Download Terms and Conditions [Internet]," July 3 2008. Available from: http://www.nasaimages.org/Terms.html.

A. Nonlinear Dynamic Equation Coefficients

$$
\begin{aligned}
A_{11} &= mL^2 \\
A_{12} &= 0 \\
A_{13} &= mL\big[r_{3/2,z}\sin(\theta_1)\sin(\psi_1)\cos(\phi_2)\cos(\psi_2) \\
&\quad + r_{3/2,z}\sin(\theta_1)\sin(\psi_1)\sin(\phi_2)\sin(\theta_2)\sin(\psi_2) \\
&\quad + r_{3/2,y}\sin(\theta_1)\sin(\psi_1)\sin(\phi_2)\cos(\psi_2) \\
&\quad - r_{3/2,y}\sin(\theta_1)\sin(\psi_1)\cos(\phi_2)\sin(\theta_2)\sin(\psi_2) \\
&\quad - r_{3/2,z}\sin(\theta_1)\cos(\psi_1)\cos(\phi_2)\sin(\psi_2) \\
&\quad + r_{3/2,z}\sin(\theta_1)\cos(\psi_1)\sin(\phi_2)\sin(\theta_2)\cos(\psi_2) \\
&\quad - r_{3/2,y}\sin(\theta_1)\cos(\psi_1)\sin(\phi_2)\sin(\psi_2) \\
&\quad - r_{3/2,y}\sin(\theta_1)\cos(\psi_1)\cos(\phi_2)\sin(\theta_2)\cos(\psi_2) \\
&\quad - r_{3/2,z}\cos(\theta_1)\sin(\phi_2)\cos(\theta_2) \\
&\quad + r_{3/2,y}\cos(\theta_1)\cos(\phi_2)\cos(\theta_2)\big]
\end{aligned}
$$

$$
\begin{aligned}
A_{14} = mL \big[& r_{3/2,x} \sin(\theta_1) \sin(\psi_1) \sin(\theta_2) \sin(\psi_2) \\
& - r_{3/2,z} \sin(\theta_1) \sin(\psi_1) \cos(\theta_2) \sin(\psi_2) \cos(\phi_2) \\
& - r_{3/2,y} \sin(\theta_1) \sin(\psi_1) \cos(\theta_2) \sin(\psi_2) \sin(\phi_2) \\
& - r_{3/2,z} \cos(\theta_1) \cos(\phi_2) \sin(\theta_2) \\
& - r_{3/2,y} \cos(\theta_1) \sin(\phi_2) \sin(\theta_2) \\
& - r_{3/2,x} \cos(\theta_1) \cos(\theta_2) \\
& + r_{3/2,x} \sin(\theta_1) \cos(\psi_1) \sin(\theta_2) \cos(\psi_2) \\
& - r_{3/2,z} \sin(\theta_1) \cos(\psi_1) \cos(\theta_2) \cos(\psi_2) \cos(\phi_2) \\
& - r_{3/2,y} \sin(\theta_1) \cos(\psi_1) \cos(\theta_2) \cos(\psi_2) \sin(\phi_2) \big] \\
A_{15} = mL \sin(\theta_1) \big[& - \sin(\psi_1) \cos(\phi_2) \cos(\psi_2) \sin(\theta_2) \, r_{3/2,z} \\
& - \sin(\psi_1) \sin(\phi_2) \sin(\psi_2) \, r_{3/2,z} \\
& - \sin(\psi_1) \sin(\phi_2) \cos(\psi_2) \sin(\theta_2) \, r_{3/2,y} \\
& - \sin(\psi_1) \cos(\psi_2) \cos(\theta_2) \, r_{3/2,x} \\
& + \sin(\psi_1) \cos(\phi_2) \sin(\psi_2) \, r_{3/2,y} \\
& + \cos(\psi_1) \cos(\phi_2) \sin(\psi_2) \sin(\theta_2) \, r_{3/2,z} \\
& - \cos(\psi_1) \sin(\phi_2) \cos(\psi_2) \, r_{3/2,z} \\
& + \cos(\psi_1) \sin(\phi_2) \sin(\psi_2) \sin(\theta_2) \, r_{3/2,y} \\
& + \cos(\psi_1) \sin(\psi_2) \cos(\theta_2) \, r_{3/2,x} \\
& + \cos(\psi_1) \cos(\phi_2) \cos(\psi_2) \, r_{3/2,y} \big] \\
A_{21} = & \; 0 \\
A_{22} = & \; mL^2 \left(\cos(\theta_1) \right)^2
\end{aligned}
$$

$$
\begin{aligned}
A_{23} = & -mL\cos(\theta_1)\left[\sin(\psi_1)\, r_{3/2,z}\cos(\phi_2)\sin(\psi_2)\right. \\
& -\sin(\psi_1)\, r_{3/2,z}\sin(\phi_2)\sin(\theta_2)\cos(\psi_2) \\
& +\sin(\psi_1)\, r_{3/2,y}\sin(\phi_2)\sin(\psi_2) \\
& +\sin(\psi_1)\, r_{3/2,y}\cos(\phi_2)\sin(\theta_2)\cos(\psi_2) \\
& +\cos(\psi_1)\, r_{3/2,z}\cos(\phi_2)\cos(\psi_2) \\
& +\cos(\psi_1)\, r_{3/2,z}\sin(\phi_2)\sin(\theta_2)\sin(\psi_2) \\
& +\cos(\psi_1)\, r_{3/2,y}\sin(\phi_2)\cos(\psi_2) \\
& \left.-\cos(\psi_1)\, r_{3/2,y}\cos(\phi_2)\sin(\theta_2)\sin(\psi_2)\right] \\
A_{24} = & \; mL\cos(\theta_1)\left[\sin(\psi_1)\, r_{3/2,x}\sin(\theta_2)\cos(\psi_2)\right. \\
& -\sin(\psi_1)\cos(\theta_2)\cos(\psi_2)\cos(\phi_2)\, r_{3/2,z} \\
& -\sin(\psi_1)\cos(\theta_2)\cos(\psi_2)\sin(\phi_2)\, r_{3/2,y} \\
& -\cos(\psi_1)\, r_{3/2,x}\sin(\theta_2)\sin(\psi_2) \\
& +\cos(\psi_1)\cos(\theta_2)\sin(\psi_2)\cos(\phi_2)\, r_{3/2,z} \\
& \left.+\cos(\psi_1)\cos(\theta_2)\sin(\psi_2)\sin(\phi_2)\, r_{3/2,y}\right] \\
A_{25} = & \; mL\cos(\theta_1)\left[\sin(\psi_1)\cos(\phi_2)\sin(\psi_2)\sin(\theta_2)\, r_{3/2,z}\right. \\
& -\sin(\psi_1)\sin(\phi_2)\cos(\psi_2)\, r_{3/2,z} \\
& +\sin(\psi_1)\sin(\phi_2)\sin(\psi_2)\sin(\theta_2)\, r_{3/2,y} \\
& +\sin(\psi_1)\sin(\psi_2)\cos(\theta_2)\, r_{3/2,x} \\
& +\sin(\psi_1)\cos(\phi_2)\cos(\psi_2)\, r_{3/2,y} \\
& +\cos(\psi_1)\cos(\phi_2)\cos(\psi_2)\sin(\theta_2)\, r_{3/2,z} \\
& +\cos(\psi_1)\sin(\phi_2)\sin(\psi_2)\, r_{3/2,z} \\
& +\cos(\psi_1)\sin(\phi_2)\cos(\psi_2)\sin(\theta_2)\, r_{3/2,y} \\
& +\cos(\psi_1)\cos(\psi_2)\cos(\theta_2)\, r_{3/2,x} \\
& \left.-\cos(\psi_1)\cos(\phi_2)\sin(\psi_2)\, r_{3/2,y}\right]
\end{aligned}
$$

$$
\begin{aligned}
A_{31} = mL \big[& \sin(\theta_1) \sin(\psi_1) r_{3/2,z} \cos(\phi_2) \cos(\psi_2) \\
& + \sin(\theta_1) \sin(\psi_1) r_{3/2,z} \sin(\phi_2) \sin(\theta_2) \sin(\psi_2) \\
& + \sin(\theta_1) \sin(\psi_1) r_{3/2,y} \sin(\phi_2) \cos(\psi_2) \\
& - \sin(\theta_1) \sin(\psi_1) r_{3/2,y} \cos(\phi_2) \sin(\theta_2) \sin(\psi_2) \\
& - \sin(\theta_1) \cos(\psi_1) r_{3/2,z} \cos(\phi_2) \sin(\psi_2) \\
& + \sin(\theta_1) \cos(\psi_1) r_{3/2,z} \sin(\phi_2) \sin(\theta_2) \cos(\psi_2) \\
& - \sin(\theta_1) \cos(\psi_1) r_{3/2,y} \sin(\phi_2) \sin(\psi_2) \\
& - \sin(\theta_1) \cos(\psi_1) r_{3/2,y} \cos(\phi_2) \sin(\theta_2) \cos(\psi_2) \\
& - \cos(\theta_1) \sin(\phi_2) \cos(\theta_2) r_{3/2,z} \\
& + \cos(\theta_1) \cos(\phi_2) \cos(\theta_2) r_{3/2,y} \big] \\
A_{32} = -m & \cos(\theta_1) L \big(\sin(\psi_1) r_{3/2,z} \cos(\phi_2) \sin(\psi_2) \\
& - \sin(\psi_1) r_{3/2,z} \sin(\phi_2) \sin(\theta_2) \cos(\psi_2) \\
& + \sin(\psi_1) r_{3/2,y} \sin(\phi_2) \sin(\psi_2) \\
& + \sin(\psi_1) r_{3/2,y} \cos(\phi_2) \sin(\theta_2) \cos(\psi_2) \\
& + \cos(\psi_1) r_{3/2,z} \cos(\phi_2) \cos(\psi_2) \\
& + \cos(\psi_1) r_{3/2,z} \sin(\phi_2) \sin(\theta_2) \sin(\psi_2) \\
& + \cos(\psi_1) r_{3/2,y} \sin(\phi_2) \cos(\psi_2) \\
& - \cos(\psi_1) r_{3/2,y} \cos(\phi_2) \sin(\theta_2) \sin(\psi_2) \big) \\
A_{33} = & I_{xx} + m {r_{3/2,y}}^2 + m {r_{3/2,z}}^2 \\
A_{34} = & m r_{3/2,x} \big(\sin(\phi_2) r_{3/2,z} - r_{3/2,y} \cos(\phi_2) \big) \\
A_{35} = & - \sin(\theta_2) I_{xx} - m {r_{3/2,z}}^2 \sin(\theta_2) \\
& - m {r_{3/2,y}}^2 \sin(\theta_2) - m r_{3/2,z} \cos(\phi_2) \cos(\theta_2) r_{3/2,x} \\
& - m r_{3/2,y} \sin(\phi_2) \cos(\theta_2) r_{3/2,x}
\end{aligned}
$$

$$
\begin{aligned}
A_{41} = mL \big(& \sin(\theta_1) \sin(\psi_1) r_{3/2,x} \sin(\theta_2) \sin(\psi_2) \\
& - \sin(\theta_1) \sin(\psi_1) \cos(\theta_2) \sin(\psi_2) \cos(\phi_2) r_{3/2,z} \\
& - \sin(\theta_1) \sin(\psi_1) \cos(\theta_2) \sin(\psi_2) \sin(\phi_2) r_{3/2,y} \\
& - \cos(\theta_1) \cos(\phi_2) \sin(\theta_2) r_{3/2,z} \\
& - \cos(\theta_1) \sin(\phi_2) \sin(\theta_2) r_{3/2,y} \\
& - \cos(\theta_1) \cos(\theta_2) r_{3/2,x} \\
& + \sin(\theta_1) \cos(\psi_1) r_{3/2,x} \sin(\theta_2) \cos(\psi_2) \\
& - \sin(\theta_1) \cos(\psi_1) \cos(\theta_2) \cos(\psi_2) \cos(\phi_2) r_{3/2,z} \\
& - \sin(\theta_1) \cos(\psi_1) \cos(\theta_2) \cos(\psi_2) \sin(\phi_2) r_{3/2,y} \big) \\
A_{42} = mL \cos(\theta_1) \big(& \sin(\psi_1) r_{3/2,x} \sin(\theta_2) \cos(\psi_2) \\
& - \sin(\psi_1) \cos(\theta_2) \cos(\psi_2) \cos(\phi_2) r_{3/2,z} \\
& - \sin(\psi_1) \cos(\theta_2) \cos(\psi_2) \sin(\phi_2) r_{3/2,y} \\
& - \cos(\psi_1) r_{3/2,x} \sin(\theta_2) \sin(\psi_2) \\
& + \cos(\psi_1) \cos(\theta_2) \sin(\psi_2) \cos(\phi_2) r_{3/2,z} \\
& + \cos(\psi_1) \cos(\theta_2) \sin(\psi_2) \sin(\phi_2) r_{3/2,y} \big) \\
A_{43} = {} & m r_{3/2,x} \big(\sin(\phi_2) r_{3/2,z} - r_{3/2,y} \cos(\phi_2) \big) \\
A_{44} = {} & I_{zz} + (\cos(\phi_2))^2 I_{yy} - m {r_{3/2,y}}^2 (\cos(\phi_2))^2 \\
& + m (\cos(\phi_2))^2 {r_{3/2,z}}^2 + m {r_{3/2,y}}^2 \\
& + 2\, m \cos(\phi_2) r_{3/2,z} \sin(\phi_2) r_{3/2,y} \\
& + m {r_{3/2,x}}^2 - I_{zz} (\cos(\phi_2))^2
\end{aligned}
$$

$$
\begin{aligned}
A_{45} = & \sin(\phi_2)\cos(\theta_2)\, I_{yy}\cos(\phi_2) \\
& - \cos(\phi_2)\cos(\theta_2)\, I_{zz}\sin(\phi_2) \\
& + m r_{3/2,x}\sin(\theta_2)\cos(\phi_2)\, r_{3/2,y} \\
& + m\cos(\theta_2)\, r_{3/2,y} r_{3/2,z} - 2\, m\cos(\theta_2)\, r_{3/2,y} r_{3/2,z}\left(\cos(\phi_2)\right)^2 \\
& + m\cos(\theta_2)\cos(\phi_2)\, {r_{3/2,z}}^2 \sin(\phi_2) \\
& - m\sin(\phi_2)\, r_{3/2,x}\sin(\theta_2)\, r_{3/2,z} \\
& - m\cos(\theta_2)\sin(\phi_2)\, {r_{3/2,y}}^2 \cos(\phi_2) \\
A_{51} = & \, mL\sin(\theta_1)\big(-\sin(\psi_1)\cos(\phi_2)\cos(\psi_2)\sin(\theta_2)\, r_{3/2,z} \\
& - \sin(\psi_1)\sin(\phi_2)\sin(\psi_2)\, r_{3/2,z} \\
& - \sin(\psi_1)\sin(\phi_2)\cos(\psi_2)\sin(\theta_2)\, r_{3/2,y} \\
& - \sin(\psi_1)\cos(\psi_2)\cos(\theta_2)\, r_{3/2,x} \\
& + \sin(\psi_1)\cos(\phi_2)\sin(\psi_2)\, r_{3/2,y} \\
& + \cos(\psi_1)\cos(\phi_2)\sin(\psi_2)\sin(\theta_2)\, r_{3/2,z} \\
& - \cos(\psi_1)\sin(\phi_2)\cos(\psi_2)\, r_{3/2,z} \\
& + \cos(\psi_1)\sin(\phi_2)\sin(\psi_2)\sin(\theta_2)\, r_{3/2,y} \\
& + \cos(\psi_1)\sin(\psi_2)\cos(\theta_2)\, r_{3/2,x} \\
& + \cos(\psi_1)\cos(\phi_2)\cos(\psi_2)\, r_{3/2,y}\big)
\end{aligned}
$$

$$
\begin{aligned}
A_{52} = & mL\cos(\theta_1)\left(\sin(\psi_1)\cos(\phi_2)\sin(\psi_2)\sin(\theta_2)\, r_{3/2,z}\right. \\
& - \sin(\psi_1)\sin(\phi_2)\cos(\psi_2)\, r_{3/2,z} \\
& + \sin(\psi_1)\sin(\phi_2)\sin(\psi_2)\sin(\theta_2)\, r_{3/2,y} \\
& + \sin(\psi_1)\sin(\psi_2)\cos(\theta_2)\, r_{3/2,x} \\
& + \sin(\psi_1)\cos(\phi_2)\cos(\psi_2)\, r_{3/2,y} \\
& + \cos(\psi_1)\cos(\phi_2)\cos(\psi_2)\sin(\theta_2)\, r_{3/2,z} \\
& + \cos(\psi_1)\sin(\phi_2)\sin(\psi_2)\, r_{3/2,z} \\
& + \cos(\psi_1)\sin(\phi_2)\cos(\psi_2)\sin(\theta_2)\, r_{3/2,y} \\
& + \cos(\psi_1)\cos(\psi_2)\cos(\theta_2)\, r_{3/2,x} \\
& \left. - \cos(\psi_1)\cos(\phi_2)\sin(\psi_2)\, r_{3/2,y}\right) \\
A_{53} = & -\sin(\theta_2)\, I_{xx} - m{r_{3/2,z}}^2\sin(\theta_2) \\
& - m{r_{3/2,y}}^2\sin(\theta_2) \\
& - m r_{3/2,z}\cos(\phi_2)\cos(\theta_2)\, r_{3/2,x} \\
& - m r_{3/2,y}\sin(\phi_2)\cos(\theta_2)\, r_{3/2,x} \\
A_{54} = & \sin(\phi_2)\cos(\theta_2)\, I_{yy}\cos(\phi_2) \\
& - \cos(\phi_2)\cos(\theta_2)\, I_{zz}\sin(\phi_2) \\
& + m r_{3/2,x}\sin(\theta_2)\cos(\phi_2)\, r_{3/2,y} \\
& + m\cos(\theta_2)\, r_{3/2,y} r_{3/2,z} \\
& - 2\, m\cos(\theta_2)\, r_{3/2,y} r_{3/2,z}\left(\cos(\phi_2)\right)^2 \\
& + m\cos(\theta_2)\cos(\phi_2)\, {r_{3/2,z}}^2\sin(\phi_2) \\
& - m\sin(\phi_2)\, r_{3/2,x}\sin(\theta_2)\, r_{3/2,z} \\
& - m\cos(\theta_2)\sin(\phi_2)\, {r_{3/2,y}}^2\cos(\phi_2)
\end{aligned}
$$

$$
\begin{aligned}
A_{55} = {} & \left(\cos\left(\phi_2\right)\right)^2 \left(\cos\left(\theta_2\right)\right)^2 I_{zz} + I_{xx} - \\
& m \left(\cos\left(\phi_2\right)\right)^2 {r_{3/2,z}}^2 \left(\cos\left(\theta_2\right)\right)^2 \\
& + m {r_{3/2,y}}^2 \left(\cos\left(\phi_2\right)\right)^2 \left(\cos\left(\theta_2\right)\right)^2 \\
& - I_{xx} \left(\cos\left(\theta_2\right)\right)^2 + \left(\cos\left(\theta_2\right)\right)^2 I_{yy} \\
& - \left(\cos\left(\theta_2\right)\right)^2 I_{yy} \left(\cos\left(\phi_2\right)\right)^2 \\
& - m {r_{3/2,y}}^2 \left(\cos\left(\theta_2\right)\right)^2 \\
& + m {r_{3/2,y}}^2 + m {r_{3/2,z}}^2 - 2\, m \cos\left(\phi_2\right) r_{3/2,z} \sin\left(\phi_2\right) r_{3/2,y} \left(\cos\left(\theta_2\right)\right)^2 \\
& + 2\, m \cos\left(\phi_2\right) \sin\left(\theta_2\right) r_{3/2,z} \cos\left(\theta_2\right) r_{3/2,x} \\
& + 2\, m \sin\left(\phi_2\right) \sin\left(\theta_2\right) r_{3/2,y} \cos\left(\theta_2\right) r_{3/2,x} \\
& + m \left(\cos\left(\theta_2\right)\right)^2 {r_{3/2,x}}^2
\end{aligned}
$$

$$
\begin{aligned}
B_1 = {} & m \sin(\theta_2) \sin(\psi_2) r_{3/2,x} \dot{\theta}_2 \sin(\theta_1) \sin(\psi_1) \dot{L} - mg \cos(\theta_1) L \\
& - m \cos(\theta_2) \cos(\psi_2) r_{3/2,z} \dot{\theta}_2 \cos(\phi_2) \sin(\theta_1) \cos(\psi_1) \dot{L} \\
& - m \sin(\theta_1) \sin(\psi_1) L \cos(\phi_2) \dot{\phi}_2^2 \cos(\psi_2) r_{3/2,y} \\
& + 2 m \sin(\theta_1) \sin(\psi_1) L \cos(\phi_2) \dot{\phi}_2 \cos(\psi_2) r_{3/2,y} \sin(\theta_2) \dot{\psi}_2 \\
& + 2 m \sin(\theta_1) \sin(\psi_1) L \sin(\phi_2) \sin(\psi_2) \dot{\psi}_2 r_{3/2,y} \dot{\phi}_2 \\
& - m \sin(\theta_1) \sin(\psi_1) L \sin(\phi_2) \sin(\psi_2) \dot{\psi}_2^2 r_{3/2,y} \sin(\theta_2) \\
& - m \sin(\theta_1) \sin(\psi_1) L \sin(\phi_2) \dot{\phi}_2^2 \sin(\theta_2) \sin(\psi_2) r_{3/2,y} \\
& + 2 m \sin(\theta_1) \sin(\psi_1) L \cos(\theta_2) \cos(\psi_2) \dot{\psi}_2 r_{3/2,z} \dot{\theta}_2 \cos(\phi_2) \\
& + 2 m \sin(\theta_1) \sin(\psi_1) L \cos(\theta_2) \cos(\psi_2) \dot{\psi}_2 r_{3/2,y} \dot{\theta}_2 \sin(\phi_2) \\
& - 2 m \sin(\theta_1) \sin(\psi_1) L \sin(\phi_2) \dot{\phi}_2 \cos(\psi_2) r_{3/2,z} \sin(\theta_2) \dot{\psi}_2 \\
& - m \sin(\theta_1) \sin(\psi_1) L \cos(\phi_2) \sin(\psi_2) \dot{\psi}_2^2 r_{3/2,z} \sin(\theta_2) \\
& - m \sin(\theta_1) \sin(\psi_1) L \cos(\phi_2) \dot{\phi}_2^2 \sin(\theta_2) \sin(\psi_2) r_{3/2,z} \\
& - 2 m \sin(\theta_1) \sin(\psi_1) L \sin(\phi_2) \cos(\theta_2) \dot{\theta}_2 \sin(\psi_2) r_{3/2,z} \dot{\phi}_2 \\
& + F_{4x} \cos(\theta_2) \cos(\psi_2) \sin(\theta_1) \cos(\psi_1) L \\
& - m \sin(\phi_2) \sin(\psi_2) r_{3/2,y} \dot{\phi}_2 \sin(\theta_1) \cos(\psi_1) \dot{L} \\
& + m \sin(\phi_2) \sin(\psi_2) r_{3/2,y} \sin(\theta_2) \dot{\psi}_2 \sin(\theta_1) \cos(\psi_1) \dot{L} \\
& - m \cos(\phi_2) \sin(\theta_2) \cos(\psi_2) r_{3/2,y} \dot{\phi}_2 \sin(\theta_1) \cos(\psi_1) \dot{L} \\
& + F_{4z} \sin(\theta_1) \cos(\psi_1) L \sin(\phi_2) \sin(\psi_2) \\
& + F_{4z} \sin(\theta_1) \cos(\psi_1) L \cos(\phi_2) \sin(\theta_2) \cos(\psi_2) \\
& - F_{4z} \sin(\theta_1) \sin(\psi_1) L \sin(\phi_2) \cos(\psi_2) \\
& + F_{4z} \sin(\theta_1) \sin(\psi_1) L \cos(\phi_2) \sin(\theta_2) \sin(\psi_2) \\
& - F_{4z} \cos(\phi_2) \cos(\theta_2) \cos(\theta_1) L
\end{aligned}
$$

$$
\begin{aligned}
&- m \sin(\theta_1) \cos(\psi_1) L \sin(\theta_2) \dot{\theta}_2^2 \cos(\psi_2) r_{3/2,z} \cos(\phi_2) \\
&- m \sin(\theta_1) \cos(\psi_1) L \sin(\theta_2) \dot{\theta}_2^2 \cos(\psi_2) r_{3/2,y} \sin(\phi_2) \\
&+ F_{4y} \sin(\theta_1) \sin(\psi_1) L \sin(\phi_2) \sin(\theta_2) \sin(\psi_2) \\
&- F_{4y} \sin(\phi_2) \cos(\theta_2) \cos(\theta_1) L + mYId \sin(\theta_1) \sin(\psi_1) \dot{L} \\
&- m \sin(\theta_1) \cos(\psi_1) L \sin(\phi_2) \dot{\phi}_2^2 \sin(\psi_2) r_{3/2,z} \\
&+ F_{4x} \sin(\theta_2) \cos(\theta_1) L - \\
&m \cos(\theta_2) \cos(\psi_2) r_{3/2,y} \dot{\theta}_2 \sin(\phi_2) \sin(\theta_1) \cos(\psi_1) \dot{L} \\
&- m \cos(\phi_2) \sin(\psi_2) r_{3/2,z} \dot{\phi}_2 \sin(\theta_1) \cos(\psi_1) \dot{L} \\
&+ m \cos(\phi_2) \sin(\psi_2) r_{3/2,z} \sin(\theta_2) \dot{\psi}_2 \sin(\theta_1) \cos(\psi_1) \dot{L} \\
&+ m \sin(\phi_2) \sin(\theta_2) \cos(\psi_2) r_{3/2,z} \dot{\phi}_2 \sin(\theta_1) \cos(\psi_1) \dot{L} \\
&+ m \sin(\phi_2) \cos(\psi_2) r_{3/2,y} \dot{\phi}_2 \sin(\theta_1) \sin(\psi_1) \dot{L} \\
&- m \sin(\phi_2) \cos(\psi_2) r_{3/2,y} \sin(\theta_2) \dot{\psi}_2 \sin(\theta_1) \sin(\psi_1) \dot{L} \\
&- m \cos(\phi_2) \sin(\theta_2) \sin(\psi_2) r_{3/2,y} \dot{\phi}_2 \sin(\theta_1) \sin(\psi_1) \dot{L} \\
&- m \sin(\theta_2) r_{3/2,z} \dot{\theta}_2 \cos(\phi_2) \cos(\theta_1) \dot{L} - \\
&m \sin(\theta_2) r_{3/2,y} \dot{\theta}_2 \sin(\phi_2) \cos(\theta_1) \dot{L} \\
&- m \sin(\phi_2) \cos(\theta_2) r_{3/2,z} \dot{\phi}_2 \cos(\theta_1) \dot{L} \\
&+ m \cos(\phi_2) \cos(\theta_2) r_{3/2,y} \dot{\phi}_2 \cos(\theta_1) \dot{L} \\
&- 2 m \cos(\theta_1) L \sin(\phi_2) \sin(\theta_2) \dot{\theta}_2 r_{3/2,z} \dot{\phi}_2 \\
&+ 2 m \cos(\theta_1) L \sin(\theta_2) r_{3/2,y} \dot{\theta}_2 \cos(\phi_2) \dot{\phi}_2 \\
&- 2 m \sin(\theta_1) \cos(\psi_1) L \cos(\theta_2) \sin(\psi_2) \dot{\psi}_2 r_{3/2,z} \dot{\theta}_2 \cos(\phi_2) \\
&- 2 m \sin(\theta_1) \cos(\psi_1) L \cos(\phi_2) \dot{\phi}_2 \sin(\psi_2) r_{3/2,y} \sin(\theta_2) \dot{\psi}_2 \\
&+ 2 m \sin(\theta_1) \cos(\psi_1) L \sin(\phi_2) \cos(\psi_2) \dot{\psi}_2 r_{3/2,y} \dot{\phi}_2
\end{aligned}
$$

$$
\begin{aligned}
&- m \sin(\theta_1) \cos(\psi_1)\, L \sin(\phi_2) \cos(\psi_2)\, \dot{\psi}_2^2 r_{3/2,y} \sin(\theta_2) \\
&- m \sin(\theta_1) \cos(\psi_1)\, L \sin(\phi_2)\, \dot{\phi}_2^2 \sin(\theta_2) \cos(\psi_2)\, r_{3/2,y} \\
&- m \cos(\theta_2) \sin(\psi_2)\, r_{3/2,y} \dot{\theta}_2 \sin(\phi_2) \sin(\theta_1) \sin(\psi_1)\, \dot{L} \\
&+ m \cos(\phi_2) \cos(\psi_2)\, r_{3/2,z} \dot{\phi}_2 \sin(\theta_1) \sin(\psi_1)\, \dot{L} \\
&- m \cos(\phi_2) \cos(\psi_2)\, r_{3/2,z} \sin(\theta_2)\, \dot{\psi}_2 \sin(\theta_1) \sin(\psi_1)\, \dot{L} \\
&+ m \sin(\phi_2) \sin(\theta_2) \sin(\psi_2)\, r_{3/2,z} \dot{\phi}_2 \sin(\theta_1) \sin(\psi_1)\, \dot{L} \\
&+ F_{4y} \sin(\theta_1) \cos(\psi_1)\, L \sin(\phi_2) \sin(\theta_2) \cos(\psi_2) \\
&+ F_{4y} \sin(\theta_1) \sin(\psi_1)\, L \cos(\phi_2) \cos(\psi_2) \\
&+ m \dot{x}_1 \sin(\theta_1) \cos(\psi_1)\, \dot{L} \\
&- m \cos(\theta_2) \sin(\psi_2)\, r_{3/2,z} \dot{\theta}_2 \cos(\phi_2) \sin(\theta_1) \sin(\psi_1)\, \dot{L} \\
&- F_{4y} \sin(\theta_1) \cos(\psi_1)\, L \cos(\phi_2) \sin(\psi_2) \\
&+ F_{4x} \cos(\theta_2) \sin(\psi_2) \sin(\theta_1) \sin(\psi_1)\, L \\
&+ 2\, m \sin(\theta_1) \cos(\psi_1)\, L \cos(\theta_2) \cos(\psi_2)\, r_{3/2,y} \dot{\theta}_2 \cos(\phi_2)\, \dot{\phi}_2 \\
&- 2\, m \sin(\theta_1) \cos(\psi_1)\, L \cos(\theta_2) \sin(\psi_2)\, \dot{\psi}_2\, r_{3/2,y} \dot{\theta}_2 \sin(\phi_2) \\
&+ 2\, m \sin(\theta_1) \cos(\psi_1)\, L \sin(\phi_2)\, \dot{\phi}_2 \sin(\psi_2)\, r_{3/2,z} \sin(\theta_2)\, \dot{\psi}_2 \\
&+ 2\, m \sin(\theta_1) \cos(\psi_1)\, L \cos(\phi_2) \cos(\psi_2)\, \dot{\psi}_2\, r_{3/2,z} \dot{\phi}_2 \\
&- m \sin(\theta_1) \cos(\psi_1)\, L \cos(\phi_2) \cos(\psi_2)\, \dot{\psi}_2^2 r_{3/2,z} \sin(\theta_2) \\
&- m \sin(\theta_1) \cos(\psi_1)\, L \cos(\phi_2)\, \dot{\phi}_2^2 \sin(\theta_2) \cos(\psi_2)\, r_{3/2,z} \\
&- 2\, m \sin(\theta_1) \cos(\psi_1)\, L \sin(\phi_2) \cos(\theta_2)\, \dot{\theta}_2 \cos(\psi_2)\, r_{3/2,z} \dot{\phi}_2 \\
&- m \sin(\theta_1) \sin(\psi_1)\, L \sin(\theta_2)\, \dot{\theta}_2^2 \sin(\psi_2)\, r_{3/2,z} \cos(\phi_2) \\
&- m \sin(\theta_1) \sin(\psi_1)\, L \sin(\theta_2)\, \dot{\theta}_2^2 \sin(\psi_2)\, r_{3/2,y} \sin(\phi_2) \\
&+ 2\, m \sin(\theta_1) \sin(\psi_1)\, L \cos(\theta_2) \sin(\psi_2)\, r_{3/2,y} \dot{\theta}_2 \cos(\phi_2)\, \dot{\phi}_2
\end{aligned}
$$

$$
\begin{aligned}
&+ m \sin(\theta_1) \sin(\psi_1) L \sin(\phi_2) \dot{\phi}_2^2 \cos(\psi_2) r_{3/2,z} \\
&+ 2 m \sin(\theta_1) \sin(\psi_1) L \cos(\phi_2) \sin(\psi_2) \dot{\psi}_2 r_{3/2,z} \dot{\phi}_2 \\
&+ m \sin(\theta_1) \cos(\psi_1) L \cos(\phi_2) \dot{\phi}_2^2 \sin(\psi_2) r_{3/2,y} \\
&+ m \cos(\theta_1) L \cos(\theta_2) \dot{\theta}_2^2 r_{3/2,z} \cos(\phi_2) \\
&+ m \cos(\theta_1) L \cos(\theta_2) \dot{\theta}_2^2 r_{3/2,y} \sin(\phi_2) \\
&+ m \cos(\theta_1) L \cos(\phi_2) \dot{\phi}_2^2 \cos(\theta_2) r_{3/2,z} \\
&+ m \cos(\theta_1) L \sin(\phi_2) \dot{\phi}_2^2 \cos(\theta_2) r_{3/2,y} \\
&- m \sin(\theta_1) L^2 \dot{\psi}_1^2 \cos(\theta_1) \\
&- m \sin(\phi_2) \cos(\psi_2) r_{3/2,z} \dot{\psi}_2 \sin(\theta_1) \cos(\psi_1) \dot{L} \\
&+ m \cos(\phi_2) \cos(\psi_2) r_{3/2,y} \dot{\psi}_2 \sin(\theta_1) \cos(\psi_1) \dot{L} \\
&+ m \cos(\phi_2) \sin(\psi_2) r_{3/2,y} \dot{\psi}_2 \sin(\theta_1) \sin(\psi_1) \dot{L} \\
&+ m \sin(\theta_1) \cos(\psi_1) L \cos(\phi_2) \sin(\psi_2) \dot{\psi}_2^2 r_{3/2,y} \\
&+ m \sin(\theta_1) \sin(\psi_1) L \sin(\phi_2) \cos(\psi_2) \dot{\psi}_2^2 r_{3/2,z} \\
&+ m \sin(\theta_2) \cos(\psi_2) r_{3/2,x} \dot{\theta}_2 \sin(\theta_1) \cos(\psi_1) \dot{L} \\
&+ m \sin(\psi_2) r_{3/2,x} \dot{\psi}_2 \cos(\theta_2) \sin(\theta_1) \cos(\psi_1) \dot{L} \\
&- m \cos(\theta_2) r_{3/2,x} \dot{\theta}_2 \cos(\theta_1) \dot{L} \\
&- m \cos(\psi_2) r_{3/2,x} \dot{\psi}_2 \cos(\theta_2) \sin(\theta_1) \sin(\psi_1) \dot{L} \\
&- m \sin(\theta_1) \sin(\psi_1) L \sin(\psi_2) \dot{\psi}_2^2 r_{3/2,x} \cos(\theta_2) \\
&- m \sin(\theta_1) \sin(\psi_1) L \cos(\phi_2) \cos(\psi_2) \dot{\psi}_2^2 r_{3/2,y} \\
&- m \sin(\phi_2) \sin(\psi_2) r_{3/2,z} \dot{\psi}_2 \sin(\theta_1) \sin(\psi_1) \dot{L} \\
&- m \sin(\theta_1) \cos(\psi_1) L \cos(\theta_2) \dot{\theta}_2^2 \cos(\psi_2) r_{3/2,x} \\
&- m \cos(\theta_1) L \sin(\theta_2) \dot{\theta}_2^2 r_{3/2,x}
\end{aligned}
$$

$$+ 2\,m \sin(\theta_1) \cos(\psi_1)\, L \sin(\theta_2) \sin(\psi_2)\, \dot{\psi}_2\, r_{3/2,x} \dot{\theta}_2$$

$$- m \sin(\theta_1) \cos(\psi_1)\, L \cos(\psi_2)\, \dot{\psi}_2^2 r_{3/2,x} \cos(\theta_2)$$

$$- m \sin(\theta_1) \cos(\psi_1)\, L \sin(\phi_2) \sin(\psi_2)\, \dot{\psi}_2^2 r_{3/2,z}$$

$$- m \sin(\theta_1) \sin(\psi_1)\, L \cos(\theta_2)\, \dot{\theta}_2^2 \sin(\psi_2)\, r_{3/2,x}$$

$$- 2\,m \sin(\theta_1) \sin(\psi_1)\, L \sin(\theta_2) \cos(\psi_2)\, \dot{\psi}_2\, r_{3/2,x} \dot{\theta}_2$$

$$
\begin{aligned}
B_2 = &-\cos(\theta_1)\Big(-2\,m\cos(\psi_1)\,L\sin(\theta_2)\cos(\psi_2)\,\dot{\psi}_2\,r_{3/2,x}\dot{\theta}_2 \\
&-m\cos(\psi_1)\,L\sin(\phi_2)\,\dot{\phi}_2^2\sin(\theta_2)\sin(\psi_2)\,r_{3/2,y} \\
&-m\sin(\psi_1)\,L\cos(\phi_2)\,\dot{\phi}_2^2\sin(\psi_2)\,r_{3/2,y} \\
&+2\,m\sin(\psi_1)\,L\cos(\theta_2)\sin(\psi_2)\,\dot{\psi}_2\,r_{3/2,y}\dot{\theta}_2\,\sin(\phi_2) \\
&-F_{4y}\,\sin(\psi_1)\,L\sin(\phi_2)\sin(\theta_2)\cos(\psi_2) \\
&+F_{4y}\,\cos(\psi_1)\,L\cos(\phi_2)\cos(\psi_2) \\
&+2\,m\cos(\psi_1)\,L\cos(\phi_2)\,\dot{\phi}_2\,\cos(\psi_2)\,r_{3/2,y}\sin(\theta_2)\,\dot{\psi}_2 \\
&+2\,m\sin(\psi_1)\,L\cos(\theta_2)\sin(\psi_2)\,\dot{\psi}_2\,r_{3/2,z}\dot{\theta}_2\,\cos(\phi_2) \\
&+2\,m\sin(\psi_1)\,L\cos(\phi_2)\,\dot{\phi}_2\,\sin(\psi_2)\,r_{3/2,y}\sin(\theta_2)\,\dot{\psi}_2 \\
&-2\,m\sin(\psi_1)\,L\sin(\phi_2)\cos(\psi_2)\,\dot{\psi}_2\,r_{3/2,y}\dot{\phi}_2 \\
&+2\,m\cos(\psi_1)\,L\cos(\theta_2)\cos(\psi_2)\,\dot{\psi}_2\,r_{3/2,y}\dot{\theta}_2\,\sin(\phi_2) \\
&-2\,m\cos(\psi_1)\,L\sin(\phi_2)\,\dot{\phi}_2\,\cos(\psi_2)\,r_{3/2,z}\sin(\theta_2)\,\dot{\psi}_2 \\
&+2\,m\cos(\psi_1)\,L\cos(\phi_2)\sin(\psi_2)\,\dot{\psi}_2\,r_{3/2,z}\dot{\phi}_2 \\
&-2\,m\sin(\psi_1)\,L\sin(\phi_2)\,\dot{\phi}_2\,\sin(\psi_2)\,r_{3/2,z}\sin(\theta_2)\,\dot{\psi}_2 \\
&+m\sin(\psi_1)\,L\sin(\phi_2)\cos(\psi_2)\,\dot{\psi}_2^2 r_{3/2,y}\sin(\theta_2) \\
&+m\sin(\psi_1)\,L\sin(\phi_2)\,\dot{\phi}_2^2\sin(\theta_2)\cos(\psi_2)\,r_{3/2,y} \\
&+2\,m\cos(\psi_1)\,L\cos(\theta_2)\cos(\psi_2)\,\dot{\psi}_2\,r_{3/2,z}\dot{\theta}_2\,\cos(\phi_2) \\
&-2\,m\sin(\psi_1)\,L\cos(\phi_2)\cos(\psi_2)\,\dot{\psi}_2\,r_{3/2,z}\dot{\phi}_2 \\
&+m\sin(\psi_1)\,L\cos(\phi_2)\cos(\psi_2)\,\dot{\psi}_2^2 r_{3/2,z}\sin(\theta_2) \\
&+m\sin(\psi_1)\,L\cos(\phi_2)\,\dot{\phi}_2^2\sin(\theta_2)\cos(\psi_2)\,r_{3/2,z} \\
&+2\,m\sin(\psi_1)\,L\sin(\phi_2)\cos(\theta_2)\,\dot{\theta}_2\,\cos(\psi_2)\,r_{3/2,z}\dot{\phi}_2
\end{aligned}
$$

$$-m\cos(\psi_1)\,L\sin(\theta_2)\,\dot{\theta}_2^2\sin(\psi_2)\,r_{3/2,z}\cos(\phi_2)$$

$$-m\cos(\psi_1)\,L\sin(\theta_2)\,\dot{\theta}_2^2\sin(\psi_2)\,r_{3/2,y}\sin(\phi_2)$$

$$+2\,m\cos(\psi_1)\,L\cos(\theta_2)\sin(\psi_2)\,r_{3/2,y}\dot{\theta}_2\,\cos(\phi_2)\,\dot{\phi}_2$$

$$-m\cos(\psi_1)\,L\cos(\phi_2)\,\dot{\phi}_2^2\cos(\psi_2)\,r_{3/2,y}$$

$$-m\cos(\psi_1)\,L\cos(\phi_2)\sin(\psi_2)\,\dot{\psi}_2^2 r_{3/2,z}\sin(\theta_2)$$

$$-m\cos(\psi_1)\,L\cos(\phi_2)\,\dot{\phi}_2^2\sin(\theta_2)\sin(\psi_2)\,r_{3/2,z}$$

$$+m\cos(\phi_2)\sin(\psi_2)\,r_{3/2,z}\dot{\phi}_2\,\sin(\psi_1)\,\dot{L}$$

$$-m\cos(\phi_2)\sin(\psi_2)\,r_{3/2,z}\sin(\theta_2)\,\dot{\psi}_2\,\sin(\psi_1)\,\dot{L}$$

$$-2\,m\sin(\psi_1)\,L\cos(\theta_2)\cos(\psi_2)\,r_{3/2,y}\dot{\theta}_2\,\cos(\phi_2)\,\dot{\phi}_2$$

$$-2\,m\cos(\psi_1)\,L\sin(\phi_2)\cos(\theta_2)\,\dot{\theta}_2\,\sin(\psi_2)\,r_{3/2,z}\dot{\phi}_2$$

$$+m\cos(\psi_1)\,L\sin(\phi_2)\,\dot{\phi}_2^2\cos(\psi_2)\,r_{3/2,z}$$

$$-m\sin(\phi_2)\cos(\psi_2)\,r_{3/2,y}\sin(\theta_2)\,\dot{\psi}_2\,\cos(\psi_1)\,\dot{L}$$

$$-m\cos(\phi_2)\sin(\theta_2)\sin(\psi_2)\,r_{3/2,y}\dot{\phi}_2\,\cos(\psi_1)\,\dot{L}$$

$$-m\sin(\phi_2)\sin(\theta_2)\cos(\psi_2)\,r_{3/2,z}\dot{\phi}_2\,\sin(\psi_1)\,\dot{L}$$

$$-m\sin(\phi_2)\sin(\psi_2)\,r_{3/2,y}\sin(\theta_2)\,\dot{\psi}_2\,\sin(\psi_1)\,\dot{L}$$

$$-F_{4z}\,\sin(\psi_1)\,L\sin(\phi_2)\sin(\psi_2)$$

$$-m\cos(\phi_2)\cos(\psi_2)\,r_{3/2,z}\sin(\theta_2)\,\dot{\psi}_2\,\cos(\psi_1)\,\dot{L}$$

$$+m\sin(\phi_2)\sin(\theta_2)\sin(\psi_2)\,r_{3/2,z}\dot{\phi}_2\,\cos(\psi_1)\,\dot{L}$$

$$+m\sin(\phi_2)\cos(\psi_2)\,r_{3/2,y}\dot{\phi}_2\,\cos(\psi_1)\,\dot{L}$$

$$-m\cos(\theta_2)\sin(\psi_2)\,r_{3/2,z}\dot{\theta}_2\,\cos(\phi_2)\cos(\psi_1)\,\dot{L}$$

$$-m\cos(\theta_2)\sin(\psi_2)\,r_{3/2,y}\dot{\theta}_2\,\sin(\phi_2)\cos(\psi_1)\,\dot{L}$$

$$+m\cos(\phi_2)\cos(\psi_2)\,r_{3/2,z}\dot{\phi}_2\,\cos(\psi_1)\,\dot{L}$$

$$+m\sin(\psi_1)\,L\sin(\phi_2)\,\dot{\phi}_2^2\sin(\psi_2)\,r_{3/2,z}$$

$$+m \sin(\psi_1) L \sin(\theta_2) \dot{\theta}_2^2 \cos(\psi_2) r_{3/2,z} \cos(\phi_2)$$

$$+m \sin(\psi_1) L \sin(\theta_2) \dot{\theta}_2^2 \cos(\psi_2) r_{3/2,y} \sin(\phi_2)$$

$$-F_{4z} \sin(\psi_1) L \cos(\phi_2) \sin(\theta_2) \cos(\psi_2)$$

$$-F_{4z} \cos(\psi_1) L \sin(\phi_2) \cos(\psi_2)$$

$$+F_{4z} \cos(\psi_1) L \cos(\phi_2) \sin(\theta_2) \sin(\psi_2)$$

$$+m \cos(\theta_2) \cos(\psi_2) r_{3/2,y} \dot{\theta}_2 \sin(\phi_2) \sin(\psi_1) \dot{L}$$

$$+m \cos(\phi_2) \sin(\theta_2) \cos(\psi_2) r_{3/2,y} \dot{\phi}_2 \sin(\psi_1) \dot{L}$$

$$-F_{4x} \cos(\theta_2) \cos(\psi_2) \sin(\psi_1) L$$

$$+m \cos(\theta_2) \cos(\psi_2) r_{3/2,z} \dot{\theta}_2 \cos(\phi_2) \sin(\psi_1) \dot{L}$$

$$+F_{4x} \cos(\theta_2) \sin(\psi_2) \cos(\psi_1) L$$

$$+F_{4y} \sin(\psi_1) L \cos(\phi_2) \sin(\psi_2)$$

$$+F_{4y} \cos(\psi_1) L \sin(\phi_2) \sin(\theta_2) \sin(\psi_2)$$

$$+m \sin(\phi_2) \sin(\psi_2) r_{3/2,y} \dot{\phi}_2 \sin(\psi_1) \dot{L}$$

$$+2\, m \cos(\psi_1) L \sin(\phi_2) \sin(\psi_2) \dot{\psi}_2 r_{3/2,y} \dot{\phi}_2$$

$$-m \cos(\psi_1) L \sin(\phi_2) \sin(\psi_2) \dot{\psi}_2^2 r_{3/2,y} \sin(\theta_2)$$

$$+mYId \cos(\psi_1) \dot{L} - m\dot{x}_1 \sin(\psi_1) \dot{L}$$

$$+m \cos(\psi_1) L \sin(\phi_2) \cos(\psi_2) \dot{\psi}_2^2 r_{3/2,z}$$

$$-m \cos(\phi_2) \cos(\psi_2) r_{3/2,y} \dot{\psi}_2 \sin(\psi_1) \dot{L}$$

$$+m \sin(\psi_1) L \cos(\psi_2) \dot{\psi}_2^2 r_{3/2,x} \cos(\theta_2)$$

$$+m \cos(\phi_2) \sin(\psi_2) r_{3/2,y} \dot{\psi}_2 \cos(\psi_1) \dot{L}$$

$$+m \sin(\psi_1) L \sin(\phi_2) \sin(\psi_2) \dot{\psi}_2^2 r_{3/2,z}$$

$$-m \cos(\psi_1) L \cos(\theta_2) \dot{\theta}_2^2 \sin(\psi_2) r_{3/2,x}$$

$$
\begin{aligned}
&-m\cos(\psi_1)\,L\cos(\phi_2)\cos(\psi_2)\,\dot{\psi}_2^2 r_{3/2,y}\\
&-2\,m\sin(\psi_1)\,L\sin(\theta_2)\sin(\psi_2)\,\dot{\psi}_2\,r_{3/2,x}\dot{\theta}_2\\
&-m\sin(\theta_2)\cos(\psi_2)\,r_{3/2,x}\dot{\theta}_2\,\sin(\psi_1)\,\dot{L}\\
&-m\cos(\psi_1)\,L\sin(\psi_2)\,\dot{\psi}_2^2 r_{3/2,x}\cos(\theta_2)\\
&-m\sin(\psi_2)\,r_{3/2,x}\dot{\psi}_2\,\cos(\theta_2)\sin(\psi_1)\,\dot{L}\\
&-m\cos(\psi_2)\,r_{3/2,x}\dot{\psi}_2\,\cos(\theta_2)\cos(\psi_1)\,\dot{L}\\
&-m\sin(\phi_2)\sin(\psi_2)\,r_{3/2,z}\dot{\psi}_2\,\cos(\psi_1)\,\dot{L}\\
&-m\sin(\psi_1)\,L\cos(\phi_2)\sin(\psi_2)\,\dot{\psi}_2^2 r_{3/2,y}\\
&+m\sin(\theta_2)\sin(\psi_2)\,r_{3/2,x}\dot{\theta}_2\,\cos(\psi_1)\,\dot{L}\\
&+m\sin(\phi_2)\cos(\psi_2)\,r_{3/2,z}\dot{\psi}_2\,\sin(\psi_1)\,\dot{L}\\
&+m\sin(\psi_1)\,L\cos(\theta_2)\,\dot{\theta}_2^2\cos(\psi_2)\,r_{3/2,x}-2\,mL^2\sin(\theta_1)\,\dot{\theta}_1\,\dot{\psi}_1\Big)
\end{aligned}
$$

$$
\begin{aligned}
B_3 = {} & 2\, I_{yy}\dot{\theta}_2\ (\cos(\phi_2))^2 \cos(\theta_2)\, \dot{\psi}_2 \\
& - m \sin(\theta_1)\, \dot{\theta}_1\ \sin(\psi_1)\, \dot{L}\, r_{3/2,y} \sin(\phi_2) \cos(\psi_2) \\
& + I_{yy}\dot{\psi}_2^2\, (\cos(\theta_2))^2 \sin(\phi_2) \cos(\phi_2) \\
& + M_{4x} + \cos(\theta_2)\, \dot{\theta}_2\, \dot{\psi}_2\, I_{xx} \\
& + 4\, m \sin(\phi_2)\, r_{3/2,z}\dot{\psi}_2\, r_{3/2,y} \cos(\phi_2) \cos(\theta_2)\, \dot{\theta}_2 \\
& + 2\, m\dot{\theta}_2^2 r_{3/2,y} r_{3/2,z}\, (\cos(\phi_2))^2 \\
& - m \cos(\phi_2)\, {r_{3/2,y}}^2 \dot{\psi}_2^2 \sin(\phi_2)\, (\cos(\theta_2))^2 \\
& + 2\, m \cos(\theta_2)\, {r_{3/2,y}}^2 \dot{\theta}_2\, \dot{\psi}_2 + F_{4y}\, r_{3/2,z} - F_{4z}\, r_{3/2,y} \\
& - I_{yy}\dot{\psi}_2\ \cos(\theta_2)\, \dot{\theta}_2 \\
& + m\dot{\theta}_2^2 {r_{3/2,y}}^2 \sin(\phi_2) \cos(\phi_2) \\
& + 2\, m \cos(\theta_2)\, \dot{\psi}_2\, {r_{3/2,z}}^2 \dot{\theta}_2\ (\cos(\phi_2))^2 \\
& - m\dot{\theta}_2^2 {r_{3/2,z}}^2 \cos(\phi_2) \sin(\phi_2) \\
& + m\dot{\psi}_2^2 \cos(\theta_2)\, r_{3/2,x} r_{3/2,y} \cos(\phi_2) \sin(\theta_2) \\
& - m\dot{\theta}_2^2 r_{3/2,y} r_{3/2,z} - 2\, m \sin(\phi_2) \sin(\theta_2)\, r_{3/2,x}\dot{\theta}_2\, r_{3/2,y}\dot{\psi}_2 \\
& - m \sin(\phi_2)\, \dot{\psi}_2^2 \cos(\theta_2)\, r_{3/2,x} r_{3/2,z} \sin(\theta_2) \\
& - 2\, m \cos(\theta_2)\, {r_{3/2,y}}^2 \dot{\theta}_2\, \dot{\psi}_2\ (\cos(\phi_2))^2 \\
& + m \sin(\phi_2)\, \dot{\psi}_2^2 {r_{3/2,z}}^2 \cos(\phi_2)\, (\cos(\theta_2))^2 \\
& + m\dot{\psi}_2^2 r_{3/2,z} r_{3/2,y}\, (\cos(\theta_2))^2 \\
& - 2\, m\dot{\psi}_2^2 r_{3/2,z} r_{3/2,y}\, (\cos(\phi_2))^2\, (\cos(\theta_2))^2 \\
& - 2\, m \sin(\theta_2)\, r_{3/2,x}\dot{\theta}_2\ \cos(\phi_2)\, r_{3/2,z}\dot{\psi}_2 + I_{zz}\dot{\psi}_2\ \cos(\theta_2)\, \dot{\theta}_2 \\
& - F_{4y}\, r_{4/2,z} + F_{4z}\, r_{4/2,y} - I_{yy}\dot{\theta}_2^2 \cos(\phi_2) \sin(\phi_2) \\
& + I_{zz}\dot{\theta}_2^2 \cos(\phi_2) \sin(\phi_2)
\end{aligned}
$$

$$
\begin{aligned}
&- m \cos(\theta_1)\, \dot{\theta}_1^2 \sin(\psi_1)\, Lr_{3/2,y} \sin(\phi_2) \cos(\psi_2) \\
&- m \sin(\theta_1)\, \dot{\theta}_1 \sin(\psi_1)\, \dot{L}\, r_{3/2,z} \cos(\phi_2) \cos(\psi_2) \\
&+ m \sin(\theta_1)\, \dot{\theta}_1 \cos(\psi_1)\, \dot{L}\, r_{3/2,z} \cos(\phi_2) \sin(\psi_2) \\
&+ m \cos(\theta_1) \cos(\psi_1)\, \dot{\psi}_1\, \dot{L}\, r_{3/2,z} \sin(\phi_2) \sin(\theta_2) \sin(\psi_2) \\
&- m \sin(\psi_1)\, \dot{\psi}_1^2 \cos(\theta_1)\, Lr_{3/2,z} \cos(\phi_2) \cos(\psi_2) \\
&+ m \sin(\psi_1)\, \dot{\psi}_1^2 \cos(\theta_1)\, Lr_{3/2,y} \cos(\phi_2) \sin(\theta_2) \sin(\psi_2) \\
&- m \cos(\theta_1)\, \dot{\theta}_1^2 \cos(\psi_1)\, Lr_{3/2,z} \sin(\phi_2) \sin(\theta_2) \cos(\psi_2) \\
&- m \cos(\theta_1)\, \dot{\theta}_1^2 \sin(\psi_1)\, Lr_{3/2,z} \sin(\phi_2) \sin(\theta_2) \sin(\psi_2) \\
&+ m \cos(\theta_1)\, \dot{\theta}_1^2 \sin(\psi_1)\, Lr_{3/2,y} \cos(\phi_2) \sin(\theta_2) \sin(\psi_2) \\
&- 2\, m \cos(\psi_1) \sin(\theta_1)\, \dot{\theta}_1\, \dot{\psi}_1\, Lr_{3/2,y} \sin(\phi_2) \cos(\psi_2) \\
&- m \sin(\theta_1)\, \dot{\theta}_1 \cos(\psi_1)\, \dot{L}\, r_{3/2,z} \sin(\phi_2) \sin(\theta_2) \cos(\psi_2) \\
&+ m \sin(\theta_1)\, \dot{\theta}_1 \cos(\psi_1)\, \dot{L}\, r_{3/2,y} \sin(\phi_2) \sin(\psi_2) \\
&+ m \sin(\theta_1)\, \dot{\theta}_1 \cos(\psi_1)\, \dot{L}\, r_{3/2,y} \cos(\phi_2) \sin(\theta_2) \cos(\psi_2) \\
&+ m \cos(\theta_1) \sin(\psi_1)\, \dot{\psi}_1\, \dot{L}\, r_{3/2,z} \cos(\phi_2) \sin(\psi_2) \\
&- m \cos(\theta_1) \sin(\psi_1)\, \dot{\psi}_1\, \dot{L}\, r_{3/2,z} \sin(\phi_2) \sin(\theta_2) \cos(\psi_2) \\
&+ m \cos(\theta_1) \sin(\psi_1)\, \dot{\psi}_1\, \dot{L}\, r_{3/2,y} \sin(\phi_2) \sin(\psi_2) \\
&+ m \cos(\theta_1) \sin(\psi_1)\, \dot{\psi}_1\, \dot{L}\, r_{3/2,y} \cos(\phi_2) \sin(\theta_2) \cos(\psi_2) \\
&+ m \cos(\psi_1)\, \dot{\psi}_1^2 \cos(\theta_1)\, Lr_{3/2,z} \cos(\phi_2) \sin(\psi_2) \\
&- m \cos(\psi_1)\, \dot{\psi}_1^2 \cos(\theta_1)\, Lr_{3/2,z} \sin(\phi_2) \sin(\theta_2) \cos(\psi_2) \\
&+ m \cos(\psi_1)\, \dot{\psi}_1^2 \cos(\theta_1)\, Lr_{3/2,y} \sin(\phi_2) \sin(\psi_2) \\
&+ m \cos(\psi_1)\, \dot{\psi}_1^2 \cos(\theta_1)\, Lr_{3/2,y} \cos(\phi_2) \sin(\theta_2) \cos(\psi_2) \\
&+ m \cos(\theta_1)\, \dot{\theta}_1^2 \cos(\psi_1)\, Lr_{3/2,z} \cos(\phi_2) \sin(\psi_2) \\
&+ m \cos(\theta_1)\, \dot{\theta}_1^2 \cos(\psi_1)\, Lr_{3/2,y} \sin(\phi_2) \sin(\psi_2)
\end{aligned}
$$

$$
\begin{aligned}
&+ m \cos(\theta_1)\, \dot{\theta}_1^2 \cos(\psi_1)\, Lr_{3/2,y} \cos(\phi_2) \sin(\theta_2) \cos(\psi_2) \\
&- 2\, m \sin(\psi_1) \sin(\theta_1)\, \dot{\theta}_1\, \dot{\psi}_1\, Lr_{3/2,z} \cos(\phi_2) \sin(\psi_2) \\
&+ 2\, m \sin(\psi_1) \sin(\theta_1)\, \dot{\theta}_1\, \dot{\psi}_1\, Lr_{3/2,z} \sin(\phi_2) \sin(\theta_2) \cos(\psi_2) \\
&- 2\, m \sin(\psi_1) \sin(\theta_1)\, \dot{\theta}_1\, \dot{\psi}_1\, Lr_{3/2,y} \sin(\phi_2) \sin(\psi_2) \\
&- 2\, m \sin(\psi_1) \sin(\theta_1)\, \dot{\theta}_1\, \dot{\psi}_1\, Lr_{3/2,y} \cos(\phi_2) \sin(\theta_2) \cos(\psi_2) \\
&- 2\, m \cos(\psi_1) \sin(\theta_1)\, \dot{\theta}_1\, \dot{\psi}_1\, Lr_{3/2,z} \cos(\phi_2) \cos(\psi_2) \\
&- 2\, m \cos(\psi_1) \sin(\theta_1)\, \dot{\theta}_1\, \dot{\psi}_1\, Lr_{3/2,z} \sin(\phi_2) \sin(\theta_2) \sin(\psi_2) \\
&+ 2\, m \cos(\psi_1) \sin(\theta_1)\, \dot{\theta}_1\, \dot{\psi}_1\, Lr_{3/2,y} \cos(\phi_2) \sin(\theta_2) \sin(\psi_2) \\
&- m \sin(\theta_1)\, \dot{\theta}_1 \sin(\psi_1)\, \dot{L}\, r_{3/2,z} \sin(\phi_2) \sin(\theta_2) \sin(\psi_2) \\
&+ m \sin(\theta_1)\, \dot{\theta}_1 \sin(\psi_1)\, \dot{L}\, r_{3/2,y} \cos(\phi_2) \sin(\theta_2) \sin(\psi_2) \\
&- m \sin(\psi_1)\, \dot{\psi}_1^2 \cos(\theta_1)\, Lr_{3/2,z} \sin(\phi_2) \sin(\theta_2) \sin(\psi_2) \\
&- m \sin(\psi_1)\, \dot{\psi}_1^2 \cos(\theta_1)\, Lr_{3/2,y} \sin(\phi_2) \cos(\psi_2) \\
&- m \cos(\theta_1)\, \dot{\theta}_1^2 \sin(\psi_1)\, Lr_{3/2,z} \cos(\phi_2) \cos(\psi_2) \\
&+ m \cos(\theta_1) \cos(\psi_1)\, \dot{\psi}_1\, \dot{L}\, r_{3/2,z} \cos(\phi_2) \cos(\psi_2) \\
&+ m \cos(\theta_1) \cos(\psi_1)\, \dot{\psi}_1\, \dot{L}\, r_{3/2,y} \sin(\phi_2) \cos(\psi_2) \\
&- m \cos(\theta_1) \cos(\psi_1)\, \dot{\psi}_1\, \dot{L}\, r_{3/2,y} \cos(\phi_2) \sin(\theta_2) \sin(\psi_2) \\
&- m \sin(\theta_1)\, \dot{\theta}_1^2 L \sin(\phi_2) \cos(\theta_2)\, r_{3/2,z} \\
&+ m \sin(\theta_1)\, \dot{\theta}_1^2 L \cos(\phi_2) \cos(\theta_2)\, r_{3/2,y} \\
&+ m \cos(\theta_1)\, \dot{\theta}_1\, \dot{L} \sin(\phi_2) \cos(\theta_2)\, r_{3/2,z} \\
&- m \cos(\theta_1)\, \dot{\theta}_1\, \dot{L} \cos(\phi_2) \cos(\theta_2)\, r_{3/2,y} \\
&+ mg \sin(\phi_2) \cos(\theta_2)\, r_{3/2,z} - mg \cos(\phi_2) \cos(\theta_2)\, r_{3/2,y} \\
&- I_{zz} \dot{\psi}_2^2 \left(\cos(\theta_2)\right)^2 \sin(\phi_2) \cos(\phi_2) \\
&- 2\, I_{zz} \dot{\theta}_2 \left(\cos(\phi_2)\right)^2 \cos(\theta_2)\, \dot{\psi}_2
\end{aligned}
$$

$$
\begin{aligned}
B_4 = & -m\dot{\psi}_2^2 \sin(\theta_2)\, {r_{3/2,y}}^2 \cos(\theta_2)\, (\cos(\phi_2))^2 \\
& - m\cos(\phi_2)\, \dot{\psi}_2^2 r_{3/2,z} r_{3/2,x} - m\cos(\phi_2)\, \dot{\phi}_2^2 r_{3/2,z} r_{3/2,x} \\
& - m\sin(\phi_2)\, \dot{\psi}_2^2 r_{3/2,y} r_{3/2,x} - 4\, m r_{3/2,z} \dot{\theta}_2\ (\cos(\phi_2))^2\, \dot{\phi}_2\, r_{3/2,y} \\
& - 2\, m {r_{3/2,y}}^2 \dot{\phi}_2\ \cos(\theta_2)\, \dot{\psi}_2 \\
& + m\cos(\theta_1)\sin(\psi_1)\, \dot{\psi}_1\, \dot{L}\ \cos(\theta_2)\cos(\psi_2)\sin(\phi_2)\, r_{3/2,y} \\
& + m\cos(\psi_1)\, \dot{\psi}_1^2 \cos(\theta_1)\, L\cos(\theta_2)\cos(\psi_2)\cos(\phi_2)\, r_{3/2,z} \\
& + m\cos(\psi_1)\, \dot{\psi}_1^2 \cos(\theta_1)\, L\cos(\theta_2)\cos(\psi_2)\sin(\phi_2)\, r_{3/2,y} \\
& + m\cos(\theta_1)\, \dot{\theta}_1^2 \cos(\psi_1)\, L\cos(\theta_2)\cos(\psi_2)\cos(\phi_2)\, r_{3/2,z} \\
& - 2\, m\sin(\psi_1)\sin(\theta_1)\, \dot{\theta}_1\, \dot{\psi}_1\, L\cos(\theta_2)\cos(\psi_2)\cos(\phi_2)\, r_{3/2,z} \\
& - 2\, m\sin(\psi_1)\sin(\theta_1)\, \dot{\theta}_1\, \dot{\psi}_1\, L\cos(\theta_2)\cos(\psi_2)\sin(\phi_2)\, r_{3/2,y} \\
& + mg\sin(\phi_2)\sin(\theta_2)\, r_{3/2,y} + mg\cos(\phi_2)\sin(\theta_2)\, r_{3/2,z} \\
& + m\sin(\theta_1)\, \dot{\theta}_1\ \cos(\psi_1)\, \dot{L}\ \cos(\theta_2)\cos(\psi_2)\cos(\phi_2)\, r_{3/2,z} \\
& + m\sin(\theta_1)\, \dot{\theta}_1\ \cos(\psi_1)\, \dot{L}\ \cos(\theta_2)\cos(\psi_2)\sin(\phi_2)\, r_{3/2,y} \\
& + m\cos(\theta_1)\sin(\psi_1)\, \dot{\psi}_1\, \dot{L}\ \cos(\theta_2)\cos(\psi_2)\cos(\phi_2)\, r_{3/2,z} \\
& - m\sin(\theta_1)\, \dot{\theta}_1^2 L\cos(\phi_2)\sin(\theta_2)\, r_{3/2,z} \\
& - m\sin(\theta_1)\, \dot{\theta}_1^2 L\sin(\phi_2)\sin(\theta_2)\, r_{3/2,y} \\
& + m\cos(\theta_1)\, \dot{\theta}_1\, \dot{L}\ \cos(\phi_2)\sin(\theta_2)\, r_{3/2,z} \\
& + m\cos(\theta_1)\, \dot{\theta}_1\, \dot{L}\ \sin(\phi_2)\sin(\theta_2)\, r_{3/2,y} \\
& + M_{4y}\ \cos(\phi_2) - M_{4z}\ \sin(\phi_2) - F_{4y}\ \sin(\phi_2)\, r_{4/2,x} \\
& - F_{4z}\ \cos(\phi_2)\, r_{4/2,x} + F_{4x}\ \cos(\phi_2)\, r_{4/2,z} \\
& + F_{4x}\ \sin(\phi_2)\, r_{4/2,y} + mg\cos(\theta_2)\, r_{3/2,x} \\
& - I_{xx}\cos(\theta_2)\, \dot{\psi}_2\, \dot{\phi}_2 + I_{xx}\cos(\theta_2)\, \dot{\psi}_2^2 \sin(\theta_2)
\end{aligned}
$$

$$
\begin{aligned}
&+ m \sin(\theta_1)\, \dot{\theta}_1\ \sin(\psi_1)\, \dot{L}\ \cos(\theta_2) \sin(\psi_2) \cos(\phi_2)\, r_{3/2,z} \\
&+ m \sin(\theta_1)\, \dot{\theta}_1\ \sin(\psi_1)\, \dot{L}\ \cos(\theta_2) \sin(\psi_2) \sin(\phi_2)\, r_{3/2,y} \\
&+ m \sin(\psi_1)\, \dot{\psi}_1^2 \cos(\theta_1)\, L \cos(\theta_2) \sin(\psi_2) \cos(\phi_2)\, r_{3/2,z} \\
&+ m \sin(\psi_1)\, \dot{\psi}_1^2 \cos(\theta_1)\, L \cos(\theta_2) \sin(\psi_2) \sin(\phi_2)\, r_{3/2,y} \\
&+ m \cos(\theta_1)\, \dot{\theta}_1^2 \sin(\psi_1)\, L \cos(\theta_2) \sin(\psi_2) \cos(\phi_2)\, r_{3/2,z} \\
&+ m \cos(\theta_1)\, \dot{\theta}_1^2 \sin(\psi_1)\, L \cos(\theta_2) \sin(\psi_2) \sin(\phi_2)\, r_{3/2,y} \\
&- m \cos(\theta_1) \cos(\psi_1)\, \dot{\psi}_1\, \dot{L}\ \cos(\theta_2) \sin(\psi_2) \cos(\phi_2)\, r_{3/2,z} \\
&- m \cos(\theta_1) \cos(\psi_1)\, \dot{\psi}_1\, \dot{L}\ \cos(\theta_2) \sin(\psi_2) \sin(\phi_2)\, r_{3/2,y} \\
&+ 2\, m \cos(\psi_1) \sin(\theta_1)\, \dot{\theta}_1\, \dot{\psi}_1\, L \cos(\theta_2) \sin(\psi_2) \cos(\phi_2)\, r_{3/2,z} \\
&+ 2\, m \cos(\psi_1) \sin(\theta_1)\, \dot{\theta}_1\, \dot{\psi}_1\, L \cos(\theta_2) \sin(\psi_2) \sin(\phi_2)\, r_{3/2,y} \\
&+ m \cos(\theta_1)\, \dot{\theta}_1^2 \cos(\psi_1)\, L \cos(\theta_2) \cos(\psi_2) \sin(\phi_2)\, r_{3/2,y} \\
&- I_{zz} \left(\cos(\phi_2)\right)^2 \sin(\theta_2)\, \dot{\psi}_2^2 \cos(\theta_2) \\
&- F_{4x}\ \sin(\phi_2)\, r_{3/2,y} - F_{4x}\ \cos(\phi_2)\, r_{3/2,z} + F_{4y}\ \sin(\phi_2)\, r_{3/2,x} \\
&+ F_{4z}\ \cos(\phi_2)\, r_{3/2,x} - 2\, I_{yy} \left(\cos(\phi_2)\right)^2 \dot{\psi}_2\ \cos(\theta_2)\, \dot{\phi}_2 \\
&+ 2\, I_{yy} \cos(\phi_2)\, \dot{\theta}_2\ \sin(\phi_2)\, \dot{\phi}_2 + 2\, I_{zz} \left(\cos(\phi_2)\right)^2 \dot{\phi}_2\ \cos(\theta_2)\, \dot{\psi}_2 \\
&- 2\, I_{zz} \cos(\phi_2)\, \dot{\phi}_2\, \dot{\theta}_2\ \sin(\phi_2) - I_{zz} \dot{\phi}_2\ \cos(\theta_2)\, \dot{\psi}_2 \\
&+ I_{yy} \dot{\phi}_2\, \dot{\psi}_2\ \cos(\theta_2) - I_{yy} \dot{\psi}_2^2 \sin(\theta_2) \cos(\theta_2) \\
&+ 2\, m r_{3/2,y} \dot{\theta}_2\, \dot{\phi}_2\, r_{3/2,z} + 2\, m \sin(\phi_2)\, \dot{\psi}_2^2 r_{3/2,y} r_{3/2,x} \left(\cos(\theta_2)\right)^2 \\
&+ 2\, m \cos(\phi_2)\, \dot{\psi}_2^2 r_{3/2,z} r_{3/2,x} \left(\cos(\theta_2)\right)^2 \\
&+ m \cos(\theta_1) \cos(\psi_1)\, \dot{\psi}_1\, \dot{L}\, r_{3/2,x} \sin(\theta_2) \sin(\psi_2) \\
&+ 2\, m \sin(\phi_2)\, r_{3/2,y} \dot{\phi}_2\, r_{3/2,x} \sin(\theta_2)\, \dot{\psi}_2 \\
&+ m \dot{\psi}_2^2 \sin(\theta_2)\, {r_{3/2,y}}^2 \cos(\theta_2) + 2\, m \cos(\phi_2)\, r_{3/2,z} \dot{\phi}_2\, r_{3/2,x} \sin(\theta_2)\, \dot{\psi}_2 \\
&+ m \left(\cos(\phi_2)\right)^2 \dot{\psi}_2^2 \sin(\theta_2)\, {r_{3/2,z}}^2 \cos(\theta_2)
\end{aligned}
$$

$$
\begin{aligned}
&+ m \cos(\theta_1)\, \dot{\theta}_1\, \dot{L}\, \cos(\theta_2)\, r_{3/2,x} \\
&- 2\, m\, (\cos(\phi_2))^2\, {r_{3/2,z}}^2 \dot{\phi}_2\, \cos(\theta_2)\, \dot{\psi}_2 \\
&- 2\, m {r_{3/2,y}}^2 \dot{\theta}_2\, \sin(\phi_2) \cos(\phi_2)\, \dot{\phi}_2 \\
&- 4\, m \sin(\phi_2)\, r_{3/2,z} \dot{\psi}_2\, \cos(\theta_2) \cos(\phi_2)\, \dot{\phi}_2\, r_{3/2,y} \\
&- m \sin(\psi_1)\, \dot{\psi}_1^2 \cos(\theta_1)\, L r_{3/2,x} \sin(\theta_2) \sin(\psi_2) \\
&- m \cos(\theta_1)\, \dot{\theta}_1^2 \sin(\psi_1)\, L r_{3/2,x} \sin(\theta_2) \sin(\psi_2) \\
&- 2\, m \cos(\psi_1) \sin(\theta_1)\, \dot{\theta}_1\, \dot{\psi}_1\, L r_{3/2,x} \sin(\theta_2) \sin(\psi_2) \\
&- m \sin(\phi_2)\, \dot{\phi}_2^2 r_{3/2,y} r_{3/2,x} + 2\, m {r_{3/2,z}}^2 \dot{\theta}_2\, \cos(\phi_2) \sin(\phi_2)\, \dot{\phi}_2 \\
&- m \sin(\theta_1)\, \dot{\theta}_1\, \cos(\psi_1)\, \dot{L}\, r_{3/2,x} \sin(\theta_2) \cos(\psi_2) \\
&+ 2\, m {r_{3/2,y}}^2 \dot{\phi}_2\, \cos(\theta_2)\, \dot{\psi}_2\, (\cos(\phi_2))^2 \\
&- m \dot{\psi}_2^2 \cos(\theta_2)\, {r_{3/2,x}}^2 \sin(\theta_2) \\
&+ 2\, m \cos(\phi_2)\, \dot{\psi}_2^2 \sin(\theta_2)\, r_{3/2,z} \cos(\theta_2) \sin(\phi_2)\, r_{3/2,y} \\
&- m \cos(\theta_1) \sin(\psi_1)\, \dot{\psi}_1\, \dot{L}\, r_{3/2,x} \sin(\theta_2) \cos(\psi_2) \\
&- m \cos(\psi_1)\, \dot{\psi}_1^2 \cos(\theta_1)\, L r_{3/2,x} \sin(\theta_2) \cos(\psi_2) \\
&- m \cos(\theta_1)\, \dot{\theta}_1^2 \cos(\psi_1)\, L r_{3/2,x} \sin(\theta_2) \cos(\psi_2) \\
&+ 2\, m \sin(\psi_1) \sin(\theta_1)\, \dot{\theta}_1\, \dot{\psi}_1\, L r_{3/2,x} \sin(\theta_2) \cos(\psi_2) \\
&- m \sin(\theta_1)\, \dot{\theta}_1^2 L \cos(\theta_2)\, r_{3/2,x} \\
&- m \sin(\theta_1)\, \dot{\theta}_1\, \sin(\psi_1)\, \dot{L}\, r_{3/2,x} \sin(\theta_2) \sin(\psi_2) \\
&+ I_{yy} \dot{\psi}_2^2 \sin(\theta_2) \cos(\theta_2)\, (\cos(\phi_2))^2
\end{aligned}
$$

$$
\begin{aligned}
B_5 = {} & F_{4y} \sin(\theta_2)\, r_{4/2,z} + m \cos(\theta_1)\, \dot{\theta}_1^2 \sin(\psi_1)\, L \sin(\phi_2) \sin(\psi_2)\, r_{3/2,z} \\
& + 2\, I_{zz} \sin(\phi_2)\, \dot{\phi}_2\, (\cos(\theta_2))^2 \cos(\phi_2)\, \dot{\psi}_2 \\
& - m \sin(\theta_1)\, \dot{\theta}_1\, \cos(\psi_1)\, \dot{L}\, \cos(\phi_2) \cos(\psi_2)\, r_{3/2,y} \\
& + 2\, m \cos(\theta_2)\, {r_{3/2,y}}^2 \dot{\theta}_2\, \dot{\phi}_2\, (\cos(\phi_2))^2 \\
& + m \sin(\theta_1)\, \dot{\theta}_1\, \sin(\psi_1)\, \dot{L}\, \cos(\psi_2) \cos(\theta_2)\, r_{3/2,x} \\
& + m \cos(\theta_1)\, \dot{\theta}_1^2 \cos(\psi_1)\, L \sin(\phi_2) \cos(\psi_2)\, r_{3/2,z} \\
& - m \cos(\theta_2)\, \dot{\theta}_2^2 r_{3/2,x} \cos(\phi_2)\, r_{3/2,y} \\
& - I_{zz} \cos(\phi_2) \sin(\theta_2)\, \dot{\theta}_2^2 \sin(\phi_2) \\
& + I_{yy} \sin(\phi_2) \sin(\theta_2)\, \dot{\theta}_2^2 \cos(\phi_2) \\
& + m \cos(\theta_1)\, \dot{\theta}_1^2 \sin(\psi_1)\, L \sin(\phi_2) \cos(\psi_2) \sin(\theta_2)\, r_{3/2,y} \\
& - 2\, m \sin(\theta_2)\, \dot{\theta}_2^2 r_{3/2,z} (\cos(\phi_2))^2\, r_{3/2,y} + 2\, m \dot{\psi}_2\, r_{3/2,x} \dot{\theta}_2\, \cos(\phi_2)\, r_{3/2,z} \\
& + F_{4z}\, \sin(\theta_2)\, r_{3/2,y} - I_{zz} \dot{\phi}_2\, \cos(\theta_2)\, \dot{\theta}_2 - F_{4y}\, \cos(\phi_2) \cos(\theta_2)\, r_{3/2,x} \\
& + F_{4z}\, \sin(\phi_2) \cos(\theta_2)\, r_{3/2,x} + F_{4x}\, \cos(\theta_2) \cos(\phi_2)\, r_{3/2,y} \\
& + \cos(\theta_2)\, I_{yy} \dot{\theta}_2\, \dot{\phi}_2 - F_{4x}\, \cos(\theta_2) \sin(\phi_2)\, r_{3/2,z} \\
& - 2\, \cos(\theta_2)\, \dot{\theta}_2\, \dot{\psi}_2\, I_{xx} \sin(\theta_2) \\
& - 2\, m \cos(\theta_2)\, \dot{\psi}_2\, {r_{3/2,z}}^2 \dot{\theta}_2\, (\cos(\phi_2))^2 \sin(\theta_2) \\
& - 2\, m \sin(\phi_2)\, {r_{3/2,z}}^2 \dot{\psi}_2\, \cos(\phi_2)\, \dot{\phi}_2\, (\cos(\theta_2))^2 \\
& - m \sin(\theta_1)\, \dot{\theta}_1\, \cos(\psi_1)\, \dot{L}\, \sin(\psi_2) \cos(\theta_2)\, r_{3/2,x} \\
& - 2\, m \cos(\psi_1) \sin(\theta_1)\, \dot{\theta}_1\, \dot{\psi}_1\, L \cos(\phi_2) \sin(\psi_2)\, r_{3/2,y} \\
& - m \cos(\theta_1) \sin(\psi_1)\, \dot{\psi}_1\, \dot{L}\, \sin(\psi_2) \cos(\theta_2)\, r_{3/2,x} \\
& - m \cos(\theta_1) \sin(\psi_1)\, \dot{\psi}_1\, \dot{L}\, \cos(\phi_2) \cos(\psi_2)\, r_{3/2,y} \\
& + M_{4y}\, \sin(\phi_2) \cos(\theta_2) + M_{4z}\, \cos(\phi_2) \cos(\theta_2)
\end{aligned}
$$

$$
\begin{aligned}
&- M_{4x} \sin(\theta_2) + 2 \left(\cos(\phi_2)\right)^2 \cos(\theta_2) I_{zz} \dot{\theta}_2 \dot{\phi}_2 \\
&- F_{4z} \sin(\theta_2) r_{4/2,y} - 2 m \dot{\phi}_2 r_{3/2,z} \dot{\psi}_2 r_{3/2,y} \left(\cos(\theta_2)\right)^2 \\
&+ 4 m \dot{\phi}_2 r_{3/2,z} \dot{\psi}_2 r_{3/2,y} \left(\cos(\phi_2)\right)^2 \left(\cos(\theta_2)\right)^2 \\
&+ m \sin(\theta_2) \dot{\theta}_2^2 {r_{3/2,z}}^2 \cos(\phi_2) \sin(\phi_2) \\
&+ m \sin(\psi_1) \dot{\psi}_1^2 \cos(\theta_1) L \sin(\phi_2) \sin(\psi_2) r_{3/2,z} \\
&+ m \sin(\theta_1) \dot{\theta}_1 \sin(\psi_1) \dot{L} \sin(\phi_2) \sin(\psi_2) r_{3/2,z} \\
&+ m \sin(\psi_1) \dot{\psi}_1^2 \cos(\theta_1) L \cos(\psi_2) \cos(\theta_2) r_{3/2,x} \\
&- m \cos(\psi_1) \dot{\psi}_1^2 \cos(\theta_1) L \cos(\phi_2) \cos(\psi_2) r_{3/2,y} \\
&+ 2 m \sin(\phi_2) \dot{\phi}_2 r_{3/2,z} \sin(\theta_2) \dot{\psi}_2 \cos(\theta_2) r_{3/2,x} \\
&+ 2 m \cos(\psi_1) \sin(\theta_1) \dot{\theta}_1 \dot{\psi}_1 L \cos(\psi_2) \cos(\theta_2) r_{3/2,x} \\
&+ 2 m \cos(\psi_1) \sin(\theta_1) \dot{\theta}_1 \dot{\psi}_1 L \sin(\phi_2) \sin(\psi_2) r_{3/2,z} \\
&+ 2 m \sin(\phi_2) \dot{\psi}_2 r_{3/2,x} \dot{\theta}_2 r_{3/2,y} - 4 m \sin(\phi_2) \dot{\psi}_2 r_{3/2,x} \dot{\theta}_2 r_{3/2,y} \left(\cos(\theta_2)\right)^2 \\
&+ 2 m \sin(\theta_2) \dot{\psi}_2 {r_{3/2,x}}^2 \dot{\theta}_2 \cos(\theta_2) \\
&- m \sin(\theta_1) \dot{\theta}_1 \sin(\psi_1) \dot{L} \cos(\phi_2) \sin(\psi_2) r_{3/2,y} \\
&- m \cos(\theta_1) \dot{\theta}_1^2 \cos(\psi_1) L \cos(\phi_2) \cos(\psi_2) r_{3/2,y} \\
&- 2 m \sin(\psi_1) \sin(\theta_1) \dot{\theta}_1 \dot{\psi}_1 L \sin(\phi_2) \cos(\psi_2) r_{3/2,z} \\
&+ m \cos(\psi_1) \dot{\psi}_1^2 \cos(\theta_1) L \sin(\phi_2) \cos(\psi_2) r_{3/2,z} \\
&- 2 m \cos(\theta_2) \dot{\psi}_2 {r_{3/2,y}}^2 \dot{\theta}_2 \sin(\theta_2) \\
&+ 2 m \cos(\theta_2) \dot{\psi}_2 {r_{3/2,y}}^2 \dot{\theta}_2 \sin(\theta_2) \left(\cos(\phi_2)\right)^2 \\
&+ m \sin(\phi_2) \cos(\theta_2) \dot{\theta}_2^2 r_{3/2,x} r_{3/2,z} \\
&+ m \cos(\theta_1) \sin(\psi_1) \dot{\psi}_1 \dot{L} \sin(\phi_2) \cos(\psi_2) r_{3/2,z} \\
&- 2 m \cos(\theta_2) {r_{3/2,z}}^2 \dot{\theta}_2 \left(\cos(\phi_2)\right)^2 \dot{\phi}_2 + 2 m \cos(\theta_2) \dot{\theta}_2 {r_{3/2,z}}^2 \dot{\phi}_2 \\
&+ 2 m \cos(\phi_2) \dot{\phi}_2 {r_{3/2,y}}^2 \dot{\psi}_2 \sin(\phi_2) \left(\cos(\theta_2)\right)^2 -
\end{aligned}
$$

$$
\begin{aligned}
& 4\,m\cos\left(\phi_2\right) r_{3/2,z}\dot{\phi}_2\ \cos\left(\theta_2\right) r_{3/2,y}\dot{\theta}_2\ \sin\left(\phi_2\right) \\
& -m\cos\left(\theta_1\right)\dot{\theta}_1^2\sin\left(\psi_1\right) L\cos\left(\phi_2\right)\sin\left(\psi_2\right) r_{3/2,y} - F_{4y}\ \sin\left(\theta_2\right) r_{3/2,z} \\
& -m\cos\left(\theta_1\right)\cos\left(\psi_1\right)\dot{\psi}_1\,\dot{L}\ \sin\left(\phi_2\right)\sin\left(\psi_2\right) r_{3/2,z} \\
& +2\,m\sin\left(\psi_1\right)\sin\left(\theta_1\right)\dot{\theta}_1\,\dot{\psi}_1\,L\sin\left(\psi_2\right)\cos\left(\theta_2\right) r_{3/2,x} \\
& +2\,m\sin\left(\psi_1\right)\sin\left(\theta_1\right)\dot{\theta}_1\,\dot{\psi}_1\,L\cos\left(\phi_2\right)\cos\left(\psi_2\right) r_{3/2,y} \\
& -2\,m\cos\left(\phi_2\right)\dot{\phi}_2\, r_{3/2,y}\sin\left(\theta_2\right)\dot{\psi}_2\ \cos\left(\theta_2\right) r_{3/2,x} \\
& +m\cos\left(\phi_2\right)\dot{\phi}_2^2 r_{3/2,y}\cos\left(\theta_2\right) r_{3/2,x} + m\sin\left(\theta_2\right)\dot{\theta}_2^2 r_{3/2,y} r_{3/2,z} \\
& +m\sin\left(\theta_1\right)\dot{\theta}_1\ \cos\left(\psi_1\right)\dot{L}\ \sin\left(\phi_2\right)\cos\left(\psi_2\right) r_{3/2,z} \\
& -4\,m\cos\left(\theta_2\right)\dot{\psi}_2\, r_{3/2,z}\dot{\theta}_2\ \cos\left(\phi_2\right)\sin\left(\phi_2\right)\sin\left(\theta_2\right) r_{3/2,y} \\
& -4\,m\left(\cos\left(\theta_2\right)\right)^2\dot{\psi}_2\, r_{3/2,z}\dot{\theta}_2\ \cos\left(\phi_2\right) r_{3/2,x} \\
& -m\cos\left(\theta_1\right)\dot{\theta}_1^2\cos\left(\psi_1\right) L\sin\left(\psi_2\right)\cos\left(\theta_2\right) r_{3/2,x} \\
& +m\cos\left(\theta_1\right)\dot{\theta}_1^2\sin\left(\psi_1\right) L\cos\left(\psi_2\right)\cos\left(\theta_2\right) r_{3/2,x} \\
& -m\cos\left(\theta_1\right)\cos\left(\psi_1\right)\dot{\psi}_1\,\dot{L}\ \cos\left(\psi_2\right)\cos\left(\theta_2\right) r_{3/2,x} \\
& -m\cos\left(\psi_1\right)\dot{\psi}_1^2\cos\left(\theta_1\right) L\sin\left(\psi_2\right)\cos\left(\theta_2\right) r_{3/2,x} \\
& -m\sin\left(\phi_2\right)\dot{\phi}_2^2 r_{3/2,z}\cos\left(\theta_2\right) r_{3/2,x} + 2\,I_{yy}\sin\left(\theta_2\right)\dot{\theta}_2\,\dot{\psi}_2\ \cos\left(\theta_2\right) \\
& -2\,I_{yy}\sin\left(\theta_2\right)\dot{\theta}_2\,\dot{\psi}_2\ \cos\left(\theta_2\right)\left(\cos\left(\phi_2\right)\right)^2 \\
& -m\sin\left(\theta_2\right)\dot{\theta}_2^2 {r_{3/2,y}}^2\sin\left(\phi_2\right)\cos\left(\phi_2\right) \\
& -m\sin\left(\psi_1\right)\dot{\psi}_1^2\cos\left(\theta_1\right) L\cos\left(\phi_2\right)\sin\left(\psi_2\right) r_{3/2,y} \\
& +m\cos\left(\theta_1\right)\cos\left(\psi_1\right)\dot{\psi}_1\,\dot{L}\ \cos\left(\phi_2\right)\sin\left(\psi_2\right) r_{3/2,y} \\
& +F_{4x}\ \sin\left(\phi_2\right)\cos\left(\theta_2\right) r_{4/2,z} - F_{4x}\ \cos\left(\phi_2\right)\cos\left(\theta_2\right) r_{4/2,y} \\
& -F_{4z}\ \sin\left(\phi_2\right)\cos\left(\theta_2\right) r_{4/2,x} + I_{xx}\cos\left(\theta_2\right)\dot{\theta}_2\,\dot{\phi}_2 \\
& +F_{4y}\ \cos\left(\phi_2\right)\cos\left(\theta_2\right) r_{4/2,x} - 2\,I_{yy}\left(\cos\left(\phi_2\right)\right)^2\dot{\phi}_2\ \cos\left(\theta_2\right)\dot{\theta}_2 \\
& -m\cos\left(\psi_1\right)\dot{\psi}_1^2\cos\left(\theta_1\right) L\cos\left(\phi_2\right)\sin\left(\psi_2\right)\sin\left(\theta_2\right) r_{3/2,z}
\end{aligned}
$$

$$
\begin{aligned}
&- m \sin(\theta_1)\, \dot{\theta}_1 \cos(\psi_1)\, \dot{L} \cos(\phi_2) \sin(\psi_2) \sin(\theta_2)\, r_{3/2,z} \\
&- m \sin(\theta_1)\, \dot{\theta}_1 \cos(\psi_1)\, \dot{L} \sin(\phi_2) \sin(\psi_2) \sin(\theta_2)\, r_{3/2,y} \\
&- m \cos(\theta_1) \sin(\psi_1)\, \dot{\psi}_1\, \dot{L} \cos(\phi_2) \sin(\psi_2) \sin(\theta_2)\, r_{3/2,z} \\
&- m \cos(\theta_1) \sin(\psi_1)\, \dot{\psi}_1\, \dot{L} \sin(\phi_2) \sin(\psi_2) \sin(\theta_2)\, r_{3/2,y} \\
&- m \cos(\psi_1)\, \dot{\psi}_1^2 \cos(\theta_1)\, L \sin(\phi_2) \sin(\psi_2) \sin(\theta_2)\, r_{3/2,y} \\
&- m \cos(\theta_1)\, \dot{\theta}_1^2 \cos(\psi_1)\, L \cos(\phi_2) \sin(\psi_2) \sin(\theta_2)\, r_{3/2,z} \\
&- m \cos(\theta_1)\, \dot{\theta}_1^2 \cos(\psi_1)\, L \sin(\phi_2) \sin(\psi_2) \sin(\theta_2)\, r_{3/2,y} \\
&+ 2\, m \sin(\psi_1) \sin(\theta_1)\, \dot{\theta}_1\, \dot{\psi}_1\, L \cos(\phi_2) \sin(\psi_2) \sin(\theta_2)\, r_{3/2,z} \\
&+ 2\, m \sin(\psi_1) \sin(\theta_1)\, \dot{\theta}_1\, \dot{\psi}_1\, L \sin(\phi_2) \sin(\psi_2) \sin(\theta_2)\, r_{3/2,y} \\
&+ 2\, m \cos(\psi_1) \sin(\theta_1)\, \dot{\theta}_1\, \dot{\psi}_1\, L \cos(\phi_2) \cos(\psi_2) \sin(\theta_2)\, r_{3/2,z} \\
&+ 2\, m \cos(\psi_1) \sin(\theta_1)\, \dot{\theta}_1\, \dot{\psi}_1\, L \sin(\phi_2) \cos(\psi_2) \sin(\theta_2)\, r_{3/2,y} \\
&+ m \sin(\theta_1)\, \dot{\theta}_1 \sin(\psi_1)\, \dot{L} \cos(\phi_2) \cos(\psi_2) \sin(\theta_2)\, r_{3/2,z} \\
&+ m \sin(\theta_1)\, \dot{\theta}_1 \sin(\psi_1)\, \dot{L} \sin(\phi_2) \cos(\psi_2) \sin(\theta_2)\, r_{3/2,y} \\
&+ m \sin(\psi_1)\, \dot{\psi}_1^2 \cos(\theta_1)\, L \cos(\phi_2) \cos(\psi_2) \sin(\theta_2)\, r_{3/2,z} \\
&+ m \sin(\psi_1)\, \dot{\psi}_1^2 \cos(\theta_1)\, L \sin(\phi_2) \cos(\psi_2) \sin(\theta_2)\, r_{3/2,y} \\
&+ m \cos(\theta_1)\, \dot{\theta}_1^2 \sin(\psi_1)\, L \cos(\phi_2) \cos(\psi_2) \sin(\theta_2)\, r_{3/2,z} \\
&- m \cos(\theta_1) \cos(\psi_1)\, \dot{\psi}_1\, \dot{L} \cos(\phi_2) \cos(\psi_2) \sin(\theta_2)\, r_{3/2,z} \\
&- m \cos(\theta_1) \cos(\psi_1)\, \dot{\psi}_1\, \dot{L} \sin(\phi_2) \cos(\psi_2) \sin(\theta_2)\, r_{3/2,y} \\
&+ 2 \left(\cos(\phi_2)\right)^2 \cos(\theta_2)\, I_{zz} \sin(\theta_2)\, \dot{\theta}_2\, \dot{\psi}_2 \\
&- 2 \sin(\phi_2) \left(\cos(\theta_2)\right)^2 I_{yy} \dot{\psi}_2 \cos(\phi_2)\, \dot{\phi}_2
\end{aligned}
$$

B. Derivation of Equations of Motion: Maple Script

```
with(LinearAlgebra):
readlib(mtaylor):
with(codegen,C):
with(CodeGeneration):
#with(VectorCalculus):

############################
## Read custom diff package
############################

read ‘eqmo_util.mpl‘;
# read in custom differentiation package
# The following 4 vectors contain all the variable names that
# are functions of time. This is needed to support the custom
# differentiation code in eqmo_util.mpl.
```

```
#####################################################
## Store all the states in vars,varsd,varsdd,varst
#####################################################

vars    := Vector([th1,ps1,ph2,th2,ps2]):
varsd   := Vector([th1d,ps1d,ph2d,th2d,ps2d]):
varsdd  := Vector([th1dd,ps1dd,ph2dd,th2dd,ps2dd]):
varst   := Vector([th1(t),ps1(t),ph2(t),th2(t),ps2(t)]):

#####################################################
## Rotation Matrices to rotate vectors between {I}
## frame, {T} frame and {B} frame
#####################################################

Rth1        := Matrix([[cos(th1),        0,          sin(th1)],
            [0,              1,          0         ],
            [-sin(th1),      0,          cos(th1)]]):

Rps1        := Matrix([[ cos(ps1),       sin(ps1),       0],
            [-sin(ps1),      cos(ps1),       0],
            [0,              0,              1]]):

RI2T        := MatrixMatrixMultiply(Rth1,Rps1):
RT2I        := Transpose(RI2T):
```

```
Rph2      := Matrix([[1,              0,              0       ],
           [0,              cos(ph2),       sin(ph2)],
           [0,              -sin(ph2),      cos(ph2)]]):

Rth2      := Matrix([[cos(th2),       0,      -sin(th2)],
           [0,              1,      0       ],
           [sin(th2),       0,      cos(th2)]]):

Rps2      := Matrix([[cos(ps2),       sin(ps2),       0],
           [-sin(ps2),      cos(ps2),       0],
           [0,              0,              1]]):


RI2B      := MatrixMatrixMultiply(Rph2,MatrixMatrixMultiply(Rth2,Rps2)):

RB2I      := Transpose(RI2B):

################################################
## Getting velocity of point 2
## (CG of the parafoil-payload system)
################################################

p1I       := Vector([X1,  Y1,  0]): # ship position
v1I       := Vector([X1d, Y1d, 0]): # velocity of the ship in {I} frame
```

```
p31T       := Vector([-L, 0, 0]):    # p31 in {T} frame
p31I       := MatrixVectorMultiply(RT2I,p31T):

p32B       := Vector([p32xb, p32yb, p32zb]):# relative vector between CG
                                    # and point of attachment
                                    # defined in {B} frame
p32I       := MatrixVectorMultiply(RB2I,p32B):

omgT       := Vector([ sin(th1)*ps1d,-th1d,cos(th1)*ps1d]):
omgB       := Vector([ph2d-sin(th2)*ps2d,
            th2d*cos(ph2) + ps2d*cos(th2)*sin(ph2),
            cos(ph2)*cos(th2)*ps2d - th2d*sin(ph2)]):

ddtp31T := Vector([-Ld, 0, 0]): # derivative of vector p31 in {T} frame
omgTcrp31T := CrossProduct(omgT,p31T):
omgBcrp32B := CrossProduct(omgB,p32B):

p2I        := p1I + p31I - p32I:

v2I        := v1I + MatrixVectorMultiply(RT2I,ddtp31T) +
              MatrixVectorMultiply(RT2I,omgTcrp31T) -
              MatrixVectorMultiply(RB2I,omgBcrp32B):

v2B        := MatrixVectorMultiply(RI2B,v2I):
```

```
#####################################################
## Kinetic Energy, Potential Energy and Lagrangian
#####################################################

InrtMat := Matrix([[Ixx, 0, 0],
                   [0, Iyy, 0],
                   [0, 0, Izz]]):

Trot := 1/2*Multiply(VectorMatrixMultiply(Transpose(omgB),InrtMat),omgB):
Ttrans:= 1/2*mass*Multiply(Transpose(v2I),v2I):

KE :=  Ttrans + Trot:
PE := -mass*grav*p2I(3):

Lag := KE - PE:



####################
## Dynamic Equations
####################

DynEq        := MakeEQMO(Lag,vars,varsd,varsdd,varst):

######################
## Generalized Forces
```

```
####################

p42B        := Vector([p42xb, p42yb, p42zb]):
# relative vector between CG and aero center 4 defined in {B} frame
omgBcrp42B := CrossProduct(omgB,p42B):
v4B         := v2B + omgBcrp42B:



delv4Bth1d        :=Vector(1..3,0):
delv4Bps1d        :=Vector(1..3,0):
delv4Bph2d        :=Vector(1..3,0):
delv4Bth2d        :=Vector(1..3,0):
delv4Bps2d        :=Vector(1..3,0):

for i from 1 to 3 do
      delv4Bth1d[i]        := diff(v4B[i],th1d):
      delv4Bps1d[i]        := diff(v4B[i],ps1d):
      delv4Bph2d[i]        := diff(v4B[i],ph2d):
      delv4Bth2d[i]        := diff(v4B[i],th2d):
      delv4Bps2d[i]        := diff(v4B[i],ps2d):
end do:

delomgBth1d        :=Vector(1..3,0):
delomgBps1d        :=Vector(1..3,0):
delomgBph2d        :=Vector(1..3,0):
```

```
delomgBth2d        :=Vector(1..3,0):
delomgBps2d        :=Vector(1..3,0):

for i from 1 to 3 do
        delomgBth1d[i]        := diff(omgB[i],th1d):
        delomgBps1d[i]        := diff(omgB[i],ps1d):
        delomgBph2d[i]        := diff(omgB[i],ph2d):
        delomgBth2d[i]        := diff(omgB[i],th2d):
       delomgBps2d[i]        := diff(omgB[i],ps2d):
end do:


Ma4b        := Vector([M4x, M4y, M4z]):
Fa4b        := Vector([F4x, F4y, F4z]):

Qth1        := Multiply(Transpose(delv4Bth1d),Fa4b) +
         Multiply(Transpose(delomgBth1d),Ma4b):
Qps1        := Multiply(Transpose(delv4Bps1d),Fa4b) +
         Multiply(Transpose(delomgBps1d),Ma4b):
Qph2        := Multiply(Transpose(delv4Bph2d),Fa4b) +
         Multiply(Transpose(delomgBph2d),Ma4b):
Qth2       := Multiply(Transpose(delv4Bth2d),Fa4b) +
         Multiply(Transpose(delomgBth2d),Ma4b):
Qps2        := Multiply(Transpose(delv4Bps2d),Fa4b) +
         Multiply(Transpose(delomgBps2d),Ma4b):
```

```
############################################################
## Final Equations in the form of Comat*varsdd = RHSmat
############################################################

GenForce := Vector([Qth1, Qps1, Qph2, Qth2, Qps2]):

for i from 1 to 5 do
 DynEq[i]:=DynEq[i]-GenForce[i]:
end do:

# Coefficient Matrix
Comat:=Matrix(1..5,1..5,0):
for i from 1 to 5 do
   for j from 1 to 5 do
      temp:=collect(DynEq[i],varsdd[j]):
      Comat[i,j]:=coeff(temp,varsdd[j]):
   end do:
end do:

# Right Hand Side Matrix
RHSmat:=Vector(1..5,0):
for i from 1 to 5 do
   RHSmatbuild:=collect(DynEq[i],varsdd[1])-Comat[i,1]*varsdd[1]:
   RHSmatbuild:=collect(RHSmatbuild,varsdd[2])-Comat[i,2]*varsdd[2]:
```

```
   RHSmatbuild:=collect(RHSmatbuild,varsdd[3])-Comat[i,3]*varsdd[3]:
   RHSmatbuild:=collect(RHSmatbuild,varsdd[4])-Comat[i,4]*varsdd[4]:
   RHSmat[i]:=-1*(collect(RHSmatbuild,varsdd[5])-Comat[i,5]*varsdd[5]):
end do:

 Comat        := simplify(Comat,trig):
 RHSmat := simplify(RHSmat,trig):

C(Comat,resultname="A");
C(RHSmat,resultname="B");

#########################
## Steady State Equations
#########################

SSeq        := Vector(1..5,0):

for i from 1 to 5 do
      SSeq[i] := subs([th1d=0,ps1d=0,ph2d=0,th2d=0,ps2d=0,Ld=0],RHSmat(i)):
end do:

Matlab(SSeq,resultname="SSeq");
```

C. Steady State Values

The steady state values of all states corresponding to the stability boundaries shown in Figure 4.6 are presented here. The cells in red color indicate unstable steady state values.

Table C.1

Steady state values of in-plane tow angle θ_{1_0} (deg) for $\eta = 0^\circ$

1.7						58.7					
1.6						58.1					
1.5						57.4					
1.4						56.6					
1.3						55.6					
1.2					48.8	54.5	48.8				
1.1					48.5	53.3	48.5				
1					47.8	51.8	47.8				
0.9					46.8	50.1	46.8				
0.8				38.5	45.5	48.1	45.5	38.5			
0.7				37.9	43.8	46.0	43.8	37.9			
0.6			29.9	36.9	41.8	43.5	41.8	36.9	29.9		
0.5			29.5	35.5	39.7	41.0	39.7	35.5	29.5		
0.4		22.5	28.8	33.9	37.4	38.4	37.4	33.9	28.8	22.5	
0.3		22.3	27.8	32.3	35.3	36.1	35.3	32.3	27.8	22.3	
0.2	16.1	21.8	26.9	30.9	33.6	34.1	33.6	30.9	26.9	21.8	16.1
0.1		21.5	26.2	30.0	32.4	32.8	32.4	30.0	26.2	21.5	
0	16.1	21.4	26.0	29.7	32.0	32.4	32.0	29.7	26.0	21.4	16.1
$\frac{v_w}{v_s} \Uparrow$ $\delta_a \Rightarrow$	-1	-0.8	-0.6	-0.4	-0.2	0	0.2	0.4	0.6	0.8	1

Table C.2
Steady state values of off-plane tow angle ψ_{1_0} (deg) for $\eta = 0°$

1.7						59.5					
1.6						58.0					
1.5						56.3					
1.4						54.5					
1.3						52.4					
1.2					79.9	50.2	20.5				
1.1					74.9	47.7	20.6				
1					69.7	45.0	20.3				
0.9					64.4	42.0	19.6				
0.8				74.5	59.0	38.7	18.4	2.8			
0.7				68.1	53.4	35.0	16.6	1.9			
0.6			71.8	61.4	47.7	31.0	14.2	0.5	-9.9		
0.5			64.8	54.8	41.9	26.6	11.2	-1.6	-11.7		
0.4		65.2	57.7	48.1	36.0	21.8	7.6	-4.5	-14.1	-21.6	
0.3		58.2	50.8	41.4	29.9	16.7	3.5	-8.0	-17.4	-24.8	
0.2	57.1	51.3	44.0	34.9	23.9	11.3	-1.3	-12.3	-21.4	-28.7	-34.5
0.1		44.8	37.6	28.6	17.9	5.7	-6.5	-17.2	-26.2	-33.4	
0	44.6	38.8	31.6	22.7	12.1	0.0	-12.1	-22.7	-31.6	-38.8	-44.6
$\frac{v_w}{v_s} \Uparrow$ $\delta_a \Rightarrow$	-1	-0.8	-0.6	-0.4	-0.2	0	0.2	0.4	0.6	0.8	1

Table C.3
Steady state values of roll angle ϕ_{2_0} (deg) for $\eta = 0°$

1.7						0.0					
1.6						0.0					
1.5						0.0					
1.4						0.0					
1.3						0.0					
1.2					-17.5	0.0	17.5				
1.1					-15.8	0.0	15.8				
1					-14.1	0.0	14.1				
0.9					-12.7	0.0	12.7				
0.8				-22.9	-11.4	0.0	11.4	22.9			
0.7				-20.6	-10.3	0.0	10.3	20.6			
0.6			-28.3	-18.6	-9.3	0.0	9.3	18.6	28.3		
0.5			-25.7	-17.0	-8.5	0.0	8.5	17.0	25.7		
0.4		-31.9	-23.6	-15.6	-7.8	0.0	7.8	15.6	23.6	31.9	
0.3		-29.7	-22.0	-14.6	-7.3	0.0	7.3	14.6	22.0	29.7	
0.2	-35.6	-28.1	-20.9	-13.9	-6.9	0.0	6.9	13.9	20.9	28.1	35.6
0.1		-27.2	-20.2	-13.4	-6.7	0.0	6.7	13.4	20.2	27.2	
0	-34.0	-26.9	-20.0	-13.3	-6.6	0.0	6.6	13.3	20.0	26.9	34.0
$\frac{v_w}{v_s} \Uparrow$ $\delta_a \Rightarrow$	-1	-0.8	-0.6	-0.4	-0.2	0	0.2	0.4	0.6	0.8	1

Table C.4
Steady state values of pitch angle θ_{2_0} (deg) for $\eta = 0°$

1.7						24.3					
1.6						24.4					
1.5						24.6					
1.4						24.8					
1.3						25.0					
1.2					24.8	25.3	24.8				
1.1					25.3	25.6	25.3				
1					25.7	25.9	25.7				
0.9					26.2	26.3	26.2				
0.8				25.9	26.6	26.6	26.6	25.9			
0.7				26.6	27.1	27.0	27.1	26.6			
0.6			26.3	27.2	27.6	27.5	27.6	27.2	26.3		
0.5			27.1	27.8	28.0	27.9	28.0	27.8	27.1		
0.4		26.8	27.8	28.3	28.5	28.8	28.5	28.3	27.8	26.8	
0.3		27.5	28.3	28.7	28.8	28.6	28.8	28.7	28.3	27.5	
0.2	27.0	28.0	28.7	29.1	29.1	28.9	29.1	29.1	28.7	28.0	27.0
0.1		28.4	29.0	29.3	29.3	29.1	29.3	29.3	29.0	28.4	
0	27.5	28.5	29.0	29.3	29.4	29.2	29.4	29.3	29.0	28.5	27.5
$\frac{v_w}{v_s} \Uparrow$ $\delta_a \Rightarrow$	-1	-0.8	-0.6	-0.4	-0.2	0	0.2	0.4	0.6	0.8	1

Table C.5
Steady state values of yaw angle ψ_{2_0} (deg) for $\eta = 0°$

1.7						59.5					
1.6						58.0					
1.5						56.3					
1.4						54.5					
1.3						52.4					
1.2					43.5	50.2	56.8				
1.1					41.7	47.7	53.7				
1					39.6	45.0	50.4				
0.9					37.2	42.0	46.8				
0.8				29.9	34.3	38.7	43.0	47.4			
0.7				27.1	31.1	35.0	38.9	42.9			
0.6			20.0	23.8	27.4	31.0	34.5	38.2	41.9		
0.5			16.6	20.0	23.3	26.6	29.8	33.1	36.5		
0.4		9.3	12.6	15.7	18.8	21.8	24.8	27.9	31.0	34.3	
0.3		5.0	8.1	11.0	13.9	16.7	19.5	22.4	25.3	28.4	
0.2	-2.8	0.2	3.1	5.9	8.6	11.3	14.0	16.7	19.5	22.4	25.4
0.1		-5.1	-2.3	0.5	3.1	5.7	8.3	11.0	13.7	16.5	
0	-13.5	-10.7	-7.9	-5.2	-2.6	0.0	2.6	5.2	7.9	10.7	13.5
$\frac{v_w}{v_s} \Uparrow$ $\delta_a \Rightarrow$	-1	-0.8	-0.6	-0.4	-0.2	0	0.2	0.4	0.6	0.8	1

Table C.6
Steady state values of in-plane tow angle θ_{1_0} (deg) for $\eta = 10°$

1.2						64.6					
1.1					56.6	63.2	56.6				
1					56.0	61.6	56.0				
0.9				44.4	55.0	59.6	55.0	44.4			
0.8				44.5	53.5	57.2	53.5	44.5			
0.7				44.0	51.5	54.5	51.5	44.0			
0.6			34.3	42.7	48.9	51.3	48.9	42.7	34.3		
0.5			33.7	40.8	46.0	47.8	46.0	40.8	33.7		
0.4		25.4	32.5	38.5	42.7	44.1	42.7	38.5	32.5	25.4	
0.3		24.7	30.8	35.9	39.4	40.4	39.4	35.9	30.8	24.7	
0.2		23.6	29.0	33.4	36.4	37.1	36.4	33.4	29.0	23.6	
0.1	16.8	22.4	27.3	31.3	33.8	34.3	33.8	31.3	27.3	22.4	16.8
0	16.1	21.4	26.0	29.7	32.0	32.4	32.0	29.7	26.0	21.4	16.1
$\frac{v_w}{v_s} \Uparrow$ $\delta_a \Rightarrow$	-1	-0.8	-0.6	-0.4	-0.2	0	0.2	0.4	0.6	0.8	1

Table C.7
Steady state values of off-plane tow angle ψ_{1_0} (deg) for $\eta = 10°$

1.2						49.8					
1.1					82.5	47.3	12.1				
1					76.5	44.6	12.7				
0.9				87.8	70.3	41.6	12.8	-4.7			
0.8				80.9	63.9	38.2	12.6	-4.5			
0.7				73.7	57.5	34.6	11.7	-4.5			
0.6			76.6	66.2	50.9	30.6	10.2	-5.1	-15.5		
0.5			68.9	58.6	44.3	26.2	8.1	-6.2	-16.5		
0.4		68.4	61.0	51.0	37.7	21.5	5.3	-8.0	-18.0	-25.4	
0.3		60.6	53.2	43.5	31.2	16.5	1.8	-10.6	-20.3	-27.6	
0.2		52.9	45.6	36.2	24.6	11.1	-2.3	-14.0	-23.3	-30.6	
0.1	51.3	45.6	38.3	29.3	18.2	5.6	-7.0	-18.0	-27.1	-34.3	-40.1
0	44.6	38.8	31.6	22.7	12.1	0.0	-12.1	-22.7	-31.6	-38.8	-44.6
$\frac{v_w}{v_s} \Uparrow$ $\delta_a \Rightarrow$	-1	-0.8	-0.6	-0.4	-0.2	0	0.2	0.4	0.6	0.8	1

Table C.8
Steady state values of roll angle ϕ_{2_0} (deg) for $\eta = 10°$

1.2						0.0					
1.1					-15.2	0.0	15.2				
1					-13.6	0.0	13.6				
0.9				-24.7	-12.2	0.0	12.2	24.7			
0.8				-22.2	-11.0	0.0	11.0	22.2			
0.7				-19.9	-9.9	0.0	9.9	19.9			
0.6			-27.4	-18.1	-9.0	0.0	9.0	18.1	27.4		
0.5			-25.0	-16.5	-8.2	0.0	8.2	16.5	25.0		
0.4		-31.1	-23.0	-15.2	-7.6	0.0	7.6	15.2	23.0	31.1	
0.3		-29.1	-21.6	-14.3	-7.1	0.0	7.1	14.3	21.6	29.1	
0.2		-27.7	-20.6	-13.7	-6.8	0.0	6.8	13.7	20.6	27.7	
0.1	-34.2	-27.0	-20.1	-13.3	-6.7	0.0	6.7	13.3	20.1	27.0	34.2
0	-34.0	-26.9	-20.0	-13.3	-6.6	0.0	6.6	13.3	20.0	26.9	34.0
$\frac{v_w}{v_s} \Uparrow$ $\delta_a \Rightarrow$	-1	-0.8	-0.6	-0.4	-0.2	0	0.2	0.4	0.6	0.8	1

Table C.9
Steady state values of pitch angle θ_{2_0} (deg) for $\eta = 10°$

1.2						17.1					
1.1					17.4	17.7	17.4				
1					18.2	18.3	18.2				
0.9				18.0	19.0	19.0	19.0	18.0			
0.8				19.2	19.9	19.9	19.9	19.2			
0.7				20.4	20.9	20.8	20.9	20.4			
0.6			20.8	21.6	21.9	21.8	21.9	21.6	20.8		
0.5			22.3	22.9	23.1	22.9	23.1	22.9	22.3		
0.4		22.8	23.7	24.2	24.4	24.2	24.4	24.2	23.7	22.8	
0.3		24.4	25.2	25.6	25.6	25.4	25.6	25.6	25.2	24.4	
0.2		25.9	26.6	26.9	26.9	26.7	26.9	26.9	26.6	25.9	
0.1	26.4	27.3	27.9	28.2	28.2	28.0	28.2	28.2	27.9	27.3	26.4
0	27.5	28.5	29.0	29.3	29.4	29.2	29.4	29.3	29.0	28.5	27.5
$\frac{v_w}{v_s} \Uparrow$ $\delta_a \Rightarrow$	-1	-0.8	-0.6	-0.4	-0.2	0	0.2	0.4	0.6	0.8	1

Table C.10
Steady state values of yaw angle ψ_{2_0} (deg) for $\eta = 10°$

1.2						49.8					
1.1					41.7	47.3	52.9				
1.0					39.5	44.6	49.6				
0.9				32.4	37.0	41.6	46.1	50.7			
0.8				30.0	34.2	38.2	42.3	46.5			
0.7				27.1	30.9	34.6	38.3	42.0			
0.6			20.3	23.8	27.2	30.6	33.9	37.4	40.9		
0.5			16.8	20.0	23.2	26.2	29.3	32.4	35.7		
0.4		9.6	12.7	15.7	18.7	21.5	24.3	27.3	30.3	33.4	
0.3		5.2	8.2	11.0	13.8	16.5	19.1	21.9	24.8	27.7	
0.2		0.3	3.2	5.9	8.6	11.1	13.7	16.4	19.1	21.9	
0.1	-7.8	-5.0	-2.2	0.5	3.1	5.6	8.2	10.8	13.5	16.2	19.1
0.0	-13.5	-10.7	-7.9	-5.2	-2.6	0.0	2.6	5.2	7.9	10.7	13.5
$\frac{v_w}{v_s} \Uparrow$ $\delta_a \Rightarrow$	-1.0	-0.8	-0.6	-0.4	-0.2	0.0	0.2	0.4	0.6	0.8	1.0

Table C.11
Steady state values of in-plane tow angle θ_{1_0} (deg) for $\eta = 30°$

0.8						76.4					
0.7					65.7	72.6	65.7				
0.6				52.2	62.7	68.0	62.7	52.2			
0.5				50.2	58.6	62.4	58.6	50.2			
0.4			38.7	46.9	53.5	56.1	53.5	46.9	38.7		
0.3		28.7	36.1	42.7	47.7	49.5	47.7	42.7	36.1	28.7	
0.2		26.6	32.8	38.1	41.9	43.0	41.9	38.1	32.8	26.6	
0.1	18.2	24.0	29.3	33.6	36.5	37.1	36.5	33.6	29.3	24.0	18.2
0.0	16.1	21.4	26.0	29.7	32.0	32.4	32.0	29.7	26.0	21.4	16.1
Vw/Vshp & gamA	-1.0	-0.8	-0.6	-0.4	-0.2	0.0	0.2	0.4	0.6	0.8	1.0

Table C.12
Steady state values of off-plane tow angle ψ_{1_0} (deg) for $\eta = 30°$

0.8						34.7					
0.7					73.7	31.2	-11.2				
0.6				52.2	62.3	27.5	-7.4	-24.7			
0.5				68.8	51.7	23.4	-4.8	-21.9			
0.4			68.0	46.9	42.0	19.1	-3.8	-19.8	-29.8		
0.3		64.8	57.8	47.8	33.3	14.6	-4.2	-18.6	-28.7	-35.6	
0.2		55.4	48.2	38.4	25.5	9.8	-5.9	-18.8	-28.6	-35.8	
0.1	52.3	46.7	39.4	30.1	18.5	4.9	-8.6	-20.2	-29.5	-36.8	-42.4
0.0	44.6	38.8	31.6	22.7	12.1	0.0	-12.1	-22.7	-31.6	-38.8	-44.6
$\frac{v_w}{v_s} \Uparrow$ $\delta_a \Rightarrow$	-1.0	-0.8	-0.6	-0.4	-0.2	0.0	0.2	0.4	0.6	0.8	1.0

Table C.13
Steady state values of roll angle ϕ_{2_0} (deg) for $\eta = 30°$

0.8						0.0					
0.7					-9.7	0.0	9.7				
0.6				-17.6	-8.8	0.0	8.8	17.6			
0.5				-16.1	-8.0	0.0	8.0	16.1			
0.4			-22.4	-14.8	-7.4	0.0	7.4	14.8	22.4		
0.3		-28.3	-21.0	-13.9	-7.0	0.0	7.0	13.9	21.0	28.3	
0.2		-27.1	-20.1	-13.4	-6.7	0.0	6.7	13.4	20.1	27.1	
0.1	-33.7	-26.6	-19.8	-13.2	-6.6	0.0	6.6	13.2	19.8	26.6	33.7
0.0	-34.0	-26.9	-20.0	-13.3	-6.6	0.0	6.6	13.3	20.0	26.9	34.0
$\frac{v_w}{v_s} \Uparrow$ $\delta_a \Rightarrow$	-1.0	-0.8	-0.6	-0.4	-0.2	0.0	0.2	0.4	0.6	0.8	1.0

Table C.14
Steady state values of pitch angle θ_{2_0} (deg) for $\eta = 30°$

0.8						6.6					
0.7					8.7	8.6	8.7				
0.6				10.8	11.0	10.8	11.0	10.8			
0.5				13.5	13.6	13.4	13.6	13.5			
0.4			16.0	16.4	16.5	16.3	16.5	16.4	16.0		
0.3		18.5	19.2	19.5	19.6	19.3	19.6	19.5	19.2	18.5	
0.2		21.9	22.5	22.8	22.8	22.6	22.8	22.8	22.5	21.9	
0.1	24.4	25.3	25.8	26.1	26.1	25.9	26.1	26.1	25.8	25.3	24.4
0.0	27.5	28.5	29.0	29.3	29.4	29.2	29.4	29.3	29.0	28.5	27.5
$\frac{v_w}{v_s} \Uparrow$ $\delta_a \Rightarrow$	-1.0	-0.8	-0.6	-0.4	-0.2	0.0	0.2	0.4	0.6	0.8	1.0

Table C.15
Steady state values of yaw angle ψ_{2_0} (deg) for $\eta = 30°$

0.8						34.7					
0.7					27.7	31.2	34.7				
0.6				21.1	24.3	27.5	30.6	33.8			
0.5				17.6	20.6	23.4	26.3	29.2			
0.4			10.9	13.7	16.5	19.1	21.8	24.5	27.3		
0.3		-28.3	6.7	9.4	12.0	14.6	17.1	19.7	22.4	25.2	
0.2		-0.5	2.2	4.8	7.4	9.8	12.3	14.8	17.4	20.2	
0.1	-8.2	-5.4	-2.7	-0.1	2.5	4.9	7.4	10.0	12.6	15.3	18.1
0.0	-13.5	-10.7	-7.9	-5.2	-2.6	0.0	2.6	5.2	7.9	10.7	13.5
$\frac{v_w}{v_s} \Uparrow$ $\delta_a \Rightarrow$	-1.0	-0.8	-0.6	-0.4	-0.2	0.0	0.2	0.4	0.6	0.8	1.0

D. Copyrights

1. Figure 1.1 is an image in the public domain originally created by United States Marine Corps. As a work of U.S. federal government, this image is in public domain. Refer (1) for more information.

2. Figure 1.2 is an image in the public domain. Refer (2) for more information.

3. Figure 1.3 (and Figure 3.8) is a copyrighted image owned by Flight Concepts International. They have granted the permission to republish this image in my dissertation for reference purpose. The email permission is attached below:

   From: red@flightconcepts.com

   Subject: Re: copyrights permission

   Date: April 11, 2011 6:51:13 AM EDT

   To: Huskymail <aspurani@mtu.edu>

   Reply-To: red@flightconcepts.com <red@parachutesdirect.com>

   Anand It's ok...

   Thanks

   Red

   —— Original Message ——

   From: Huskymail

To: info@flightconcepts.com

Sent: Sunday, April 10, 2011 10:32 PM

Subject: copyrights permission

Hello,

My name is Anand Puranik and I am a graduate student working with Dr Gordon Parker at Michigan Technological University. I am working on a project related to paragliders in association with Mr Dexter Bird of Craft Engineering Associates in Virginia.

In my dissertation I intend to use a photo of a powered paraglider (condor) from your website which Dexter Bird has procured from you. Please allow me to use this image for reference purposes only.

Thanks,

Anand Puranik,

PhD Candidate,

Intelligent Systems and Control Laboratory,

Department of Mechanical Engineering,

Michigan Technological University,

Houghton, MI-49931.

(906) 370-0985

4. Figure 2.1 and Figure 2.2 are the images owned by NASA and are available in public domain. Refer (33) for more information.

5. Figure 2.3 and Figure 2.4 are republished from (5) with the permission from AIAA who own the copyright of this publication. The email permission is attached below:

   From: Mike Baden-Campbell <MikeB@aiaa.org>

   Subject: RE: copyright permission

   Date: April 11, 2011 4:09:51 PM EDT

   To: Anand Puranik <aspurani@mtu.edu>

   Anand,

   AIAA holds the copyright on this work. We grant you permission to reprint Figures 1 and 2 from the work mentioned below in your dissertation. We ask that the source be cited properly and that the figures be accompanied with the following statement, ”Reprinted with permission of the American Institute of Aeronautics and Astronautics.”

   Let me know if you have any additional questions and good luck with your defense.
   Sincerely,
   Michael Baden-Campbell
   AIAA Publications

   ——Original Message——

   From: Anand Puranik [mailto:aspurani@mtu.edu]

   Sent: Monday, April 11, 2011 3:40 PM

   To: Mike Baden-Campbell

   Subject: Re: copyright permission

6. Figure 2.7 has been redrawn from (6) with the permission from AIAA who own the copyright of this publication. The email permission is attached below:

   From: Mike Baden-Campbell <MikeB@aiaa.org>

   Subject: RE: copyright permission

   Date: April 28, 2011 11:12:03 AM EDT

   To: Huskymail <aspurani@mtu.edu>

   Anand,

   AIAA also grants you permission to redraw the figure that appears on page 2 of AIAA Paper 1975-1394 in your dissertation. We ask that the source be cited properly and that the figures be accompanied with the following statement, ”Reprinted with permission of the American Institute of Aeronautics and Astronautics.”

   Sincerely,

   Michael Baden-Campbell

   AIAA Publications

   ——Original Message——

   From: Huskymail [mailto:aspurani@mtu.edu]

   Sent: Wednesday, April 27, 2011 10:09 PM

   To: Mike Baden-Campbell

   Subject: Re: copyright permission